ANALYSIS OF DIFFUSION PROCESSES IN THE HUMAN BODY BY MEANS OF MAGNETIC RESONANCE IMAGING, SPECTROSCOPY AND TRACTOGRAPHY

CHRISTIAN WIESEOTTE

THESIS PRESENTED TO THE MAX PLANCK GRADUATE CENTER FOR THE ACADEMIC DEGREE OF DOCTOR RERUM NATURALIUM (DR. RER. NAT.)

Johannes Gutenberg University Medical Center
Department of Radiology, Section of Medical Physics

Max Planck Graduate Center
mit der Johannes Gutenberg-Universität Mainz

Examination date: April 1st 2016

"While examining the form of these particles immersed in water, I observed many of them very evidently in motion; [...] These motions were such as to satisfy me, after frequently repeated observation, that they arose neither from currents in the fluid, nor from its gradual evaporation, but belonged to the particle itself. [...] Specimens of several plants, some of which had been dried and preserved in an herbarium for upwards of twenty years, and others not less than a century, still exhibited the molecules [...] in evident motion. [...] Reflecting on all the facts with which I had now become acquainted, I was disposed to believe that the minute spherical particles or Molecules [...] were in reality the supposed constituent or elementary Molecules of organic bodies [...]."

- Robert Brown, 1827 [13]

ABSTRACT

The experiments presented in this thesis were designed to study diffusion processes in the human body under two distinct environmental conditions, i.e. free and restricted diffusion.

In the typical timescales of milliseconds in magnetic resonance imaging (MRI), the diffusion of contrast agent molecules in blood vessels can be regarded as isotropic. However, reliably measured values of the diffusion coefficients have not been reported so far. With this thesis, a new approach to assess the diffusivity of Gd-DOTA as the most commonly used MRI contrast agent is presented. In order to enable direct observation of the complex by means of ^{1}H NMR spectroscopy, the paramagnetic Gd^{3+} ion of Gd-DOTA was replaced by Ga^{3+}. The diffusion coefficient of Ga-DOTA in D_2O at body temperature was measured with high precision using 2D DOSY NMR experiments: $D = (4.38 \pm 0.04) \times 10^{-10}\,\mathrm{m^2/s}$.

The hydrodynamic similarity of Ga-DOTA and Gd-DOTA was verified using dielectric relaxation spectroscopy. Consequently, the diffusion coefficient of Ga-DOTA as a hydrodynamic analogue of Gd-DOTA is also valid for the MRI contrast agent. Direct diffusion measurements in human blood were not feasible due to the strong ^{1}H signal background. However, an estimate of the diffusivity in human blood plasma at body temperature was derived using the Stokes-Einstein relation to correct for the higher solvent viscosity: $D_{\mathrm{plasma}} = (2.92 \pm 0.25) \times 10^{-10}\,\mathrm{m^2/s}$.

Within the framework of the "Panini Project", anisotropic diffusion along neuron fiber tracts in fixed post mortem human brain specimens was investigated. Using a highly optimized setup, unprecedented spatial resolutions of up to 350 µm on a full-bore human 3 T MRI system were achieved. Reconstruction of fiber pathways based on the local diffusion orientation distributions showed an impressive level of detail. However, tissue fixation imposed a strong limitation on the achievable angular resolution in the reconstruction of complex neuron microstructures.

Using fixed and fresh pig hearts, the proposed method was transferred to cardiac imaging and the impact of tissue fixation on signal intensity and diffusion contrast was studied. The existence of a structurally stable state in unfixed tissue was demonstrated and allowed for continuous image acquisition over 13 h. The helical structure of myocardial fiber bands was accurately reconstructed as were the vessel walls of the aorta, pulmonary trunk and right coronary artery. Analysis of spherical harmonic energy spectra and fractional anisotropy confirmed an increased angular resolution in data sets of unfixed tissue compared to fixed tissue.

In a pilot study, the feasibility of high-resolution tractography of unfixed human tissue specimens was investigated. In the human brain, major white matter pathways were successfully reconstructed at 0.9 mm isotropic resolution. Fiber reconstructions in the human heart were less accurate as a consequence of shorter relaxation times. However, both ventricles and parts of several vessel walls were identified in the reconstruction.

ZUSAMMENFASSUNG

In der vorliegenden Dissertation wurden Diffusionsprozesse im menschlichen Körper unter den Rahmenbedingungen der freien und eingeschränkten Diffusion untersucht.

In den für die Magnetresonanztomographie (MRT) üblichen Zeitskalen von wenigen Millisekunden kann die Diffusion von Kontrastmittelmolekülen in Blutgefäßen als isotrop angesehen werden. Verlässlich gemessene Diffusionskoeffizienten wurden bisher jedoch nicht publiziert. Im Zuge dieser Arbeit wurde ein neues Verfahren zur Bestimmung des Diffusionskoeffizienten von Gd-DOTA als dem am häufigsten verwenden Kontrastmittel entwickelt. Um eine direkte Beobachtung mittels ^{1}H NMR Spektroskopie zu ermöglichen, wurde das paramagnetische Gd^{3+} Ion des Komplexes durch Ga^{3+} ersetzt. Der Diffusionskoeffizient von Ga-DOTA in D_2O bei Körpertemperatur wurde mittels 2D DOSY NMR bestimmt zu $D = (4.38 \pm 0.04) \times 10^{-10}\,\mathrm{m^2/s}$. Die hydrodynamische Ähnlichkeit von Ga-DOTA und Gd-DOTA wurde mittels dielektrischer Relaxationsspektroskopie nachgewiesen. Folglich gilt der für Ga-DOTA direkt gemessene Diffusionskoeffizient auch für das MR Kontrastmittel Gd-DOTA. Eine direkte Diffusionsmessung in menschlichem Blut war bislang aufgrund des starken ^{1}H Hintergrundsignals nicht möglich. Allerdings konnte mit Hilfe der Stokes-Einstein Gleichung die höhere Viskosität des Blutes korrigiert und der Diffusionskoeffizient abgeschätzt werden: $D_{\mathrm{plasma}} = (2.92 \pm 0.25) \times 10^{-10}\,\mathrm{m^2/s}$.

Im Zuge des »Panini Project« wurde die anisotrope Diffusion von Wassermolekülen in fixierten Gewebeproben des menschlichen Gehirns untersucht. Durch die Verwendung eines hoch-optimierten experimentellen Aufbaus konnten bislang unerreichte räumliche Auflösungen von bis zu 350 µm auf einem 3 T Ganzkörper MR-Tomographen erzielt werden. Die Rekonstruktion von Faserbündeln zeigte eine zuvor unerreichbare Detailtiefe. Allerdings wurde die maximale Winkelauflösung der Faserrekonstruktion von komplexen Mikrostrukturen erheblich durch den Einfluss der Gewebefixierung eingeschränkt. Die Methodik wurde daher auf die Bildgebung von fixierten und frischen Schweineherzen übertragen um den Einfluss der Gewebefixierung genauer zu untersuchen. Außerdem wurde die Existenz eines strukturell stabilen Zustands in unfixiertem Gewebe nachgewiesen wodurch kontinuierliche Bildaufnahmen über 13 Stunden möglich wurden. Die helikale Faserstruktur im Myokard konnte ebenso detailliert dargestellt werden wie die Gefäßwände von Aorta, arteria pulmonalis und der rechten Herzkranzarterie. Die Analyse der sphärisch-harmonischen Energiespektren und der fraktionellen Anisotropie bestätigten eine erhöhte Winkelauflösung in unfixiertem Gewebe. In einem Pilotversuch wurde außerdem die Durchführbarkeit dieser Methode an unfixiertem menschlichem Gewebe demonstriert. Im Gehirn konnten die wichtigsten Faserbündel der weißen Hirnsubstanz bei einer Auflösung von 0.9 mm rekonstruiert werden. Entsprechende Rekonstruktionen im menschlichen Herzen zeigten leider eine etwas geringere Genauigkeit, konnten aber die beiden Ventrikel sowie Bruchstücke zweier Herzkranzgefäße abbilden.

CONTENTS

1 INTRODUCTION 1

I THEORY 3

2 DIFFUSION 5

3 NUCLEAR MAGNETIC RESONANCE (NMR) 9
- 3.1 Principles of NMR Spectroscopy . . . 9
  - 3.1.1 Spin . . . 9
  - 3.1.2 Resonant Spin Excitation . . . 11
  - 3.1.3 Relaxation . . . 12
- 3.2 Chemical Shift . . . 13
- 3.3 Detecting Diffusion with NMR . . . 15

4 MAGNETIC RESONANCE IMAGING (MRI) 19
- 4.1 Principles of MRI . . . 19
  - 4.1.1 Spatial Encoding . . . 19
  - 4.1.2 Image Reconstruction and k-Space . . . 22
  - 4.1.3 Image Contrast . . . 22
  - 4.1.4 Echo Planar Imaging (EPI) . . . 23
  - 4.1.5 Multi-Shot EPI Acquisitions . . . 24
- 4.2 Diffusion-Weighted MRI (DWI) . . . 25
  - 4.2.1 Diffusion-Weighted EPI . . . 25
  - 4.2.2 Apparent Diffusion Coefficient . . . 26
  - 4.2.3 Imaging in the Low-SNR Regime . . . 27
- 4.3 Contrast Agents . . . 28

5 TRACTOGRAPHY 29
- 5.1 Diffusion Tensor Imaging (DTI) . . . 29
- 5.2 Q-Ball Imaging . . . 31
- 5.3 Derived Indices and Quality Measures . . . 33
- 5.4 Fiber-Tracking . . . 34

II DIFFUSIVITY OF METAL-DOTA CHELATES 37

6 METHODS 39
- 6.1 Synthesis . . . 41
- 6.2 ^{1}H NMR Spectroscopy . . . 42
- 6.3 ^{1}H 2D Diffusion Ordered NMR Spectroscopy . . . 42
- 6.4 Dielectric Relaxation Spectroscopy . . . 43

7 RESULTS 45
- 7.1 ^{1}H NMR Spectroscopy . . . 45
  - 7.1.1 Thermal Stability of Ga-DOTA . . . 48
  - 7.1.2 Mass Spectrometry of Ga-DOTA . . . 49
- 7.2 ^{1}H 2D Diffusion Ordered NMR Spectroscopy . . . 50

8 DISCUSSION 53

III HIGH-RESOLUTION EX VIVO DIFFUSION-WEIGHTED IMAGING - THE PANINI PROJECT 57
9 METHODS 59
9.1 DWI of Fixed Human Brain Specimens . . . 59
9.1.1 Experimental Setup . . . 60
The Panini Coil . . . 60
Tissue Specimens . . . 62
Imaging Pulse Sequence . . . 63
Diffusion Sampling . . . 65
9.1.2 Postprocessing . . . 66
9.1.3 Spherical Harmonic Decomposition . . . 69
9.2 DWI of Pig Hearts . . . 70
9.2.1 Comparison of DWI of Fixed and Fresh Tissue . . . 70
9.2.2 DWI of the Unfixed Pig Heart . . . 72
9.3 DWI of Unfixed Human Tissue Specimens . . . 74
10 RESULTS 77
10.1 DWI of Fixed Human Brain Specimens . . . 77
10.1.1 Image Reconstruction . . . 77
10.1.2 Spatial Resolution and SNR . . . 81
10.1.3 Tractography . . . 84
10.1.4 Angular Resolution . . . 88
10.2 Comparison of Fresh and Fixed Pig Hearts . . . 91
10.3 DWI of Unfixed Pig Hearts . . . 92
Image Quality . . . 92
Gradient System Heating . . . 93
Tissue Properties . . . 94
Tractography . . . 94
10.4 DWI of Unfixed Human Tissue Specimens . . . 102
10.4.1 Human Brain . . . 102
10.4.2 Human Heart . . . 106
11 DISCUSSION 111
11.1 DWI of Fixed Human Tissue Specimens . . . 111
11.2 DWI of Unfixed Animal Tissue Specimens . . . 112
11.3 DWI of Unfixed Human Tissue Specimens . . . 113
11.4 Limitations . . . 114

IV CONCLUSION AND OUTLOOK 117
12 CONCLUSION 119
13 OUTLOOK 121
A APPENDIX 123

BIBLIOGRAPHY 129

1

INTRODUCTION

Driven by Brownian motion, diffusion is one of the most fundamental transport mechanisms in the human body and plays a vital role for its functionality. Diffusion occurs on a wide range of length- and time-scales, from the uptake of oxygen in the lung to the diffusion of enzymes and proteins through cell membranes. The diffusion spectrum ranges from isotropic, free diffusion to hindered and restricted diffusion in the presence of boundaries for water displacement. The experiments presented in this thesis investigate diffusion processes in the two extremes of this spectrum.

In Magnetic Resonance Imaging (MRI), contrast agents are routinely used to enhance image quality for a given diagnostic interest. The primary purpose of these agents is to manipulate the signal intensity in the final image to enhance tissue contrast. As part of the blood stream, contrast agents also provide valuable information about perfusion and fluid dynamics. It has been shown that the dispersion of a contrast agent bolus depends on the diffusion coefficient of the applied contrast agent in blood [28, 58]. Although contrast agents are used in widespread MRI applications, information about their diffusivity is surprisingly scarce. This is mainly due to the fact that they contain highly paramagnetic ions to manipulate the relaxivity of protons in their direct vicinity. Because of their short relaxation times contrast agent complexes cannot be observed in Nuclear Magnetic Resonance (NMR) spectroscopy, which is the method of choice to study diffusion in solutions. In the course of this thesis, a new approach to this problem was developed. The proposed method substitutes the paramagnetic ion with another ion of lesser magnetic moment to enable direct NMR observations of the contrast agent complex. The question whether the diffusional behavior of the complex is changed by this substitution is crucial and will be discussed in chapter 8.

The opposite side of the spectrum of diffusion processes is dominated by hindered and restricted diffusion. In the presence of boundaries, such as vessel walls, water displacement is restricted in one or more dimensions. Muscles and neurons are good examples of fibrous tissue where the diffusion of water molecules is anisotropic because of the structure of the surrounding tissue.

In 1965, Stejskal and Tanner showed that diffusion can be observed in NMR spectra using time-dependent magnetic field gradients [67]. This observation marks the beginning of a development which lead to diffusion-weighed MRI (DW-MRI). Based on the diffusion anisotropy in fibrous tissue, DW-MRI is capable of detecting the preferred direction of water displacement in every voxel. This is the foundation for diffusion tractography, a powerful, non-invasive technique to reconstruct fiber

pathways, e.g. in muscles or neurons in the human brain. During the typical time-scale of MRI signal acquisitions in the order of milliseconds, diffusion causes a mean displacement of water molecules in the order of a few micrometers. Therefore, DW-MRI is capable of probing tissue microstructure well below its actual spatial image resolution.

The field of applications for tractography as an emerging technique is steadily expanding. Detailed maps of neuron pathways are currently used to investigate the *Human Connectome*, i.e. the connectivity and routing of neuronal fibers between brain regions [70]. Other studies focus on the benefits of presurgical tractography to identify tissue at risk and to minimize damage to healthy tissue [5, 54].

However, all of the above in vivo applications suffer from the same limitations, namely long acquisition times and motion artifacts. It has been shown that diffusion anisotropy is still present in fixed post mortem tissue and that diffusion tractography can still be performed to investigate the tissue microstructure [68]. This enables the acquisition of high-resolution data sets with minimal motion and susceptibility artifacts. Therefore, ex vivo DWI has the potential to reveal even smaller and more complex fiber architectures than those identified in living subjects. As part of the *Human Connectome Project*, the experiments presented in chapter 9 of this thesis aimed for maximum spatial and angular resolution in DW-MRI of post mortem tissue specimens to advance our understanding of the complex neuron architecture in the human brain.

Part I

THEORY

2

DIFFUSION

Diffusion is a physical process that was discovered by the Scottish botanist Robert Brown (1773-1858) in 1827 when he observed random movement of pollen grains in water [13]. Encouraged by his observation, Brown also verified the same random motion in suspensions of various other organic and inorganic powdered materials. A theoretical explanation of what Brown believed to be proof of animated elementary particles of inorganic and organic matter was given almost 80 years later by Albert Einstein in 1905 [22].

The so-called "Brownian motion" is caused by interactions (i.e. collisions) between particles. Every particle in an ensemble has its own thermal kinetic energy and will travel in a straight line until it collides with another particle. As both the distance and direction of travel between collisions are randomly distributed, the resulting trajectories are often called "random walks". Jean Perrin was one of the first to validate Einstein's predictions by analyzing the statistical distribution of particle displacements in suspensions (cf. Fig. 2.1).

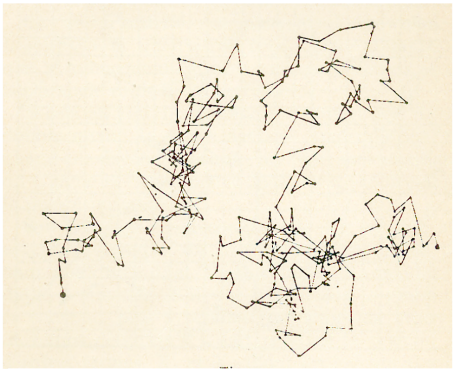

(a) Trace of a single gamboge particle in water as observed over 30 seconds through a simple microscope.

(b) Statistical distribution of displacements along the random trajectory. The circles indicate fractions and multiples of the mean squared displacement.

Figure 2.1: Brownian motion as observed by Jean Perrin in 1913, images reproduced from [55].

Because all particles in the ensemble experience different random trajectories, the expectation value for the overall displacement $\bar{x}$ of the ensemble is always zero

$$\bar{x} = \sum_i \Delta_i = 0 \tag{2.1}$$

where Δ_i are the total displacements of the individual particles after a certain period of time. This means that the center of mass of the ensemble remains stationary in the presence of diffusion. Diffusion will, however, cause an expansion of the system.

The average distance covered before another collision happens is commonly referred to as the mean free travel distance λ. It is mainly given by the particle size and density of the system. Assuming a constant λ for particles on a one-dimensional grid, the Gaussian distribution can be derived by looking at the probabilities of all possible displacements after a certain number of collisions n. After the first collision, the particle will be found at a position of either $+\lambda$ or $-\lambda$ with equal probability of $p = 1/2$. For higher values of n, the distribution is described by Pascal's triangle. For large values of n and divided by 2^n, it approaches a normal distribution (cf. Fig. 2.2).

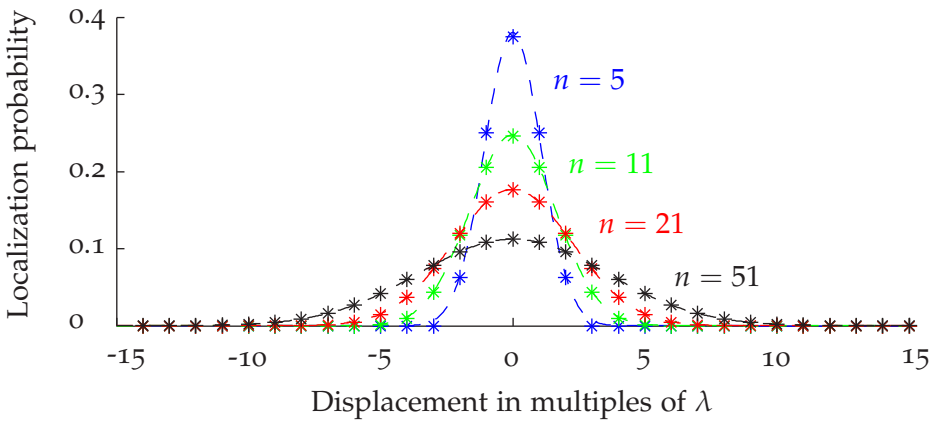

Figure 2.2: Shape of Pascal's triangle for different numbers of collisions and the resulting Gaussian fit functions. The center of mass remains stationary but the system expands with higher numbers of collisions, i.e. time.

It is interesting to see that Pascal's triangle already shows diffusion as the overall distribution becomes broader with an increasing number of collisions which is equivalent to a longer diffusion time. The expansion of a diffusing system is characterized by the mean squared displacement. For the above system in one dimension, the mean squared displacement can be described by

$$\left\langle (x(t) - x_0)^2 \right\rangle = 2Dt \tag{2.2}$$

with D being the diffusion coefficient of the ensemble. In the more general case of three dimensions, equation 2.2 can be written as

$$\left\langle (\vec{r}(t) - \vec{r}_0)^2 \right\rangle = 6Dt \tag{2.3}$$

For particles in solution the diffusion coefficient can be calculated using the Stokes-Einstein equation [22],

$$D = \frac{k_B T}{6\pi\eta r_h} \tag{2.4}$$

where T is the ambient temperature, η the viscosity of the solvent and r_h the hydrodynamic radius of the diffusing particle.

3

NUCLEAR MAGNETIC RESONANCE

3.1 PRINCIPLES OF NMR SPECTROSCOPY

Matter, as we understand it today, is made of atoms which in turn are made of electrons, protons and neutrons. These particles can be described using a variety of physical properties. While mass and charge of elementary particles are relatively easy to grasp because of their presence in everyday life, magnetism and spin are more conceptual. Nuclear Magnetic Resonance involves precise manipulations of nuclear spin states in an object.

3.1.1 *Spin*

The concept of spin is very abstract and requires a solid knowledge of quantum mechanics. However, one can get a decent feeling for spin dynamics by "thinking 'physically' and 'geometrically' about spins without being entirely wrong" [47]. Nuclear spin is often compared to an angular momentum because similar mathematical concepts can be applied. In quantum mechanics, the total angular momentum L_{tot} of a rotating object is quantized as:

$$L_{\text{tot}} = \hbar\sqrt{J(J+1)} \tag{3.1}$$

where J describes the rotational state and can only take integer values. For particles with spin, one can define a total angular momentum of the form :

$$L_{\text{tot}} = \hbar\sqrt{S(S+1)} \tag{3.2}$$

where S is the particle spin. Each elementary particle has an intrinsic spin quantum number S which is either an integer (0,1,2, ...) for bosons or half integer ($1/2$,$3/2$, ...) for fermions. As for angular momentum, there exist $2S+1$ sub-states for a particle with spin S which are energetically degenerate in the absence of an external field but may have different energies if an external field is applied. An important difference between spin and an actual angular momentum is, that a particle does not "gain" spin by rotation, spin is an intrinsic property of each particle.

For atomic nuclei which are composed of protons and neutrons, the nuclear spin state I can be calculated as a combination of proton and neutron spins. Therefore, different isotopes of the same element can have different nuclear spins and magnetic properties. For example, ^{12}C as the most common carbon isotope has a nuclear spin of 0 while ^{13}C has a nuclear spin of $1/2$.

Spin quantum numbers different from zero give rise to a magnetic moment μ. The strength of the magnetic moment is defined as:

$$\vec{\mu} = \gamma \cdot \vec{I} \tag{3.3}$$

where the proportionality constant γ is called gyromagnetic ratio. It is worth mentioning that γ can have negative values (e.g. for electrons) for which the magnetic moment and the spin angular momentum point in opposite directions. This magnetic moment is the basis of Nuclear Magnetic Resonance.

In the following introduction to NMR Spectroscopy, only atomic nuclei with spin $I = 1/2$ will be considered, as only this type is relevant for the experiments presented in this thesis. A more detailed description of NMR on isotopes with spin $I > 1/2$ can be found in the existing literature (e.g. [47]).

In an external magnetic field, the two sub-states of spin $1/2$ atomic isotopes have different magnetic energies. The magnetic energy of a particle with magnetic moment μ in an external magnetic field B_0 can be calculated as:

$$E = -\vec{\mu} \cdot \vec{B_0} \tag{3.4}$$

The negative sign indicates that the energy is minimized when μ and B are parallel. In NMR physics, text books often refer to spin states as "up" and "down" or having "parallel" and "anti-parallel" alignment to the external field. This is a simplified model of the exact quantum mechanical description. All spins in an ensemble constantly change their orientation due to local magnetic field fluctuations. The energy difference between "parallel" and "anti-parallel" alignment of the magnetic moment with the external field introduces a slight bias towards states with parallel projection component. As an ensemble average, this slight bias leads to a macroscopic longitudinal magnetization M_z along the external magnetic field.

However, the two-state model is very efficient in visualizing the most relevant mechanisms in NMR. In the two-state model, the longitudinal magnetization can be expressed as population differences in the two states which are given by a Boltzmann distribution

$$\frac{N_{\text{up}}}{N_{\text{down}}} = \exp\left(\frac{\Delta E}{k_B T}\right) \tag{3.5}$$

with

$$\Delta E = \hbar \gamma B_0 \tag{3.6}$$

being the energy difference between the two states.
In order to use this magnetization for NMR applications, another very important property of spin in an external magnetic field has to be introduced. Instead of simply aligning the magnetic moment to the external field, it will move around the field axis on a cone. This movement is called precession. Many NMR books visualize precession as two cones for the spin states "up" and "down". However, the angle of the precession cone is given by the initial polarization without an external field. For example, if the magnetic moment was already accidentally aligned with the external field axis, they remain perfectly aligned. If the initial angle was about 90°, the precession will occur on a flat disk. The averaged precession angle of the whole ensemble will be in-between these extremes.

The precession frequency ν_0 is given by the following equation and is commonly referred to as the Larmor frequency:

$$\nu_0 = \frac{\Delta E}{h} = \frac{\hbar \gamma B_0}{h} = \frac{\gamma}{2\pi} \cdot B_0 \tag{3.7}$$

Note that at this point, no transverse magnetization can be detected as the transverse components of the magnetic moments are uniformly distributed and average to zero. For ^{1}H nuclei, the Larmor frequency at 3 T is 127.73 MHz.

3.1.2 *Resonant Spin Excitation*

The energy difference ΔE between the two states can be used to drive transitions by resonant excitation using radio-frequency pulses (RF pulses). The resonance condition can be expressed as:

$$h \cdot f = \Delta E = \hbar \gamma B_0 = h \cdot \nu_0 \tag{3.8}$$

where f is the frequency of the applied RF pulse. The effect of this resonant excitation is quite complex and can be described using the density matrix formalism. In the two-state model, resonant excitation triggers a "spin-flip" from the lower energy state to the higher energy state. Additionally, coherences between individual spins are
the magnetic moments. As a consequence, a macroscopic transverse magnetization is created which precesses at the Larmor frequency. This oscillating magnetic field can be detected by the electric current it induces in the receive coils of the NMR spectrometer.

The number of spins affected by the RF pulse depends on the amplitude and duration of the pulse, i.e. its energy. A very important parameter in NMR is the "flip angle" α of the applied RF pulse. It is motivated by the observation that with increasing energy of the RF pulse, the measured transverse magnetization $M_\perp$ is characterized by:

$$M_\perp = M_z \cdot \sin(\alpha) \tag{3.9}$$

where M_z is the initial longitudinal magnetization. $M_\perp$ reaches its maximum at $\alpha = 90°$. In MRI physics, the coordinate system is conventionally chosen to align the z-axis with the direction of the permanent magnetic field B_0. The transverse magnetization then rotates in the xy-plane which is why it is often labeled as M_{xy}.

3.1.3 *Relaxation*

Resonant RF excitation of a spin ensemble represents a disturbance of the thermal equilibrium state. The excited state will return to its thermal equilibrium by the following relaxation mechanisms:

SPIN-LATTICE RELAXATION: In the thermal equilibrium, macroscopic magnetization is only observed in the direction of the external field. This polarization is transferred into the transversal plane by resonant RF excitation, assuming a flip angle of 90°. However, the energy difference of the "up" and "down" spin states remains unchanged and drives the re-establishment of the longitudinal polarization. The energy of excited spins is distributed by interactions with the surrounding "lattice". The longitudinal equilibrium magnetization is re-built with the characteristic relaxation time constant T_1 and can be described by:

$$M_z(t) = M_z^{eq} \cdot \left(1 - e^{-t/T_1}\right) \tag{3.10}$$

where M_z^{eq} is the longitudinal equilibrium magnetization.

SPIN-SPIN RELAXATION: A precessing transverse magnetization requires a large number of spins to precess at the same speed and phase. This spin coherence is created by the resonant RF pulse. As the Larmor frequency of a single particle depends on the local magnetic field, this coherence is very sensitive to magnetic field fluctuations. These fluctuations lead to a gradual de-phasing of excited spins and thus, an exponential decay of the transverse magnetization. The rate at which coherence is lost is given by the characteristic relaxation time constant T_2. The transverse components of the precessing magnetization can be described by:

$$M_x(t) = M_0 \cdot \sin(\omega_0 t) \cdot e^{-t/T_2} \tag{3.11}$$

$$M_y(t) = -M_0 \cdot \cos(\omega_0 t) \cdot e^{-t/T_2} \tag{3.12}$$

where M_0 is the maximum initial transverse magnetization after excitation and $\omega_0 = 2\pi\nu_0$.

Another source for the loss of coherence are field inhomogeneities that lead to local variations of the Larmor frequency. In contrast to field fluctuations, inhomogeneities are static and can be compensated using appropriate imaging pulse sequences. Without compensation, the de-phasing process is accelerated and another time constant, T_2^* with $T_2^* \leq T_2$, replaces T_2 in the above equations.

The most basic NMR pulse sequence consists of a single 90° RF pulse followed by signal detection. The received signal decays with time due to transverse relaxation (cf. Fig. 3.1). This experiment is called free induction decay (FID) and is often used to acquire NMR spectra. The NMR spectrum is calculated from the FID signal using a Fourier transform (FFT).

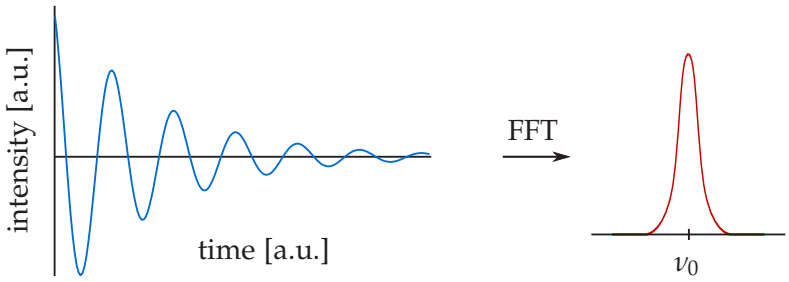

Figure 3.1: Evolution of the received signal in an FID experiment and the resulting NMR spectrum.

3.2 CHEMICAL SHIFT

The local magnetic field at a proton's location can be different from B_0 in the presence of other nuclei with additional magnetic moments and varying electron densities. In fact, multiple protons within the same molecule often experience different local magnetic fields as a result of their chemical coordination. Figure 3.2 shows an exemplary ^{1}H NMR spectrum of ethanol along with its chemical structure. Ethanol shows a total of three signal groups, either as singlets or multiplets. As indicated by their color, the protons of the different groups show different chemical shifts. The resulting ^{1}H NMR spectrum can be seen as a "fingerprint" of the ethanol molecule and provides valuable information about the molecular structure.

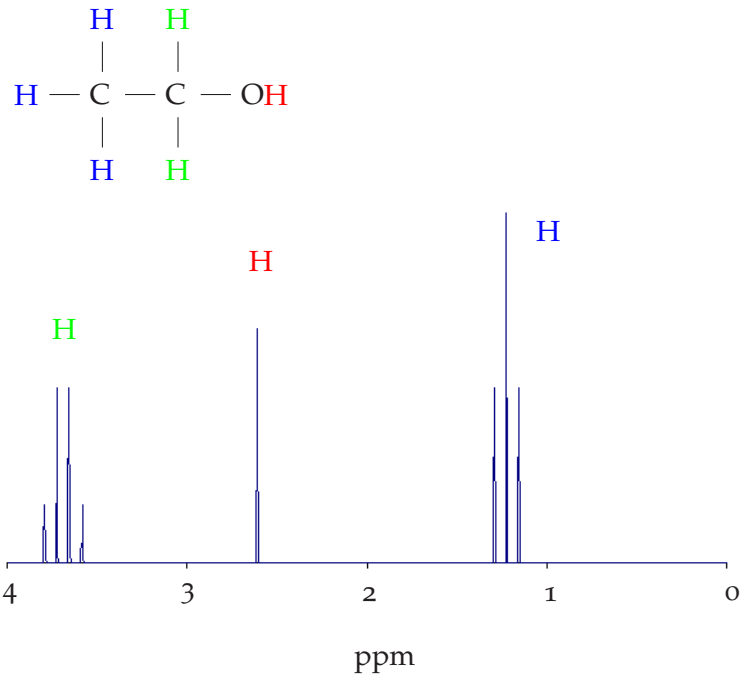

Figure 3.2: ^{1}H NMR spectrum and structure of ethanol. Peaks are color-coded to show contributing proton locations. Spectrum reproduced from the *AIST Spectral Database* (http://sdbs.db.aist.go.jp).

Although the chemical shift describes a shift in the Larmor frequency, the absolute frequency is rarely used to characterize shifts in NMR spectroscopy. The reason for this is that according to Eq. 3.7, the frequency shift depends on the strength of the external magnetic field and can not directly be compared between systems with different magnetic field strengths. A solution to this problem is the parts-per-million (ppm) scale which is defined as:

$$\text{shift} = \frac{\text{signal frequency} - \text{reference frequency}}{\text{spectrometer frequency}} \cdot 10^{-6} \quad [\text{ppm}] \tag{3.13}$$

The reference frequency is the resonance frequency of a standard solution and depends on the detected nucleus. For ^{1}H and ^{13}C NMR, the single resonance of Tetramethylsilan (TMS) is defined as 0 ppm. TMS has the advantage of being chemically inert which means that it can be added to most samples for referencing without changing the NMR results of the sample. It is also very fugitive, which makes it easy to remove TMS after the NMR experiments.

3.3 DETECTING DIFFUSION WITH NMR

As diffusion occurs on the microscopic level of individual molecules, the spatial resolution of NMR is not sufficient to observe diffusion directly. However, the diffusion of a macroscopic ensemble of molecules or spins can be observed in the evolution of NMR signals.

In order to sensitize an NMR pulse sequence to diffusion, the spin ensemble in a target volume has to be observed at two different points in time. The target volume in NMR is usually the active volume of the spectrometer coil. In Magnetic Resonance Imaging the target volumes are usually image voxels. Diffusion is then observed indirectly by measuring the signal attenuation that is caused by spins diffusing out of the target volume during a defined diffusion time Δ (c.f. Fig. 3.3).

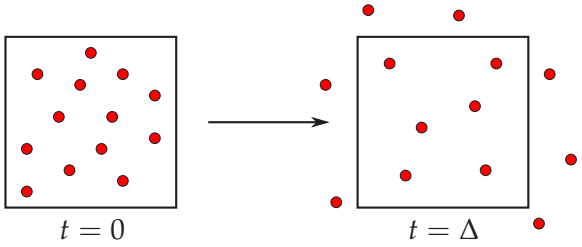

Figure 3.3: Gaussian diffusion leads to an expansion of the observed spin ensemble. At $t = \Delta$, some spins have diffused out of the volume which results in an attenuation of the received NMR signal from that volume. The degree of the attenuation depends on the expansion speed which is given by the diffusion coefficient D.

Detection of diffused spins is implemented by adding a pair of balanced magnetic field gradients to the pulse sequence. The first gradient lobe de-phases spins along the direction of the gradient axis. The second gradient is usually applied with inverted polarity and re-phases spins along the same direction (bipolar gradients). As seen in Fig. 3.3, the spin ensemble initially "labeled" by the first gradient will have spread during the diffusion time Δ. Therefore, the second gradient will only be able to completely re-phase the portion of spins that haven't traveled out of the target volume. This leads to an attenuated signal in comparison to the same experiment without diffusion encoding gradients. Alternatively, the two gradients can be placed around an inversion pulse and are then applied with the same polarity to yield the same effect (monopolar gradients). Bipolar gradients tend to create weaker eddy currents, i.e. currents in the spectrometer or MRI hardware or patient that are induced by switching the gradients. On the other hand, bipolar gradients can also add artifacts due to differences in gradient performance at positive and negative polarity. A spin echo has the additional advantage of compensating the T_2^* relaxation due to magnetic field inhomogeneities.

It is essential for the experiments presented in this thesis, that water diffusion is only observed in the direction of the diffusion encoding gradient. While this may seem to be a limitation at first, the additional directional (or angular) information is extremely valuable and will be the basis for MR tractography.

The diffusion-induced signal attenuation can be described by the Stejskal-Tanner equation which links the diffusion coefficient to the NMR signal intensity [67]:

$$S = S_0 \cdot \exp(-b \cdot D) \tag{3.14}$$

where S_0 is the signal intensity without diffusion weighting, S the attenuated signal, D the diffusion coefficient and b a pulse sequence specific parameter describing the degree of diffusion weighting. In every diffusion-weighted experiment, a reference acquisition without diffusion encoding gradients has to be performed to measure S_0.

The "b-value" for an arbitrary gradient waveform $G(t)$ along a single axis is defined as:

$$b = \gamma^2 \int_0^{TE} \left[\int_0^t G(t')dt' \right]^2 dt \tag{3.15}$$

The b-values is usually given in s/mm^2. In the case of trapezoidal gradient waveforms, the integral in Eq. 3.15 can be evaluated to a form that is more intuitive and allows for a direct calculation of b from pulse sequence parameters:

$$b_{\text{trap}} = \gamma^2 G^2 \left[\delta^2 \left(\Delta - \frac{\delta}{3} \right) + \frac{\xi^3}{30} - \frac{\delta \xi^2}{6} \right] \tag{3.16}$$

where G is the gradient amplitude, Δ the spacing of the two gradients which is equivalent to the diffusion time, δ the duration of each gradient and ξ the ramp duration (cf. Fig. 3.4b). Therefore, signal attenuation will be stronger when the gradients are placed further apart (i.e. longer diffusion time) or gradient amplitudes are increased (i.e. higher spatial sensitivity to residual phase of diffused spins).

Rectangular gradient waveforms are an approximation that is often used when gradient rise times are small compared to the gradient duration. In this case, ξ can be neglected and Eq. 3.16 reduces to:

$$b_{\text{rect}} = \gamma^2 G^2 \delta^2 \left(\Delta - \frac{\delta}{3} \right) \tag{3.17}$$

The diffusion coefficient in NMR experiments is routinely measured by repeating the same experiment with different diffusion gradient amplitudes which is essentially a variation of the b-value. Fitting of Eq. 3.14 to the data points does then yield D as one of the fitting parameters.

(a) Rectangular gradient waveform

(b) Trapezoidal gradient waveform

Figure 3.4: Timing parameters of the two most commonly used monopolar diffusion gradient waveforms.

4

MAGNETIC RESONANCE IMAGING

4.1 PRINCIPLES OF MRI

Magnetic Resonance Imaging (MRI) is a technique that is based on Nuclear Magnetic Resonance but allows for 3D mapping of the received signal's origin. Much like in NMR, resonant RF pulses are used to create a precessing transverse magnetization in the imaged object which is detected by receive coils. For the experiments in this thesis, the detected nucleus was always ^{1}H, which is mainly present in the form of H_2O molecules.

4.1.1 *Spatial Encoding*

In order to calculate the origin of an RF signal in 3D space, three encoding steps are usually performed. Without loss of generality, the gradient axes in the following description are chosen to align with the principal directions of the MRI system.

1. SLICE ENCODING: Most MRI pulse sequences acquire images in a slice-wise fashion. Individual slices in a 3D object can be selectively excited by applying a magnetic field gradient at the same time as the RF excitation pulse. The field gradient G_z changes the local magnetic fields along its axis and introduces a dependency of the local Larmor frequency on the position along the gradient.

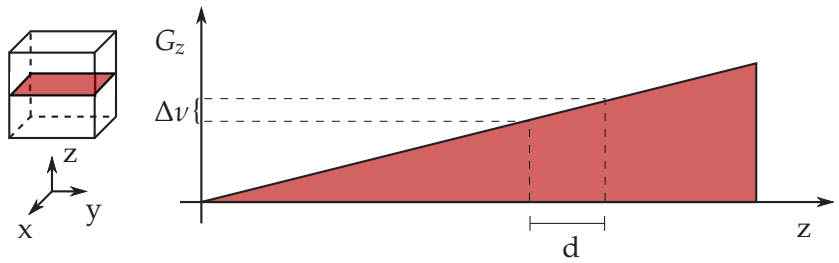

Figure 4.1: Slice Encoding: Only spins in a plane perpendicular to the gradient axis are excited by the RF pulse.

As a consequence, an RF pulse of frequency f_0 will only match the Larmor frequency ν_0 of protons in a slice perpendicular to the gradient direction:

$$\nu_0(z) = \frac{\gamma}{2\pi} \cdot (B_0 + z \cdot G_z) \stackrel{!}{=} f_0 \tag{4.1}$$

However, real RF pulses consist of a whole band of frequencies which can be described by the bandwidth $\Delta\nu$. As a result, the resonance condition to excite precessing spins is met by a whole volume rather than an infinitely narrow slice (cf. Fig. 4.1). The thickness d of the selected slice is given by the shape and bandwidth of the applied RF pulse (cf. Fig. 4.1). The so-called "slice profile" describes the transition between excited spins in the selected slice and "thermal" spins around it. If the transition is very sharp, then the selected slice is well defined and volumes from within this slice contribute equally to the received signal. If the transition is smooth, the number of excited spins will be higher in the center of the slice and will decrease gradually towards its edges. The relation between the slice profile and the RF pulse shape is a Fourier transform. The ideal pulse for a rectangular slice profile is *sinc*-shaped. However, in reality the pulse has a certain length and has to be truncated. Figure 4.2 shows some examples of pulse shapes and the resulting slice profiles. Theoretically, any desired slice profile and even multiple slices can be excited using more advanced pulse shapes [21].

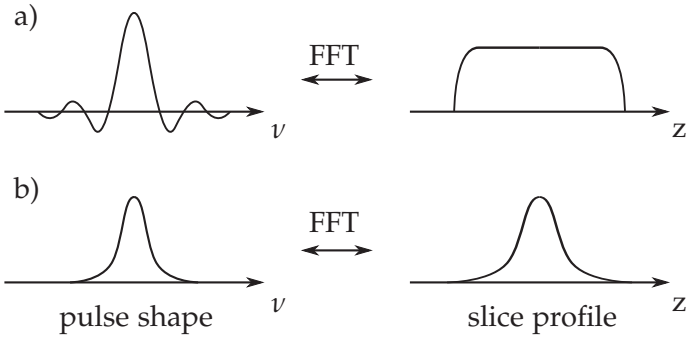

Figure 4.2: Fourier transform relation between the slice profile and RF pulse shape. a) A truncated $\mathrm{sinc}(x)$ pulse creates an almost rectangular slice profile. b) A Gaussian pulse shape leads to a Gaussian slice profile.

2. PHASE ENCODING: In-plane spatial encoding is based on the two defining properties of the NMR signal, its phase and frequency. The second encoding step is usually the phase encoding, which is applied just before the signal is acquired. The phase encoding gradient G_x is turned on for a certain period of time t_{PE} and causes a dependency of the signal's phase on the location along the gradient axis.

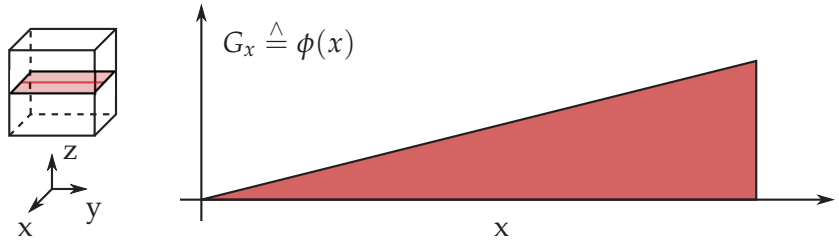

Figure 4.3: Phase Encoding: The spin location along the gradient axis is encoded in the phase of the spin precession.

$$\nu_0(x) = \frac{\gamma}{2\pi} \cdot (B_0 + x \cdot G_x) \tag{4.2}$$

$$\phi(x) = 2\pi \cdot \nu_0(x) \cdot t_{PE} \tag{4.3}$$

3. FREQUENCY ENCODING: The third encoding step is performed at the same time as the signal is detected by the receive coils and recorded by the analog-to-digital converter (ADC). The frequency encoding gradient G_y is applied along the remaining axis and leads to a dependency of the signal's frequency on the location along the gradient axis.

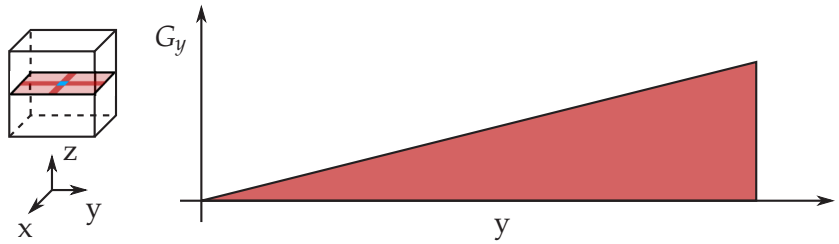

Figure 4.4: Frequency Encoding: The spin location along the gradient axis is encoded in the frequency of the received signal.

$$\nu_0(y) = \frac{\gamma}{2\pi} \cdot \left(B_0 + y \cdot G_y\right) \tag{4.4}$$

4.1.2 *Image Reconstruction and k-Space*

The received signal is spatially encoded by its phase and frequency. In MRI, the phase/frequency domain is called k-space because every point in k-space can be described by a wave vector $\vec{k}$. Spatial encoding, as described above, samples the full frequency spectrum for one specific phase that is set by the phase encoding gradient amplitude. As a consequence, the measured signal is represented by a line in k-space (cf. Fig. 4.5). In order to sample the full k-space, several acquisitions, so-called phase-encoding steps, have to be performed. The final MRI image can then be reconstructed from k-space by a 2D Fourier transform.

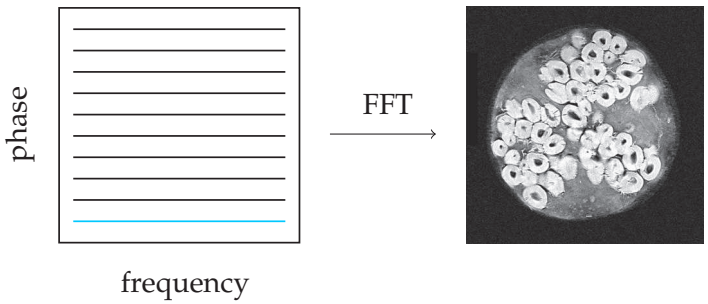

Figure 4.5: Every line in k-space is acquired with a separate measurement. The MRI image is then reconstructed from full k-space by a 2D Fourier transform.

4.1.3 *Image Contrast*

The contrast of MRI images depends on a variety of sequence parameters and can be tuned to a particular diagnostic interest. Assuming that all spins contribute equally to the received signal, the signal intensity in each image voxel is determined by the spin density within the voxel. The resulting image is then "proton density" (PD) weighted.

As described in chapter 3.1.3, the transverse magnetization decays exponentially with a time constant T_2 or T_2^*, depending on the sequence type. Both constants are characteristic for the imaged tissue and can vary significantly within the imaged object or patient. If the MR signal is acquired at time t, the signal may have decayed to different degrees in different areas which leads to an additional weighting of the image intensity. This type of contrast is called T_2 or T_2^* weighting. As this contrast requires a certain time to allow the signal to decay, it is observed when the echo time (TE) is long compared to T_2 or T_2^*.

The received signal also depends on the available longitudinal magnetization at the time of excitation (cf. M_0 in Eq. 3.12). This can be used to introduce signal weighting based on T_1 when the system is not in the thermal equilibrium state. This effect is observed when the repetition time (TR) is short compared to the T_1 of the imaged tissue. At the time of excitation, the longitudinal magnetization of different tissues has then been recovered to different degrees from the previous excitation. This leads to an additional signal weighting according to the local T_1 value.

4.1.4 *Echo Planar Imaging*

In MRI, a wide range of pulse sequences were developed for various applications in both research and clinical routine. One of the most popular pulse sequences is the echo planar imaging (EPI) sequence (cf. 4.6). EPI sequences are very time efficient and are capable of acquiring whole 3D volumes with a single "shot" [48, 63]. Technically, EPI only defines the signal acquisition scheme and can be used with almost any form of signal preparation. As all of the imaging experiments presented in this thesis were performed using different variations of the EPI readout, only this sequence type will be explained in more detail here.

Instead of encoding and sampling a single line of k-space at a time, EPI readouts use very fast balanced gradient pairs to create multiple echoes within a single readout. Each of these gradient echoes is used to sample one line of k-space which allows for full k-space sampling in one shot if enough echoes can be produced.

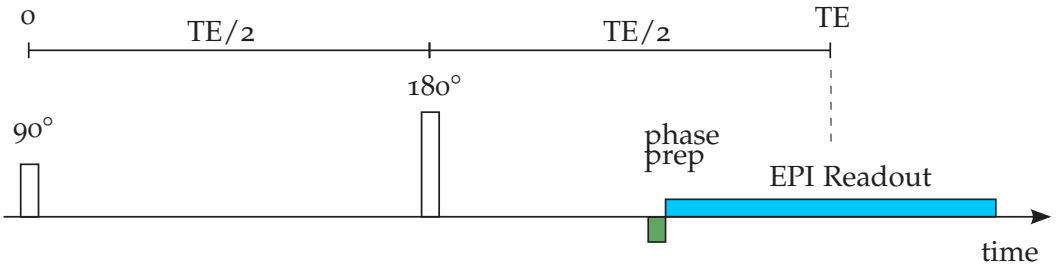

Figure 4.6: Schematic representation of a 2D EPI spin echo pulse sequence. The 180° inversion pulse creates a signal echo at *TE*. The EPI readout is centered around *TE* so that the center of k-space is sampled at the maximum echo intensity.

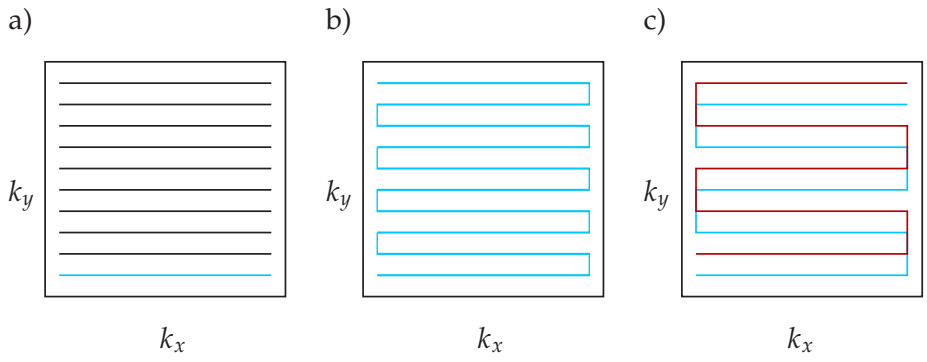

Figure 4.7: K-space sampling schemes of a) a traditional single-line sequence, b) a sequence using the EPI readout to sample the full k-space with a single shot and c) a multi-shot EPI readout.

As seen in Fig. 4.7 b), k-space is filled with a single readout echo train. K-space lines acquired with even echo numbers are acquired in reverse direction than those with odd echo numbers. When the image is reconstructed from k-space using a 2D Fourier transform, those lines have to be flipped. This can lead to inconsistent

phase errors due to eddy currents, B_0 field inhomogeneity or different gradient performance at positive and negative gradient polarity.

For a constant phase error ϕ between odd and even lines in k-space, the reconstructed image I' will be modulated as:

$$I'(x,y) = I(x,y) \cdot \cos(\phi) + iI(x, y - \frac{N_y}{2}) \cdot \sin(\phi) \tag{4.5}$$

with $I(x,y)$ being the ideal image and N_y the image matrix size in the phase-encoding direction [10]. The overall image intensity of the ideal image is reduced by a factor of $\cos(\phi) \leq 1$ which leads to losses in the signal-to-noise ratio (SNR). Furthermore, a second image or "ghost" with a shift of $N_y/2$ and modulated by $\sin(\phi)$ will be superimposed on the ideal image. This artifact which is very common in EPI images is often called Nyquist or "N-over-two" ghosting. Usually, the ghost intensity can be reduced to less than 10 % by correcting for those phase errors.

4.1.5 *Multi-Shot EPI Acquisitions*

Although EPI readouts are very time efficient, the total readout duration can become very long for high image resolutions where many lines have to be acquired. This leads to longer echo times and thus, reduced SNR due to T_2 signal decay. Furthermore, T_2 decay during signal acquisition can introduce errors in k-space which lead to so-called T_2 blurring of the reconstructed image. It can therefore be desirable to split k-space acquisition into multiple shots (cf. Fig. 4.7 c). This prolongs the total acquisition time per slice but also reduces the effects mentioned above.

There are two options to split k-space sampling, along either the phase or the frequency encoding direction. When k-space is sampled using segmented readouts, the full k-space is composed of multiple sets of lines that can introduce phase errors in the same way as previously described for odd and even echoes.

In order to improve the phase correction and reduce the level of ghosting in the image, phase navigators can be used. Phase navigators are additional lines that are acquired just after excitation and contain information about phase drifts between shots.

4.2 DIFFUSION-WEIGHTED MRI (DWI)

Basically any imaging pulse sequence can be sensitized to diffusion by adding a pair of magnetic field gradients in the same way as described for NMR spectroscopy in chapter 3.3. Equation 4.6 represents the basic principle of diffusion-weighted MRI and links the diffusion coefficient D to an image property, the signal intensity of every voxel. Therefore, MRI is capable of mapping the local diffusion coefficients of the imaged object along a defined axis in 3D space.

$$S = S_0 \cdot \exp\left(-b \cdot D\right) \tag{4.6}$$

4.2.1 *Diffusion-Weighted EPI*

Most DWI pulse sequences are based on the EPI readout described in chapter 4.1.4. Figure 4.8 shows a 2D EPI sequence which was modified to be sensitive to diffusion. An additional monopolar diffusion encoding gradient pair and phase navigators were added. The phase navigator collects valuable information about the relative phases of consecutive shots in multi-shot acquisitions. This information is necessary to reduce the ghosting level when the full k-space is reconstructed from individual shots. It is important to note that the direction of the diffusion gradient axis defines the direction in which diffusion can be observed.

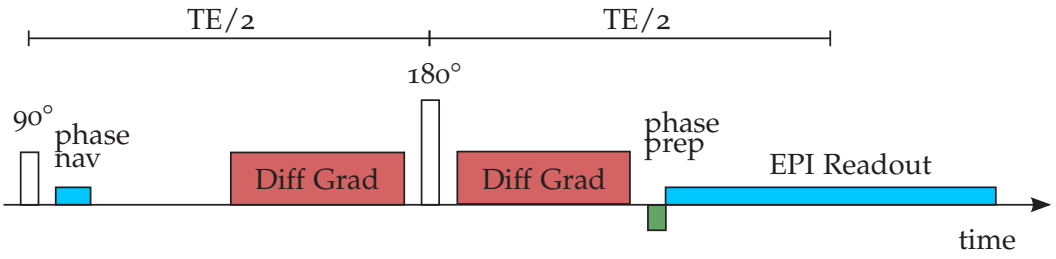

Figure 4.8: Schematic representation of a 2D diffusion-weighted multi-shot EPI imaging pulse sequence. This sequence is based on Fig. 4.6 with additional diffusion encoding gradients and phase navigators.

The maximum gradient slew rate is often not used in diffusion acquisitions as it greatly contributes to $\delta B/\delta t$, which can cause nerve stimulation and stronger eddy currents. The desired reduction of the minimum echo time is often very small and does not justify using the maximum slew rate. DWI can also be performed using other sequence types like steady-state free precession (SSFP) which provides shorter echo times at the cost of control over the b-value [50, 16].

4.2.2 *Apparent Diffusion Coefficient (ADC)*

So far, diffusion was assumed to be purely Gaussian. However, in the presence of boundaries such as vessel or fiber walls, the diffusion model has to be expanded to account for restricted and hindered diffusion.

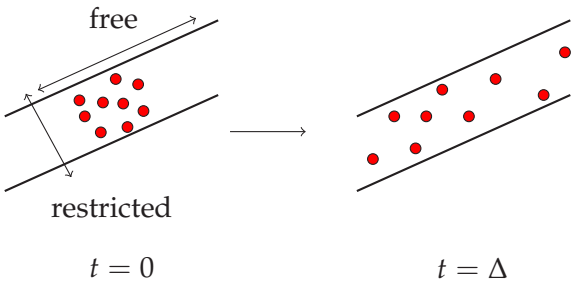

Figure 4.9: Restricted Diffusion in the presence of boundaries: The measured apparent diffusion coefficient (ADC) depends on the direction in which it is observed.

Figure 4.9 shows an exemplary geometry in which diffusion is restricted by vessel walls. As a result, the apparent diffusion coefficient (ADC) in NMR or MRI experiments will depend on the direction of the applied diffusion encoding gradient. If the gradient axis aligns with the fiber direction, diffusion will be observed as if it was free. The measured signal will be strongly attenuated by diffusion. On the other hand, if the gradient axis is perpendicular to the fiber orientation, the labeled spins cannot travel freely and the signal will be less attenuated. Additionally, the observed or apparent diffusivity will depend on the diffusion time Δ because it limits the mean squared displacement. For very short diffusion times, diffusion may still appear to be unrestricted because the water molecules don't have enough time to bounce back from the vessel wall.

The choice of the right b-value in DW-MRI is still a topic of current research studies [39, 42], but it can be estimated from the apparent diffusion coefficient in the target region. From equation 4.6 follows that the product of b and D has to be equal to $-\log(1/2)$ for a signal attenuation of 50%. Therefore, the b-value has to be tuned to each specific experiment. Especially in ex vivo imaging, where diffusion coefficients are substantially lower than in vivo, high b-values are needed to achieve sufficient diffusion weighting.

4.2.3 *Imaging in the Low-SNR Regime*

As seen in the previous section, the diffusion information in diffusion-weighted MR imaging is encoded by an attenuation of the received signal. This, in combination with high spatial resolution, often leads to images with very low SNR.

It has been shown that noise in magnitude images with low SNR values can introduce a significant bias due to its non-Gaussian distribution [30]. While white noise in complex signals can be described by a Gaussian distribution with mean value of zero, this doesn't hold true for magnitude images where noise can only take positive values. Therefore, pure noise in magnitude images is better described by a Rayleigh distribution. As seen in Fig. 4.10, the mean value of the Rician probability distribution of the measured pixel values diverges from the true SNR for low SNR values. The impact of this potential bias on the results of this thesis will be discussed in chapter 11.

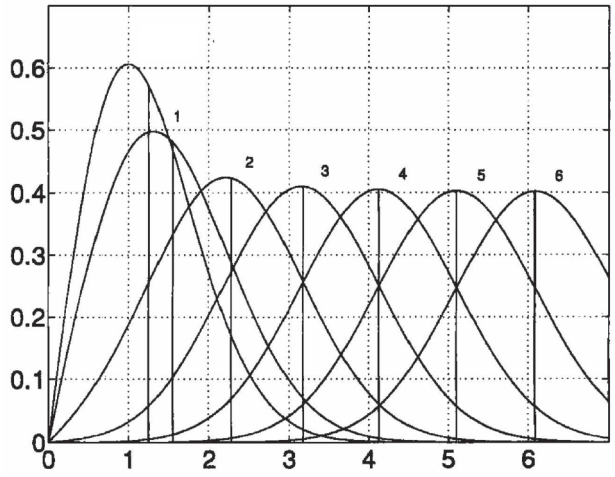

Figure 4.10: Rician distribution of the measured signal in magnitude MR images at different signal-to-noise ratios. For small SNR values, the mean SNR as depicted by the solid vertical lines is greater than the true SNR. Image reproduced from [30].

4.3 CONTRAST AGENTS

As described in section 4.1.3, MRI pulse sequences can be modified to show different image contrasts which is often helpful in medical diagnostics. In addition to this, image contrast can also be influenced by contrast agents which have to be administered to the patient or subject.

Most contrast agents are based on the mechanism of longitudinal relaxation (T_1). This mechanism is usually driven by moving molecules which create a fluctuating local magnetic field. This field then triggers the return or relaxation of an excited spin ensemble to its equilibrium state. This process can be accelerated by adding molecules with strong magnetic moments which amplify the local field fluctuations. Most MRI contrast agents contain metal ions which have unpaired electrons and thus, strong magnetic moments. In an imaging pulse sequence with a short repetition time, only protons in the vicinity of the contrast agent will have returned to their equilibrium state at the time of the next excitation pulse (i.e. T_1 weighting). As a result, areas with contrast agent will appear brighter in T_1-weighted sequences. Unlike in other imaging techniques, MRI contrast agents are not directly visible on the final image, only their influence on neighboring protons is detected. Some exceptions exist where the image contrast is based on non-proton nuclei or hyperpolarized media such as ^{3}He or PHIP agents [27, 38, 31].

Gd^{3+} is the most prominent ion which is used in MRI contrast agents as it has a total of seven unpaired electrons. This drastically increases the relaxivity of water protons in the direct vicinity of the Gd^{3+} ion. Unfortunately, this also makes the ion very toxic which creates the need for protection mechanisms.

The most commonly used contrast agent of this class is Gd-DOTA (brand name DOTAREM ©, Guerbet, USA) where the Gd^{3+} ion is incorporated into the cavity of the DOTA chelator (DOTA = 1,4,7,10-tetraazacyclododecane-1,4,7,10-tetraacetic acid). The crystal structure of Gd-DOTA is shown in Fig. 4.11.

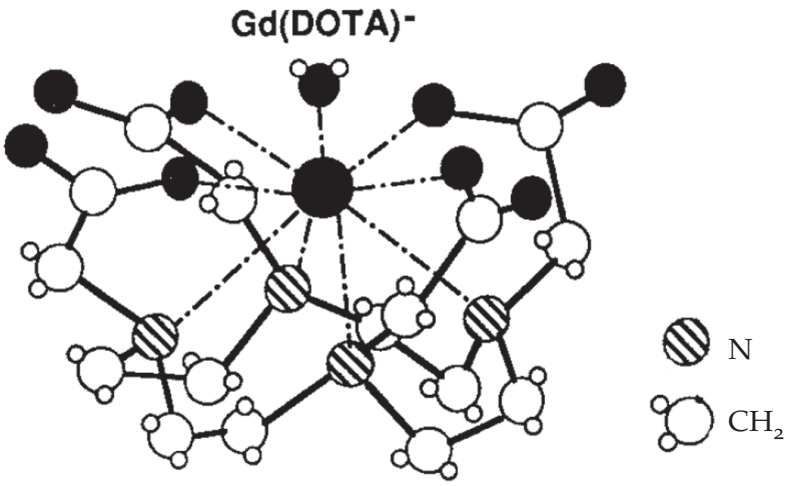

Figure 4.11: Crystal structure of Gd-DOTA [9]. The image was modified to show a legend.

5

TRACTOGRAPHY

The expression tractography generally refers to the process of reconstructing the orientation and connectivity of (fiber) tracts from a given set of information. In the case of MR tractography, the directional diffusion information from diffusion-weighted MR images is used to reconstruct the most likely directions of water displacement. The central assumption in MR tractography is, that the observed dependency of the apparent diffusion coefficient on the direction of the applied diffusion gradients is a result of the underlying microstructure. Although the exact mechanism is still a topic of present research studies, it is generally accepted that the preferred diffusion orientation(s) in each voxel align with fibers in the imaged tissue.

The orientation distribution information of the imaged tissue is not directly accessible from the diffusion-weighted MR images. In order to reconstruct the orientation distribution functions (ODF) of each image voxel, a series of post-processing steps has to be performed depending on the applied diffusion model.

5.1 DIFFUSION TENSOR IMAGING

In diffusion tensor imaging (DTI), water displacement in each image voxel is represented by a symmetric 3-dimensional tensor. As a consequence, this tensor can be fully determined by six independent measurements for the three diagonal elements and three off-diagonal elements. Upon diagonalization of the tensor, the three resulting eigenvalues λ_i can be used to visualize water displacement as an ellipsoid.

$$D = \begin{pmatrix} a_{11} & a_{12} & a_{13} \\ a_{21} & a_{22} & a_{23} \\ a_{31} & a_{32} & a_{33} \end{pmatrix} \quad \Rightarrow \quad D_{\text{diag}} = \begin{pmatrix} \lambda_1 & 0 & 0 \\ 0 & \lambda_2 & 0 \\ 0 & 0 & \lambda_3 \end{pmatrix} \tag{5.1}$$

For isotropic diffusion, all eigenvalues will be equal as there is no preferred direction of water displacement. The resulting orientation distribution function will be a sphere (cf. Fig. 5.1). In the presence of boundaries that restrict diffusion in certain directions, the eigenvalues of the diffusion tensor will point in the main diffusion direction.

Although DTI has been successfully applied to reconstruct and visualize fiber orientations in many parts of the human body [25, 64], one major caveat prevents its use for resolving complex microstructures in research applications.

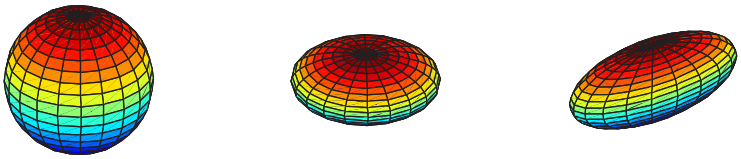

$\lambda_1 = \lambda_2 = \lambda_3 = 1$ $\lambda_1 = \lambda_2 = 1$, $\lambda_3 = 0.4$ $\lambda_1 = 1$, $\lambda_1 = \lambda_2 = 0.4$

Figure 5.1: Visualization of the diffusion tensor eigenvalues as ellipsoids for a) isotropic diffusion, b) diffusion restricted in one dimension and c) diffusion restricted in two dimensions.

Diagonalization of the diffusion tensor yields the main diffusion direction, or the most likely direction of water displacement in every imaged voxel. The underlying assumption is that image voxels only contain a single fiber population. This may be true for voxels in large fiber bundles like the corpus callosum or corticospinal tract (CST), but there are many other regions where multiple fiber pathways are present within the same voxel. This is particularly true at low spatial resolutions with large voxels, having a higher probability to contain multiple fiber bundles. Figure 5.2 shows an examplary DTI reconstruction of two voxels containing crossing fibers.

(a) Fiber bundles crossing at an angle of 90° and the resulting DTI ODF.

(b) Fiber bundles crossing at an angle of less than 90° and the resulting DTI ODF.

Figure 5.2: Schematic DTI reconstructions of image voxels containing multiple fiber orientations. The DTI ODFs in both cases do not represent the correct underlying fiber structures. At a crossing angle of 90°, DTI does not even detect diffusion anisotropy. It is assumed that both fiber bundles have identical diffusion properties.

5.2 Q-BALL IMAGING

The inability of DTI to resolve multiple fiber orientations within single voxels precludes its use in many scientific applications. Soon after the shortcomings of DTI became obvious, more advanced methods like Q-Ball imaging (QBI), diffusion spectrum imaging (DSI) and high angular resolution diffusion-weighted imaging (HARDI) were presented. All these methods try to use the full spectral information from the diffusion-weighted images to accurately reconstruct the true ODFs. For a better understanding of the differences of the above methods, the concept of q-space has to be introduced. Very much like k-space for spatial encoding, q-space can be seen as the diffusion-encoding space. In q-space, each diffusion measurement is represented by a vector q that points in the direction of the diffusion encoding gradient. The length of the vector is given by the q-value which is equivalent to the b-value.

DSI is very similar to traditional k-space sampling in the way that q-space is sampled on a Cartesian grid. Although the whole q-space is sampled, the sample density is often quite sparse and strong gradients are needed for the edges of q-space. The water displacement probability distribution function (PDF) of each voxel can be calculated directly from the sampled q-space by a Fourier transform. This technique avoids the use of specific models for the underlying diffusion process.

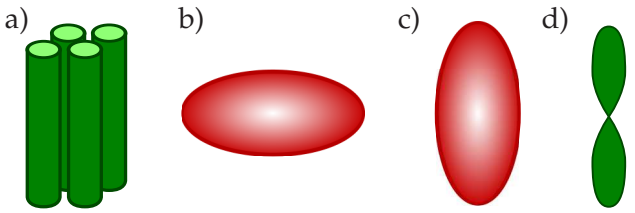

Figure 5.3: Exemplary ODF reconstruction steps for a coherent fiber bundle (a): The measured signal intensity distribution (b) is converted into a water displacement probability distribution function (PDF)(c). From the PDF, the orientation distribution function (ODF)(d) is extracted by isolating the detected PDF maxima.

In Q-Ball imaging, only one b-value is used for each gradient direction. The sampled points of q-space form a sphere (or shell) with radius q, hence the name Q-Ball [73]. The main advantage of sphere sampling is that the "PDF surface" is sampled directly. Also, a definition of angular resolution, that is, the ability to distinguish multiple fiber orientations, is more intuitive when data points are sampled on a single sphere rather than all over q-space. Additionally, the b-value can be chosen to tune diffusion sensitivity to a specific length scale.

Reconstruction of the ODF from the measured MR signal employs the spherical harmonics (SH) basis [32, 19]. The measured MR signal $E(q)$ is expanded into a SH series of order L:

$$E(q) = \sum_{l=0}^{L} \sum_{m=-l}^{l} c_l^m Y_l^m(q) \tag{5.2}$$

where c_l^m denote the spherical harmonic coefficients and Y_l^m the spherical harmonic basis functions of order l and degree m. As the spherical harmonics form a complete basis set for a sphere, any finite-energy ODF can be represented by a linear combination of spherical harmonic functions given a sufficiently large order L. The final ODF in direction (θ, ϕ) can be analytically calculated as:

$$\Psi(\theta, \phi) = \sum_{l=0}^{L} \sum_{m=-l}^{l} 2\pi P_l(0) c_l^m Y_l^m(\theta, \phi) \tag{5.3}$$

with P_l the Legendre polynomial of order l [32]. Another advantage of the spherical harmonics representation is that the achievable angular resolution can be expressed as a function of the harmonic series order L by analyzing the point-spread-function of the reconstruction (cf. Fig. 5.4).

In order to resolve small variations in the angular diffusion profile, the expansion into spherical harmonics needs to represent these high frequency components. Therefore, higher orders in the expansion correspond to finer angular features. However, in order to determine the higher-order components in the expansion, more diffusion samples in q-space are needed.

The contribution of each order to the spherical harmonics expansion is given by its coefficients c_l^m. In order to resolve complex fiber structures and small crossing angles, non-vanishing energy fractions in the higher orders of the expansion are required. The energy fraction of each order in the reconstruction is defined as:

$$E_l = \frac{1}{E_T} \sum_{m=-l}^{l} 4\pi^2 P_l(0)^2 c_l^{m2} \tag{5.4}$$

with E_T being the total energy up to the highest order in the expansion [32]. The resulting power spectrum can be used to analyze the complexity of the measured signal and to evaluate the achievable angular resolution.

Angular resolution also depends on the b-value because strong attenuations are needed to induce sufficient contrast between neighboring points on the sphere. The term “diffusion contrast” will be used throughout this thesis to describe the amplitude of variations in the PDF or ODF.

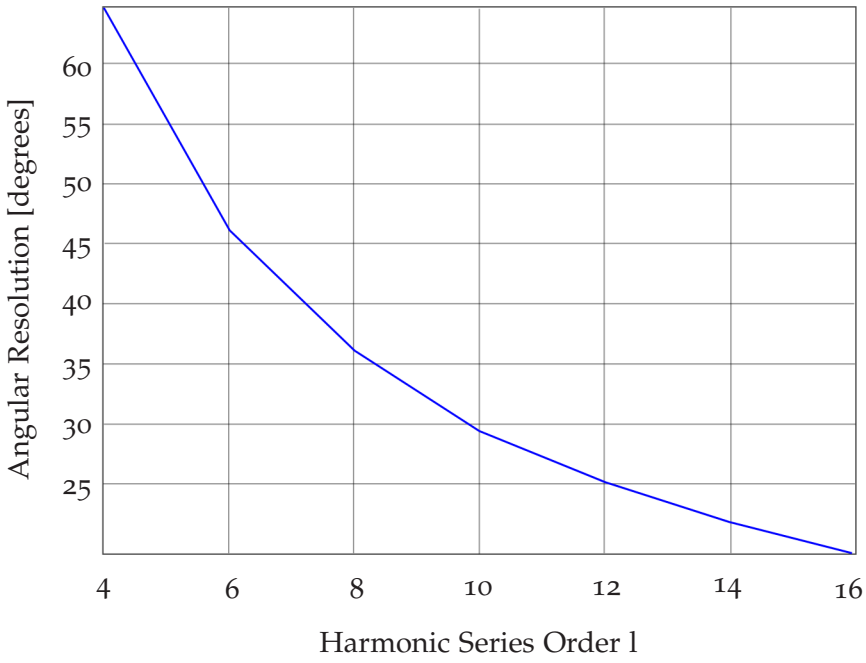

Figure 5.4: Angular resolution in the ODF reconstruction using the spherical harmonics basis as a function of the harmonic series order L. Image reproduced from [32].

5.3 DERIVED INDICES AND QUALITY MEASURES

For clinical applications of MR tractography, quantitative metrics that can be compared between patients and healthy subjects are needed. The following paragraphs are intended to introduce the most relevant and specific metrics for the assessment of tissue integrity and disease in DWI.

FRACTIONAL ANISOTROPY: Fractional anisotropy (FA) is the most commonly used parameter to quantify the degree of anisotropy in DTI tensor representations. FA is rotationally invariant and robust in low-SNR acquisitions [56]. It is a very sensitive marker for microstructural changes at the level of fibers, but not for the type of change. It also provides a valuable threshold parameter for fiber-tracking algorithms, as it can be used to distinguish between areas with isotropic and restricted diffusion. Fractional anisotropy is defined as:

$$\mathrm{FA} = \sqrt{\frac{3}{2}} \cdot \sqrt{\frac{\sum_{i=1}^{3} (\lambda_i - \mathrm{tr}(\lambda))^2}{\sum_{i=1}^{3} \lambda_i^2}} \tag{5.5}$$

with the tensor trace

$$\mathrm{tr}(\lambda) = \sum_{i=1}^{3} \lambda_i \tag{5.6}$$

GENERALIZED FRACTIONAL ANISOTROPY: Because FA became so popular in the brain MRI research community, a similar parameter for DSI and QBI reconstructions was needed. In analogy to fractional anisotropy, the generalized fractional anisotropy (GFA) is defined as:

$$\mathrm{GFA} = \sqrt{\frac{n \sum_{i=1}^{n} (\Psi(u_i) - \langle\Psi\rangle)^2}{(n-1) \sum_{i=1}^{n} \Psi(u_i)^2}} \tag{5.7}$$

where $\langle\Psi\rangle$ is the mean of the ODF [18].

QUANTITATIVE ANISOTROPY: In contrast to voxel-wise metrics such as FA and GFA, quantitative anisotropy (QA) is a metric for each resolved fiber orientation and quantifies the spin population along a given direction $\vec{a}$ [81].

$$\mathrm{QA}(\vec{a}) = Z_0(\Psi(\vec{a}) - I(\Psi_Q)) \tag{5.8}$$

where Z_0 is a scaling constant and $I(\Psi_Q)$ is the isotropic compartment of the ODF. The minimum value of the ODF is often used to estimate the isotropic compartment and is subtracted from the raw signal data.

5.4 FIBER-TRACKING

Given a field of ODFs, fiber-tracking algorithms try to find the most likely connections between voxels to form continuous fiber pathways. Various algorithms differ in how they integrate pathways and in the definition of their start/stop criteria. The most basic tractography algorithms follow the direction of the major eigenvector in discrete steps, assuming that it is tangent to the underlying fiber bundle.

Deterministic fiber-tracking algorithms usually start from a predefined seed point and find pathways by step-wise tracking of the major eigenvalue vector field (cf. Fig. 5.5). Depending on the algorithm, this field is interpolated to find smoother, more realistic transitions between neighboring voxels [7].

The main limitation of deterministic fiber-tracking algorithms is their lack of information about uncertainties of the reconstructed pathways. Artifacts or noise in DWI images can lead to errors in the estimation of the dominant fiber orientation of

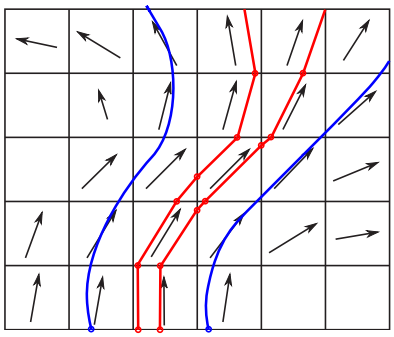

Figure 5.5: Illustration of step-wise (red) and interpolating (blue) fiber tracking algorithms. Note that although both red tracts start in the same voxel, their end points do not. In this case, the divergence of the vector field is correctly adapted.

a given voxel. It is therefore imperative to find a way to evaluate the confidence that one can have in the reconstructed pathways. This is the motivation of probabilistic fiber-tracking.

The free software tool DSI Studio was used for all tractography reconstructions presented in this thesis (http://dsi-studio.labsolver.org). DSI Studio performs deterministic fiber-tracking but evaluates the likelihood of tract propagation using the QA value in that direction [80]. In order to visualize 3D fiber architectures on 2D media such as computer screens and paper prints, fibers are color-coded to show their orientation. For in vivo applications of DWI, the colors red, blue and green align with R>L, H>F and A>P directions, respectively (R=Right, L=Left, H=Head, F=Feet, A=Anterior, P=Posterior). However, this is not true for the images shown in this thesis as the optimal image orientation in ex vivo imaging doesn't necessary align with this convention.

Part II

DIFFUSIVITY OF METAL-DOTA CHELATES

6

METHODS

The use of contrast agents in Magnetic Resonance Imaging has long since become a routine procedure in clinical diagnostics, especially for perfusion measurements and angiography. Contrast agent enhanced MRI also offers the great opportunity to investigate and possibly understand the mechanisms of how blood perfusion is influenced by factors such as arterial geometry or disease [62].

Whenever quantitative modeling of the contrast agent bolus is required, the diffusion coefficient of the applied contrast agent in human blood will be an important parameter. It was recently shown that the diffusion coefficient of the contrast agent in blood has a strong impact on the dispersion profile [58]. Although contrast agents are widely used in MRI, information about this fundamental property is surprisingly scarce. So far, only an indirect estimate of the Gd-DOTA diffusivity based on pharmacokinetic modeling of the MRI signal intensities in necrotic tumor regions has been reported [44].

As described in section 4.3, most MRI contrast agents rely on paramagnetic particles or ions to manipulate the relaxation properties of protons in their vicinity. Unfortunately, the strong paramagnetic moment of these particles or ions also affects atoms in the contrast agent complex itself. As a consequence, NMR signals from MRI contrast agent chelates are often either very broad or can't be detected at all.

According to the Stokes-Einstein equation, the diffusion coefficient of particles in a solution with viscosity η at temperature T only depends on their hydrodynamic radius r_h [22]:

$$D = \frac{k_B T}{6\pi\eta r_h} \tag{6.1}$$

It can therefore be hypothesized that the paramagnetic Gd^{3+} ion of Gd-DOTA can be replaced by another ion with lesser magnetic moment without changing the diffusional behavior of the complex. The new complex could then be detected by means of NMR spectroscopy and direct diffusion measurements of the complex would become feasible. The assumption of similar diffusional behavior will hold true as long as the hydrodynamic radius, which is mainly given by the DOTA structure, is not, or only to a negligible degree, changed by the substitution of the metal ion.

Based on this assumption, the following requirements for an ideal replacement ion for Gd^{3+} in Gd-DOTA were established:
The metal ion should

- be **trivalent** to maintain the coordination and structure of Gd^{3+}−DOTA and thus, the hydrodynamic radius r_h.
- have a little or no **magnetic moment** to achieve sufficiently long relaxation times for NMR detection and diffusion measurements of the complex.
- carry **spin 1/2** to allow direct detection of the metal ion itself in solutions where the proton background signal is strong (e.g. in human blood). For higher spin quantum numbers, quadrupolar interaction of the spin with electric field gradients within the highly polar DOTA molecule lead to rapid relaxation of the NMR signal [47].

Table 6.1 shows the part of the periodic table of elements where metal ions are found (groups 3-14 plus lanthanides). Elements are color-coded based on the above criteria to show their suitability as a replacement for Gd^{3+}. Surprisingly, there is no element that can fulfill all of the above conditions. Therefore, some of the requirements had to be relaxed for different experiments. For example, proton NMR spectroscopy in D_2O can still be performed if the metal ion has a spin different from 1/2 as long as it is not ferro- or paramagnetic.

3	4	5	6	7	8	9	10	11	12	13	14	group
Sc	Ti	V	Cr	Mn	Fe	Co	Ni	Cu	Zn	Ga		
Y	Zr	Nb	Mo	Tc	Ru	Rh	Pd	Ag	Cd	In		
Lan.*	Hf	Ta	W	Re	Os	Ir	Pt	Au	Hg	Tl	Pb	
*La	Ce	Pr	Nd	Pm	Sm	Eu	Gd	Tb	Dy	Ho	Er	Tm	Yb

Table 6.1: Part of the periodic table of elements where metal ions are found. Elements with spin 1/2 isotopes are highlighted and color-coded due to their suitability as substitution ions for Gd^{3+}. Bivalent and monovalent spin 1/2 elements are highlighted in orange. Ferro- and paramagnetic spin 1/2 metals are highlighted in red. There is no trivalent, non-magnetic spin 1/2 metal ion.

6.1 SYNTHESIS

According to the literature, DOTA is a very potent chelator for trivalent and some bivalent metal ions [33, 75]. This allowed for a wide range of elements to be tested for their suitability as replacements for Gd^{3+}. Table 6.2 gives a list of ions that were considered for the synthesis of a hydrodynamic analogue of Gd-DOTA along with some key properties.

ion	ionic radius	magnetic susceptibility χ_m	spin	compound
V^{3+}	64 pm	3.8×10^{-4}	^{51}Va: 7/2	VCl_3
Zn^{2+}	74 pm	-1.6×10^{-5}	^{67}Zn: 5/2	$ZnCl_2$
Ga^{3+}	62 pm	-2.3×10^{-5}	^{69}Ga: 3/2	$GaCl_3$
Y^{3+}	90 pm	1.2×10^{-4}	^{89}Y: 1/2	YCl_3
In^{3+}	80 pm	-5.1×10^{-5}	^{115}In: 9/2	$InCl_3$
La^{3+}	103 pm	5.4×10^{-5}	^{139}La: 7/2	$LaCl_3$
Eu^{3+}	95 pm	1.3×10^{-2}	^{151}Eu: 5/2	$EuCl_3$
Au^{3+}	85 pm	-3.5×10^{-5}	^{197}Au: 3/2	$AuCl_3$
Tl^{3+}	89 pm	-3.7×10^{-5}	^{205}Tl: 1/2	$TlCl_3$
Pb^{2+}	120 pm	-1.6×10^{-5}	^{207}Pb: 1/2	$PbCl_2$
Gd^{3+}	94 pm	1.2×10^{-1}	^{157}Gd: 3/2	

Table 6.2: List of ions that were considered as possible substitution ions for Gd^{3+} in Gd-DOTA. Ionic radii are taken from [61] for VI-coordinate ions for better comparison. Magnetic susceptibilities are taken from [77].

All metal-DOTA complexes were synthesized based on procedures previously described in the literature [3, 74, 20]. Pure DOTA was dissolved in D_2O to yield a clear solution. In this case, D_2O is preferred over H_2O because it avoids a high intensity water peak which could possibly absorb small signals in the spectrum. Contact with ambient humidity or residual water in other chemicals leads to the formation of HDO which is used as an internal reference. Additionally, the resonance of D_2O allows independent monitoring of magnetic field drifts during signal acquisition. Compounds containing the metal ions were also dissolved in D_2O (cf. Tab. 6.2). Concentrations of DOTA and the metal-chlorides varied over the course of this thesis to optimize the reaction conditions but were usually approximately $10\,mg\,mL^{-1}$. The two solutions were then mixed in molar ratios of 1:2, respectively, to provide an excess amount of metal ions in the solution. To prevent the formation of metal-hydroxides, pH was adjusted to 4 with NaOH. The total volume of the solution at this stage was usually about 15 mL. Samples were then heated to 80 °C and stirred overnight to increase the product yield. For the NMR spectroscopy experiments, 0.6 ml of the solutions were transferred into a 5 mm NMR tube. Chemicals were purchased from Sigma Aldrich (St. Louis, MO, USA) and used without further purification.

6.2 ^{1}H NMR SPECTROSCOPY

Successful complexation of the metal ions was verified by means of ^{1}H NMR spectroscopy. ^{1}H NMR spectra of all solutions were recorded on a Bruker Avance III 500 MHz NMR spectrometer (Bruker Corporation, Billerica, MA, USA) using an FID pulse sequence. Postprocessing of the spectra was performed by the software package TopSpin 3.0. The ppm scales of all ^{1}H spectra are referenced to HDO at 4.8 ppm to avoid the TMS (Tetramethylsilane) reference signal in the expected ppm range of DOTA.

For Ga-DOTA, additional spectra were recorded at temperatures between 310 K and 383 K to investigate structural changes and the integrity of the complex. Another spectrum at 310 K was acquired after the sample had cooled down to verify that the complex had not been destroyed at high temperatures. Probe temperatures were calibrated with a standard ^{1}H methanol sample and controlled using a variable temperature unit (BCU05, accuracy ± 0.1 K).

Human blood plasma samples were kindly provided by the blood transfusion laboratory of the Johannes Gutenberg University Medical Center. Each sample contained 4.5 mL of human blood plasma from centrifuged blood donations. Coagulation had to be prevented by adding citrate to the samples.

6.3 ^{1}H 2D DIFFUSION ORDERED NMR SPECTROSCOPY

The diffusion coefficients of successfully synthesized metal-DOTA complexes were measured using a standard Bruker 2D convection-compensated diffusion ordered spectroscopy (DOSY) pulse sequence as described in [35]. Diffusion gradient amplitudes were varied linearly from 10 to 470 mT m^{-1} over a total of 32 experiments. The diffusion time and gradient duration were kept constant at 36 ms and 2.8 ms, respectively, to avoid additional relaxation weighting. Diffusion coefficients were then calculated by fitting an exponential decay function to every data point of the 32 spectra:

$$S = S_0 \cdot \exp(-b \cdot D) \tag{6.2}$$

Data processing and analysis was performed by the software package TopSpin 3.0. For the calculation of b, TopSpin assumes rectangular gradient waveforms which can not be realized in real experiments (cf. Eq. 3.17). The error introduced by this assumption is internally corrected by adjusting the effective gradient amplitude duration product (area of the gradient) and will not be considered any further.

6.4 DIELECTRIC RELAXATION SPECTROSCOPY

In order to validate the assumption of similar diffusional properties of Gd-DOTA and Ga-DOTA, their hydrodynamic radii had to be measured and compared.

One approach to study hydrodynamic properties of polar substances in solutions is dielectric relaxation spectroscopy (DRS) [14]. DRS measures the polarization of a sample as response to an oscillating external electric field as a function of the field cycling frequency ν. The sample polarization is commonly expressed in terms of the complex permittivity spectra

$$\epsilon(\nu) = \epsilon'(\nu) - i\epsilon''(\nu) - \frac{i\kappa}{2\pi\epsilon_0\nu} \tag{6.3}$$

with ϵ' being the in-phase polarization components, ϵ'' the dielectric losses representing out-of-phase (absorptive) components, κ the direct current conductivity and ϵ_0 the permittivity of free space. Peaks in the resulting dielectric permittivity spectra allow calculation of the characteristic dielectric relaxation times which are determined by the mean rotational radius of the observed compound. As a result, rotation times of different compounds can be directly compared to assess their hydrodynamic similarity.

Dielectric permittivity spectra of solutions of Ga-DOTA and Gd-DOTA at equal concentrations were recorded on a frequency domain reflectometer based on the Anritsu Vector Star MS4647A vector network analyzer. For both solutions, frequencies between 400 MHz and 70 GHz were sampled at 25 °C. All spectra were calibrated using air, water and conductive silver paint as references. Measurements were performed and analyzed in cooperation with the Liquid Dynamics group at the Max Planck Institute for Polymer Research, Mainz.

7

RESULTS

7.1 ^{1}H NMR SPECTROSCOPY

Evaluation of the metal-DOTA ^{1}H NMR spectra was based on a comparison to the spectrum of pure DOTA which served as a reference. As can be seen from the structural formula of DOTA in Fig. 7.1, DOTA has a symmetric averaged planar cyclic structure in solution. The proton sites labeled as "1" or "2" represent chemically identical coordinations which lead to identical chemical shifts. Consequently, the NMR spectrum of DOTA shows two clear signals at 3.4 ppm and 3.8 ppm with an intensity ratio of 4:8, respectively, which matches the ratio of CH_2 groups at the sites "1" and "2". The protons at the end of the carboxyl groups are not visible in solution as they are constantly exchanged with the bulk water due to their acidity.

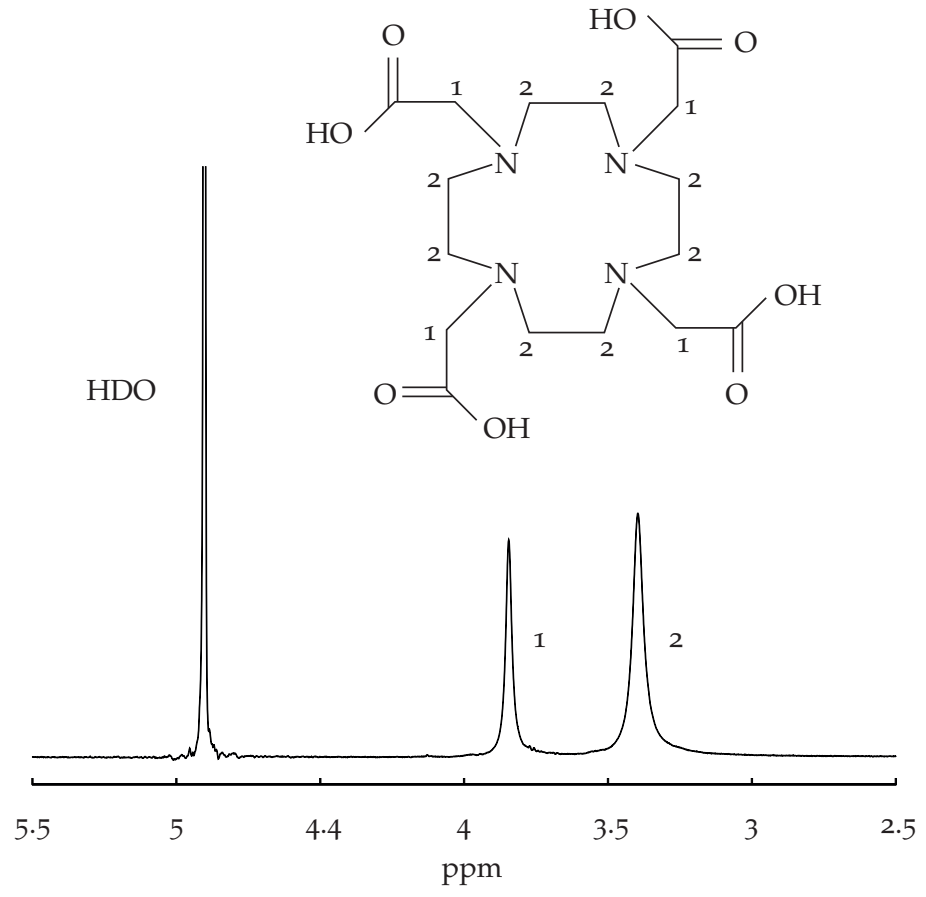

Figure 7.1: Structure and ^{1}H NMR spectrum of pure DOTA in D_2O. Proton sites labeled as "1" or "2" have the same chemical coordination and therefore experience the same chemical shifts. Thus, they contribute to the same peaks in the NMR spectrum. CH_2 groups at the labeled positions are omitted for the sake of clarity.

As shown in Tab. 6.2, a variety of metal ions were evaluated for their suitability as a replacement ion for Gd^{3+}. Figure 7.2 shows the ^1H NMR spectra of all solutions that were prepared in the course of this thesis.

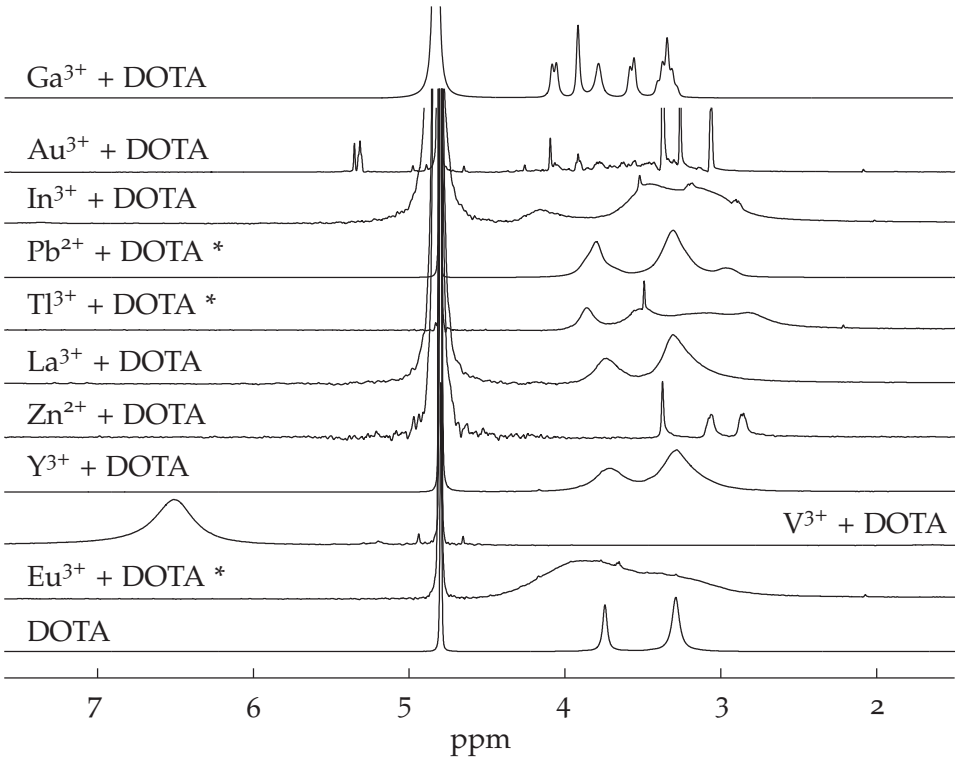

Figure 7.2: ^1H NMR spectra at 298 K of all metal + DOTA solutions and pure DOTA as a reference. All spectra are referenced to the signal of HDO at 4.8 ppm. (*) Data reproduced from the author's diploma thesis [79].

Unfortunately, most of the spectra either showed too many signals, signals that were very broad, or only the original DOTA signals which made identification of the metal-DOTA signals very difficult. For example, solutions of DOTA with La^{3+} and Y^{3+} showed broadened DOTA peaks but not any new signals that could be attributed to the respective metal-DOTA complexes.

An exception to this was the spectrum of a solution of $GaCl_3$ and DOTA which is shown separately in Fig. 7.3. A total of 5 signal groups were clearly visible in the ppm range of pure DOTA, with some of them split into multiplets. The appearance of multiple new peaks in the spectrum indicated that the DOTA structure had changed significantly after $GaCl_3$ had been added to the solution. This is a result of the Ga^{3+} ion being incorporated into the DOTA cavity. All individual signals show narrow peak widths which indicates long T_2 relaxation times. This is an important requirement for the diffusion measurements described later. Furthermore, the original DOTA peaks are no longer visible which indicated a complete reaction with high product yield.

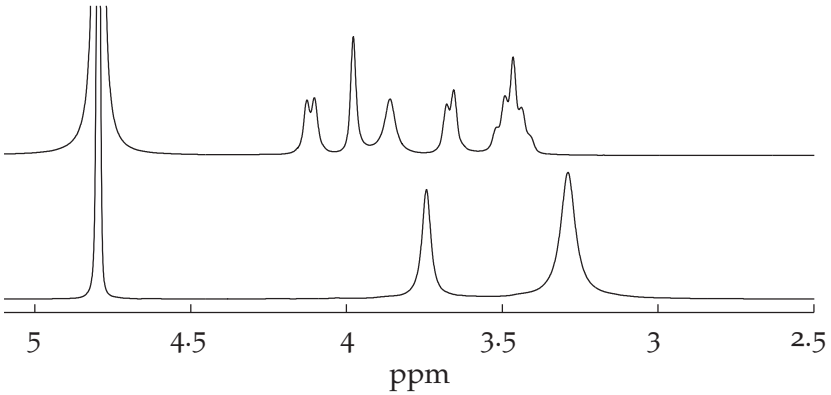

Figure 7.3: ^{1}H NMR spectra of Ga-DOTA and pure DOTA in D_2O. Several new peaks are observed after the Ga^{3+} ion was incorporated into the DOTA cavity.

7.1.1 *Thermal Stability of Ga-DOTA*

It was assumed that the observed signal splitting in Ga-DOTA was caused by a distortion of the formerly planar DOTA structure to form a cavity for the Ga^{3+} ion. This would result in a break of symmetry and thus cause different chemical shifts at different proton sites. To verify this assumption and explain the observed spectrum, additional spectra at different temperatures were recorded (cf. Fig. 7.4). Each FID was averaged 16 times for a total acquisition time of 2 minutes and 11 seconds. This measurement was repeated 9 times for temperatures between 310 K and 383 K.

With rising temperatures, a transition of the Ga-DOTA spectrum to a two signal spectrum was observed. This can be explained by the additional energy in the system at high temperatures which leads to a less rigid molecular structure. Rapid oscillations of the cyclic DOTA complex result in an "averaging" of the local magnetic fields and reverse the signal splitting. After cooling the sample down from 383 K, a second spectrum at 310 K was recorded to show that the observed spectral changes were not due to the destruction of the Ga-DOTA complex.

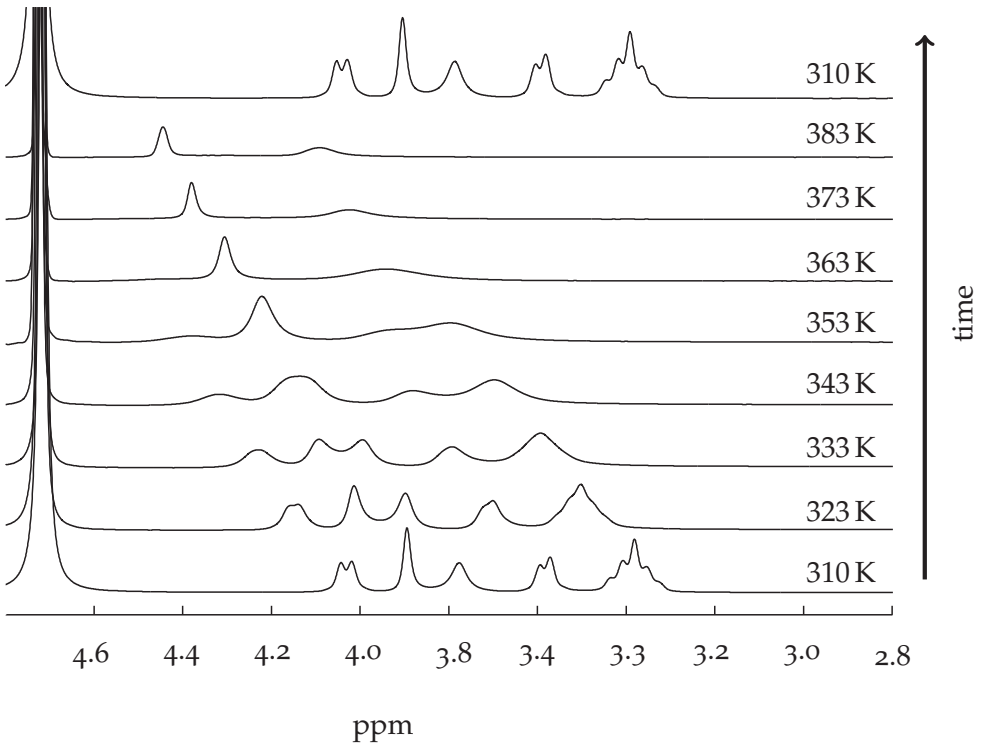

Figure 7.4: ^1H NMR spectra of Ga-DOTA in D_2O at different temperatures. The higher thermal energy leads to rapid oscillations of the complex which partially reverses the observed signal splitting. The top spectrum was recorded after the sample had cooled down to verify that the complex had not been destroyed during the high temperature experiments.

7.1.2 *Mass Spectrometry of Ga-DOTA*

Additional proof of the successful Ga-DOTA synthesis was given by MALDI-TOF (matrix-assisted laser desorption/ionization time of flight) mass spectrometry [37, 69]. Figure 7.5 shows the resulting mass spectrum of Ga-DOTA with peaks at mass-to-charge ratios of 471 and 473. Multiple peaks were expected because of the natural abundances of ^{69}Ga (60.1 %) and ^{71}Ga (39.9 %) and agree with reported values in the literature [74]. The two additional peaks with lesser intensity are caused by the natural abundances of ^{12}C (98.9 %) and ^{13}C (1.1 %). Note that, in general, peak intensities in mass spectroscopy do not represent actual quantities in the sample.

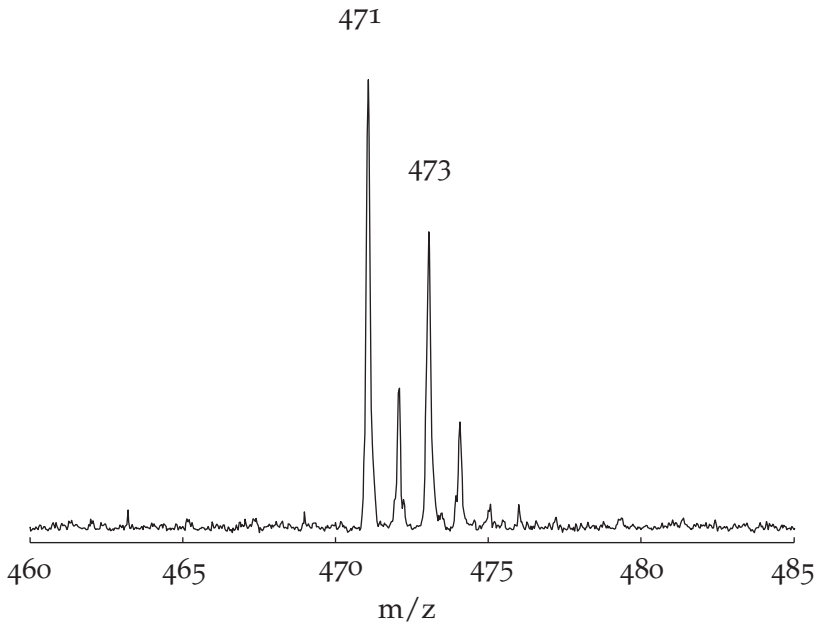

Figure 7.5: MALDI-TOF mass spectrum of Ga-DOTA.

7.2 ^{1}H 2D DIFFUSION ORDERED NMR SPECTROSCOPY

Figure 7.6 shows the results of 2D DOSY NMR experiments on solutions of Ga-DOTA and pure DOTA in D_2O at 310 K, processed by TopSpin 3.0. Diffusion coefficients were calculated for each data point of the spectra which are shown above the diffusion plots. The dashed lines indicate the mean diffusion coefficients of the respective signals. Additionally, the diffusion coefficient of HDO as the visible component of the solvent D_2O is shown. It is important to note that for both solutions, DOTA and Ga-DOTA, all signals show similar diffusion coefficients. This confirms that all observed signals originate from the same molecule. One can also conclude that none of the peaks in the Ga-DOTA spectrum are caused by residual DOTA, which indicates a complete reaction with no DOTA left in the solution.

In order to evaluate the error of the diffusion coefficient, which is not accessible in TopSpin 3.0, fitting of Eq. 3.14 was performed manually in GnuPlot (http://gnuplot.info) using the integrated peak areas instead of individual data points. The final diffusion coefficients of Ga-DOTA and pure DOTA in D_2O at 310 K were then calculated as the mean value of the individual peak diffusivities:

$$D_{\mathrm{Ga-DOTA}}(310\,\mathrm{K}, D_2O) = (4.38 \pm 0.04) \times 10^{-10}\,\mathrm{m^2/s} \tag{7.1}$$

$$D_{\mathrm{DOTA}}(310\,\mathrm{K}, D_2O) = (5.68 \pm 0.04) \times 10^{-10}\,\mathrm{m^2/s} \tag{7.2}$$

$$D_{\mathrm{HDO}}(310\,\mathrm{K}, D_2O) = (2.29 \pm 0.04) \times 10^{-9}\,\mathrm{m^2/s} \tag{7.3}$$

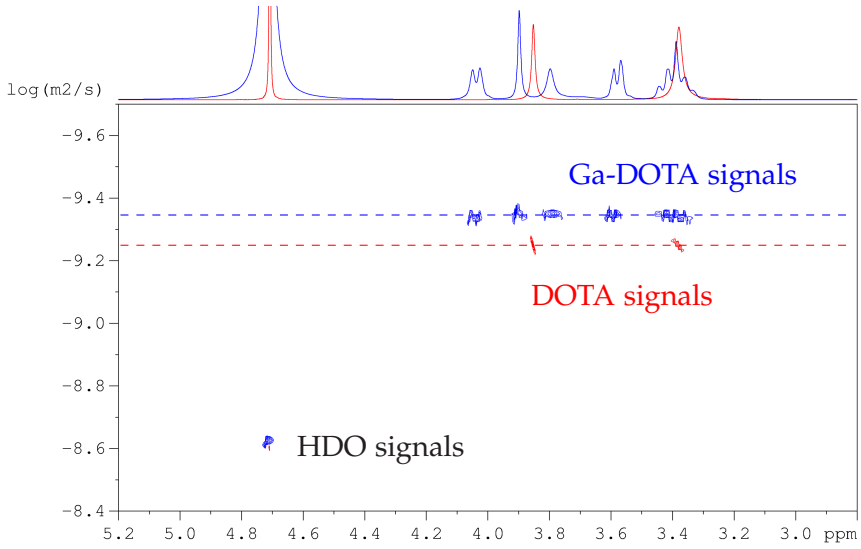

Figure 7.6: ^{1}H 2D DOSY NMR spectra of pure DOTA and Ga-DOTA at 310 K. Values below a confidence threshold are omitted for the sake of clarity.

Figure 7.7 shows the results of dielectric relaxation spectroscopy (DRS) performed on solutions of Ga-DOTA and Gd-DOTA in D_2O. Both solutions show an intense water relaxation peak at 20 GHz (red curve). Due to the non-centrosymmetric (i.e. dipolar) nature of both metal-DOTA complexes, an additional relaxation mode towards lower frequencies is expected. As can be seen from Fig. 7.7, the superposition of two Debye modes excellently describes the experimental data (gray shaded areas). The dielectric relaxation times of both solutes were found to be very similar:

$$\tau_{\text{Ga-DOTA}} = (210 \pm 10)\,\text{ps} \tag{7.4}$$

$$\tau_{\text{Gd-DOTA}} = (211 \pm 5)\,\text{ps} \tag{7.5}$$

Confidence intervals correspond to the standard deviation within 12 independent measurements. Due to the asymmetric coordination of the central metal ion by DOTA in both metal-DOTA complexes, the measured relaxation modes evidently originate from diffusive rotation of the solutes. The relaxation time is determined by the hydrodynamic radius of the solute (i.e. the larger the hydrodynamic radius the slower the relaxation time). The similarity of the extracted values for $\tau_{\text{Ga-DOTA}}$ and $\tau_{\text{Gd-DOTA}}$ provides evidence that the rotational hydrodynamic radius is not significantly altered upon substituting Ga^{3+} for Gd^{3+}.

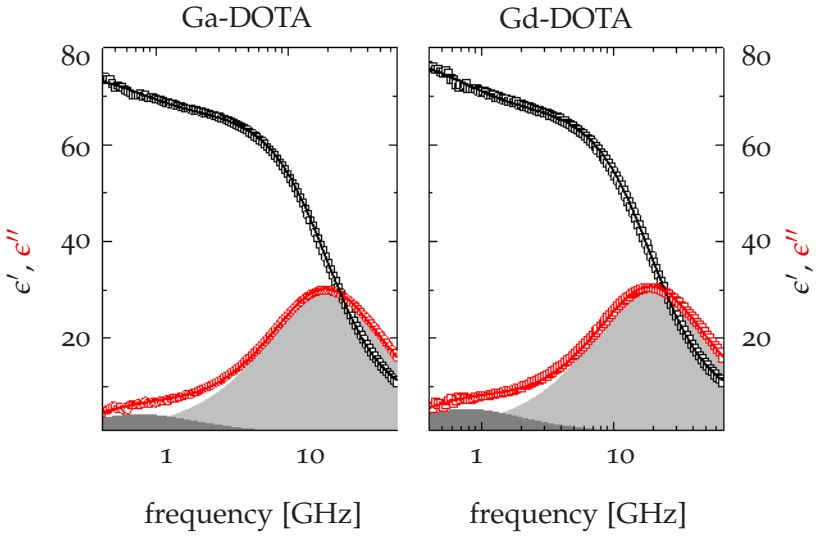

Figure 7.7: Dielectric relaxation spectra of Ga-DOTA and Gd-DOTA in D_2O. The dark gray shaded areas depict the contributions of the respective metal-DOTA complex and show very similar peak frequencies.

8

DISCUSSION

The presented results show that of all potential metal ions listed in Tab. 6.2, only Ga^{3+} was successfully incorporated into the DOTA cavity. Other metal ions showed either very broad or too many lines to allow reliable assignment of these signals to a metal-DOTA complex. The formation of Ga-DOTA was confirmed by MALDI-TOF mass spectrometry and ^{1}H NMR spectroscopy. The diffusion coefficient of Ga-DOTA in D_2O at body temperature was determined with high accuracy to be:

$$D_{\mathrm{Ga-DOTA}}(310\,\mathrm{K}, D_2O) = (4.38 \pm 0.04) \times 10^{-10}\,\mathrm{m^2/s} \tag{8.1}$$

The diffusion coefficient of HDO was calculated to be:

$$D_{\mathrm{HDO}}(310\,\mathrm{K}, D_2O) = (2.29 \pm 0.04) \times 10^{-9}\,\mathrm{m^2/s} \tag{8.2}$$

This value is slightly slower than a previously reported value for HDO diffusion in D_2O of $2.59 \times 10^{-9}\,\mathrm{m^2/s}$ [52] [1]. This may indicate that Ga-DOTA slightly increases the viscosity of the solution. Also, because of the low molecular mass of HDO, its diffusional behavior is very sensitive to other particles in the solution so that the presented result may not be directly comparable to the literature [52, 53].

The assumption of similar diffusional behavior of Gd-DOTA and Ga-DOTA has to be evaluated based on the presented results:

It may appear counter-intuitive that although the kinetic energy of a particle depends on its mass, the resulting diffusion coefficient does not. Computer simulations show that mass only affects diffusion in very small systems where the mass of the diffusing particle is comparable to that of the solvent molecules [53]. For large systems, a thermodynamic limit is reached where D becomes independent of the particle mass.

Comparing the crystal structures of both complexes, one has to point out that although both ions are trivalent, the coordination within the complex is quite different (cf. Fig. 8.1). While Gd^{3+} is nine-coordinate in Gd-DOTA, Ga^{3+} is only six-coordinate with two free carboxyl groups. However, different coordination of the metal ions does not necessarily falsify the assumption of similar diffusional behavior. The key parameter for this assumption is the hydrodynamic radius of the complex. Unfortunately, the hydrodynamic radius is extremely difficult to measure.

1 Value interpolated from data given in [52] using linear regression.

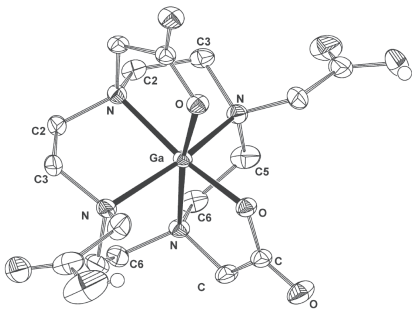

(a) Solid-state crystal structure of Ga-DOTA as determined by X-ray crystallography. Image reproduced from [45].

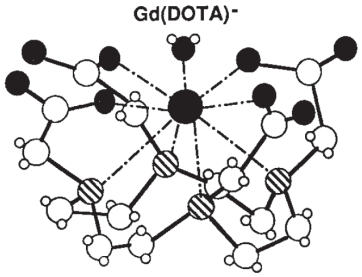

(b) Structure of Gd-DOTA. Image reproduced from [9].

Figure 8.1: Comparison of crystal structures of Ga-DOTA and Gd-DOTA. Although both metal ions are trivalent, their coordination within the DOTA complex is different.

For larger molecules and polymers, dynamic light scattering (DLS) is often used to analyze solution state dynamics. However, the scattering power is proportional to the 6th power of the particle radius which limits the resolution of this method to the nanometer scale. In the case of DOTAREM ©, the solution also contains meglumine which serves as a buffer. Judging from its crystal structure, meglumine can be expected to have a hydrodynamic radius which is very close to that of Gd-DOTA. This creates the need for an additional method to distinguish between these two species.

For Ga-DOTA, the measured diffusion coefficient can be used to calculate r_h using the Stokes-Einstein equation:

$$r_h = \frac{k_b T}{6\pi\eta D} \tag{8.3}$$

This yields a hydrodynamic radius of Ga-DOTA of:

$$r_h = 6.48\,\text{Å} \tag{8.4}$$

with $\eta = 0.8\,\text{mPa s}$ at $310\,\text{K}$ [17].

For Gd-DOTA, no reported values for r_h were found in the literature.

DRS measurements of Ga-DOTA and Gd-DOTA in D_2O showed very similar rotation peaks in their respective spectra which agree well within their confidence intervals.

$$\tau_{\text{Ga-DOTA}} = (210 \pm 10)\,\text{ps} \tag{8.5}$$

$$\tau_{\text{Gd-DOTA}} = (211 \pm 5)\,\text{ps} \tag{8.6}$$

As the relaxation times are determined by the hydrodynamic radius of the complexes, the similarity of their rotational relaxation times provides evidence that the hydrodynamic radius is not significantly changed upon substitution of Gd^{3+} with Ga^{3+}. Therefore, the diffusion coefficient and hydrodynamic radius of Ga-DOTA given in Eqs. 8.2 and 8.4, respectively, are also valid for the MRI contrast agent Gd-DOTA.

For most clinical research applications, the relevant information is the diffusion coefficient of the applied contrast agent in human blood. Direct measurements of the Ga-DOTA diffusion coefficient in human blood are difficult because of the intense ^{1}H NMR signal background. Fig. 8.2 shows an exemplary ^{1}H spectrum of a blood plasma sample. Unfortunately, even the addition of large Ga-DOTA quantities ($\approx 20\,\text{mg}$) did not produce significant changes in the blood plasma spectrum. One has to note that the addition of citrate to prevent coagulation adds multiple strong peaks in the expected ppm range of Ga-DOTA [6]. The exact positions of the Ga-DOTA signals are hard to predict because they are influenced by factors such as pH and other molecules in the solution. Future studies may benefit from using alternative anti-coagulation methods or agents.

The main difference between D_2O and blood as a solvent is their viscosity. Using the Stokes-Einstein equation (6.1), the measured diffusion coefficient in D_2O can be corrected for the viscosity to estimate the diffusivity in human blood plasma

$$D_{\text{plasma}} = \frac{\eta_{D_2O}}{\eta_{\text{plasma}}} \cdot D_{D_2O} \tag{8.7}$$

This yields a diffusion coefficient for both complexes in human blood plasma at 310 K of

$$D_{\text{Ga/Gd-DOTA}}(310\,\text{K}, \text{plasma}) = (2.92 \pm 0.25) \times 10^{-10}\,\text{m}^2/\text{s} \tag{8.8}$$

where $\eta_{\text{plasma}} = 1.2\,\text{mPa s}$ and $\eta_{D_2O} = 0.8\,\text{mPa s}$ [41, 17].

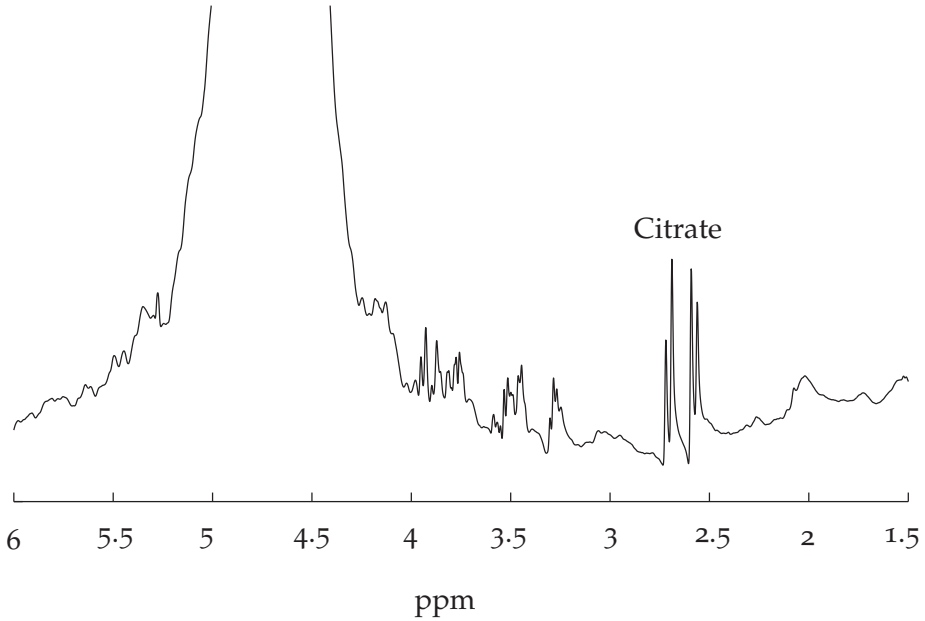

Figure 8.2: ^{1}H NMR spectrum of human blood plasma with two sharp citrate signals.

The estimated diffusivity in blood plasma agrees with a previously reported value of the Gd-DOTA diffusion coefficient in necrotic tumor regions of $D = (2.08 \pm 0.88) \times 10^{-10}\,\mathrm{m^2/s}$ [44]. However, the agreement is mainly due to the high uncertainty of the literature value of 42% and should be evaluated with caution.

Due to similar hydrodynamic properties of Ga-DOTA and Gd-DOTA, this value of the diffusion coefficient in blood plasma at 310 K is also valid for the MRI contrast agent Gd-DOTA. It may serve as a reliable reference for future studies, not only in the field of MRI. With increasing interest in ^{68}Ga-DOTA and its derivatives as a tracer in positron emission tomography (PET), the presented diffusivity of Ga-DOTA may also play an important role in the analysis of dose distributions from a given tracer bolus.

Part III

HIGH-RESOLUTION EX VIVO DIFFUSION-WEIGHTED IMAGING - THE PANINI PROJECT

9

METHODS

The methods described in this chapter can be divided into two projects. Work on the topic of diffusion tractography started during a 6-month research stay at the Athinoula A. Martinos Center of the Massachusetts General Hospital (MGH), Boston, MA, USA. Within the framework of the *NIH Blueprint Human Connectome Project*, the group of Lawrence L. Wald had started the development of an experimental setup for high-resolution MR imaging of post mortem human brain tissue specimens. As will be described later, this project quickly became known as "The Panini Project".

After 6 months in Boston, work on this topic continued in Mainz with a slightly shifted focus. The aim of this second project was to analyze the impact of tissue fixation on the results of fiber reconstructions. This was done using Formalin-fixed and unfixed pig models. As a second step, the feasibility of high-resolution DWI of unfixed human brain and heart tissue on a commercially available MRI system was demonstrated.

9.1 DWI OF FIXED HUMAN BRAIN SPECIMENS

Tractography based on diffusion-weighted MR images is one the most powerful non-invasive techniques to study and understand the complex architecture and connectivity of neuron pathways in the human brain. The Human Connectome Project (HCP) is a large-scale project currently focusing on this research topic. Within its framework great advances in MRI hardware and methodology have been achieved. A key achievement was the development of the 3 T Siemens Magnetom Connectom MRI tomograph whose gradient system was re-built from scratch to allow for a maximum gradient amplitude of $300\,\mathrm{mT\,m^{-1}}$ that can be switched at a slew rate of $200\,\mathrm{mT\,m^{-1}\,ms^{-1}}$ [60].

With the development of more advanced diffusion sampling schemes and fiber-tracking algorithms, smaller and more complex fiber structures became observable on the Human Connectom MRI system [49, 34]. However, the required acquisition times of several hours soon posed a limit on the achievable spatial resolution in living subjects or patients.

Ex vivo DWI enables virtually "unlimited" examination times while being intrinsically free of motion. Spatial resolution and the number of sampled diffusion directions can be significantly increased to investigate even smaller fiber architectures. It was shown by Sun et al. that relative indices such as fractional anisotropy and reconstructed fiber orientations are preserved in fixed tissue [68]. Therefore, DWI of fixed ex vivo tissue specimens provides a valuable tool to obtain high-resolution data that is not accessible from living subjects.

The aim of the Panini project, as part of the Human Connectome Project, was to explore the limits of spatial and angular resolution of diffusion tractography of post mortem human brain specimens on the 3 T MGH-UCLA Human Connectom MRI system.

9.1.1 *Experimental Setup*

The Panini Coil

As SNR was expected to be the limiting factor for increasing spatial resolution below the millimeter scale, a special 60 channel coil array with optimized geometry for imaging of ex vivo tissue specimens was designed and constructed by Gruber et. al. [29]. The diameter of the individual coil elements of 40 mm was chosen to achieve sufficient penetration depth for tissue specimens of up to 5 cm thickness. At the same time, a high number of channels was desirable to enable parallel imaging with high acceleration factors. Based on the average diameter of a human brain, the active volume was set to about $220 \times 180 \times 50$ mm^3. In order to closely cover this volume, two coil layers of 30 elements each were mounted on a wooden base-plate and a movable lid. The coil housing was printed using a fast prototyping 3D printer (FORTUS 3D Production Systems by Stratasys, MN, USA). Figure 9.1 shows a rendered 3D simulation of the two coil layers around a whole human hemisphere. Photographs of the final setup are shown in figure 9.2. The implementation of a double-hinged lid allowed for a flexible setup that can be adjusted to the thickness of the imaged sample. The strong resemblance of the coil with commercial panini presses was name-giving for this study.

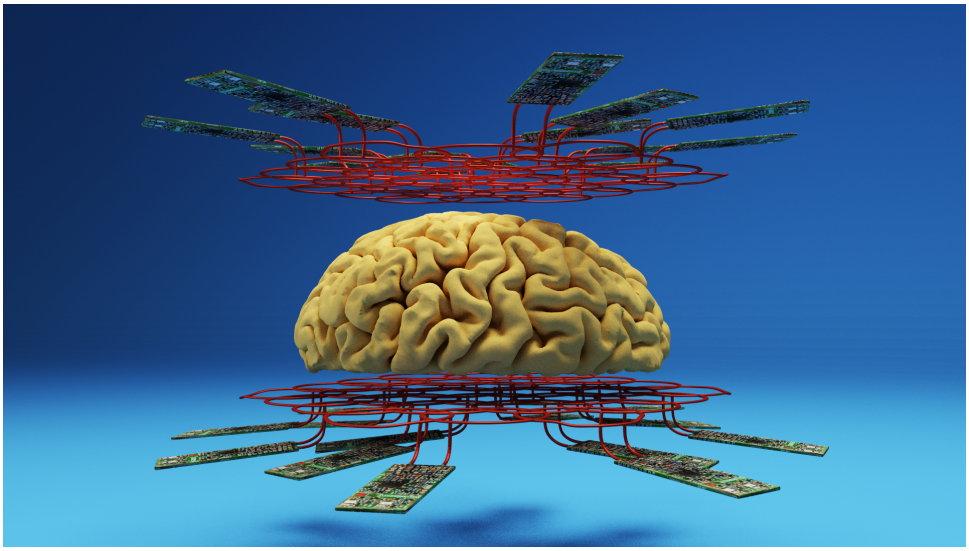

Figure 9.1: 3D render of the two 30 channel coil layers covering a whole human hemisphere. The 3D model was created using the free software Blender, version 2.6 (http://blender.org)

Upon arrival at the MGH, the coil showed intense image artifacts, so-called spikes, that can result from defective coil elements or short circuits. Extensive testing of the coil in the laboratory revealed several defective components and required partial re-development of the setup.

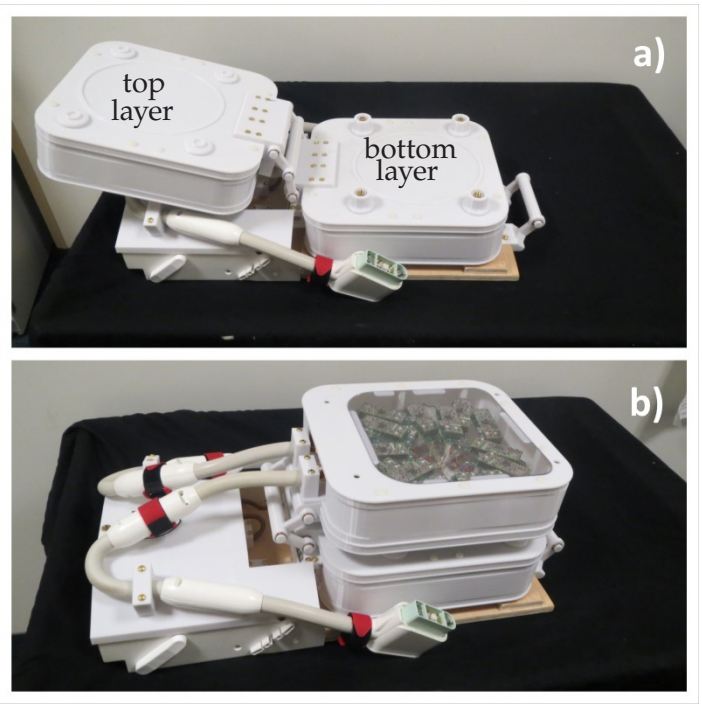

Figure 9.2: Photographs of the final coil setup in the (a) open and (b) closed state: The Panini coil consists of a base-plate and lid which contain planar arrays of 30 coil elements each.

In order to evaluate the performance of the Panini coil, SNR and $1/G$ maps were acquired and compared with a 64 channel head coil. The G-factor describes SNR losses in the final image when accelerated imaging techniques are used to sub-sample k-space (so-called "SNR penalties")[57].

$$\mathrm{SNR}_{\mathrm{accelerated}} = \frac{\mathrm{SNR}_{\mathrm{full}}}{G \cdot \sqrt{R}} \tag{9.1}$$

The acceleration factor R defines the portion of k-space lines that are sampled, e.g. for $R = 2$ only every 2^{nd} line in k-space is acquired. The sensitivity profiles of individual coil elements can be used to compensate aliasing artifacts which would normally result from undersampling of k-space (cf. Parallel Imaging). In MR coil engineering, maps of $1/G$ are often used to quantify SNR losses as a function of the acceleration factor. For parallel imaging, SNR losses of up to 20 % are usually rated as acceptable which translates to a $1/G$ factor of 0.83 [59].

Tissue Specimens

In order to evaluate the performance of the Panini coil for tissue specimens of different shapes and sizes, two fixed human brain tissue specimens were provided by the group of Bruce Fischl of the Athinoula A. Martinos Center. The two specimens were a whole human hemisphere as an example for the maximum sample volume of the setup and a smaller, coronal slab cut from the central brain region of another hemisphere (cf. Fig. 9.4). At the time of this study, the samples had been fixed in Formalin for several years. The use of human brain tissue for the experiments presented in this chapter was approved by the local ethics committee.

(a) Whole hemisphere (b) Coronal slab

Figure 9.3: Photographs of the two fixed human brain tissue specimens used in this chapter.

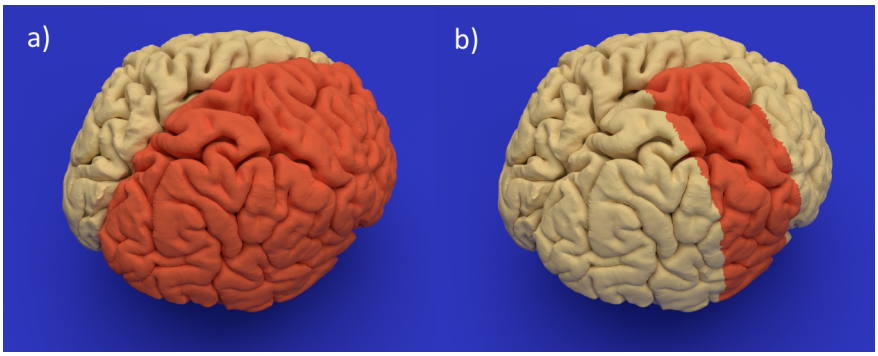

Figure 9.4: Anatomical localization of fixed human brain tissue specimens: a) whole human hemisphere and b) coronal slab cut from the central brain region.

Imaging Pulse Sequence

Mapping of T_1 and T_2 in the fixed tissue specimens revealed dramatically reduced relaxation times (cf. Fig. 10.4). This is a consequence of fixing the tissue with paraformaldehyde solutions (Formalin or Fomblin) as the fixative increases water viscosity and tissue rigidity [72].

Diffusion-weighted EPI pulse sequences have a minimum echo time which is mainly given by the duration of the diffusion gradients and readout echo train. For the 3D DW-EPI sequence shown in Fig. 9.5, the minimum echo time can be calculated as:

$$TE_{\text{min}} = \frac{T_{\text{InvPulse}}}{2} + T_{\text{DiffGrad}} + T_{\text{PE}} + \frac{T_{\text{RO}}}{2} \tag{9.2}$$

with T_{InvPulse} being the duration of the 180° inversion pulse, T_{DiffGrad} the diffusion gradient duration, T_{PE} the duration of the phase encoding preparation block, and T_{RO} the readout duration. All timing parameters include their respective ramp times and hardware delays. Equation 9.2 assumes that the second half of TE after the inversion pulse is the limiting factor for TE_{min} which is true for most EPI applications. Although non-accelerated Cartesian k-space sampling is implied here, Eq. 9.2 can be easily modified to account for parallel imaging and advanced k-space sampling techniques without changing the following general considerations.

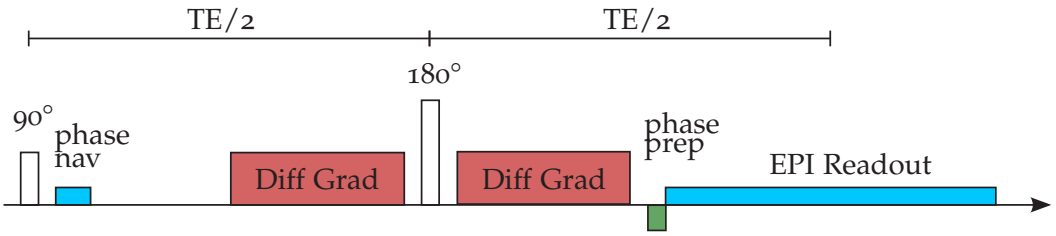

Figure 9.5: Schematic representation of the 3D diffusion-weighted EPI imaging pulse sequence used for the experiments in this chapter.

As can be seen from Eq. 9.2, for a given duration of the diffusion encoding gradient, the minimum echo time of DW-EPI sequences scales with the duration of the readout echo train T_{RO}. For high spatial resolutions, the number of phase encoding lines in k-space increases and leads to longer echo trains, i.e. longer minimum echo times. This can be problematic, especially when the T_2 relaxation time of the imaged tissue is short, e.g. in fixed tissue. The T_2 decay will then lead to T_2 blurring in k-space and dramatic losses in SNR.

With the need for high b-values in ex vivo DWI, the duration of the diffusion encoding gradients becomes another major source for SNR losses. While clinical routine applications of DWI use b-values in the range of 500 s/mm^2 to 1500 s/mm^2, a b-value of 30 000 s/mm^2 was needed to achieve strong diffusion weighting in the

fixed human brain [1]. Assuming that the maximum gradient amplitude is used, higher b-values can only be achieved by increasing the gradient duration or the diffusion time. Both options imply an increased TE_{min} and reduced SNR. At this point, the gradient system of the Siemens Magnetom Connectom provides a unique tool to drastically reduce the gradient durations for a desired b-value by using its $300\,\text{mT}\,\text{m}^{-1}$ gradients (cf. results in section 10.1.2).

As described in chapter 4.1.5, the readout duration can also be reduced by splitting k-space sampling into multiple "shots". For all experiments performed at the Martinos Center in Boston, a segmented multi-shot readout was used to increase SNR at the cost of total acquisition time.

In order to evaluate the results of the presented setup, an in vivo data set from the Human Connectome Project (HCP) was kindly provided by the group of Lawrence L. Wald at the Martinos Center. The following acquisition parameters were used for the results presented in chapter 10.1:

	whole hemisphere	coronal slab	HCP reference
sequence	3D DW-EPI	3D DW-EPI	2D DW-EPI
TE [ms]	100	79	57
TR [ms]	600	400	8,800
matrix [p/r/s]	262/380/112	322/430/128	140/140/96
resolution [µm]	$500 \times 500 \times 500$	$350 \times 350 \times 350$	$1500 \times 1500 \times 1500$
bandwidth/pixel [Hz]	598	485	1984
diffusion directions	266	120	64/128*
b-value [s/mm^2]	30 000	30 000	1000/5000*
acquisition time [h]	47 : 00	20 : 00	0 : 22

Table 9.1: Acquisition parameters for the experiments on fixed human brain specimens.
* The HCP protocol acquires different shells in q-space with different numbers of sampled diffusion directions. For a fair comparison with the single-shell data from the Panini project, only the $b = 5000\,\text{s/mm}^2$ shell with 128 directions was used to reconstruct fiber tracts.

1 Reference for clinical values: Prof. Dr. med. Müller-Forell, Director of the Institute of Neuroradiology, University Medical Center, Mainz.

Diffusion Sampling

Diffusion was sampled using custom-made gradient vector tables. The gradient vectors were generated randomly on an iso-sphere and distributed evenly using an electrostatic repulsion model. As will be described later in this chapter, the correction algorithm for eddy current induced distortions requires input distortion fields from images with opposing gradient polarities. Therefore, the opposite direction of every vector was also added to the gradient vector table. The diffusion directions were then sampled using the provided vectors in random order to suppress any bias, e.g. due to sample heating. For an easier alignment of MR images and sampled diffusion directions during post-processing the PRS (phase-read-slice) coordinate system was used for the gradient vector tables and image acquisition.

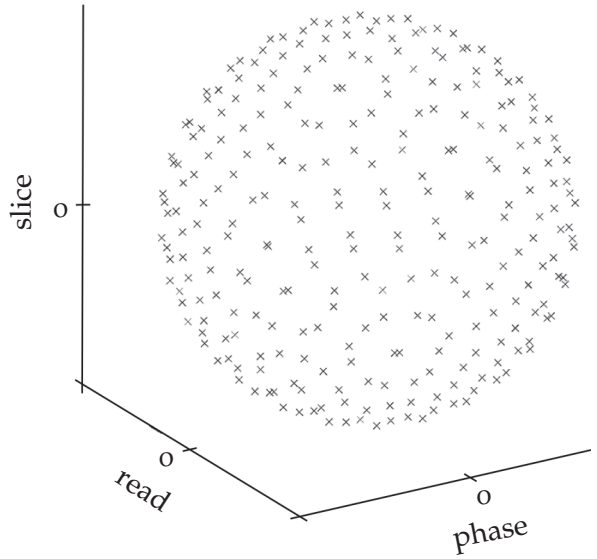

Figure 9.6: Q-space coverage with 266 normalized diffusion gradient vectors in the PRS coordinate system.

For high numbers of sampled diffusion directions, total acquisition times can become extremely long (up to days depending on the spatial resolution). In order to avoid damage to the gradient system by continuous operation on maximum duty cycle, those acquisitions were split into several parts with additional cooling pauses for the HF transmit and gradient system. Each set included a b_0 reference volume and 20 diffusion-weighted volumes.

9.1.2 *Postprocessing*

In order to use a given data set for diffusion-based tractography, a series of post-processing steps has to be performed after the raw data has been acquired. The pipeline used for all experiments in this chapter was developed as part of this thesis and is represented by a workflow diagram in Fig. 9.7.

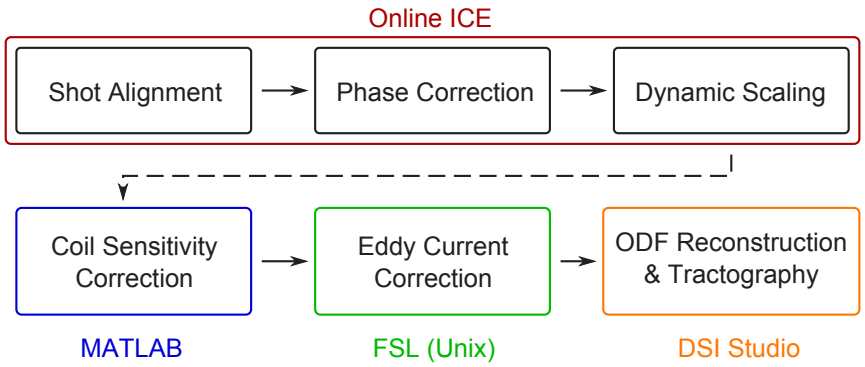

Figure 9.7: Postprocessing pipeline.

SHOT ALIGNMENT: As k-space was sampled using multiple shots (cf. Fig. 4.7c), these shots had to be merged to recover the full k-space information. Alignment of individual shots was based on phase-navigator data which was acquired with every shot. The navigator consisted of three gradient echoes which were generated immediately after the initial 90° pulse. The unwrapped phase evolutions of echoes 1 and 3 were averaged as they both represent "forward" lines in k-space and compared to echo 2 which represents a "reverse" line (cf. section 4.1.4). After all reversed lines were flipped, detected phase errors had to be corrected.

PHASE CORRECTION: As part of the k-space reconstruction, detected phase errors between shots were corrected using two different approaches. The standard Siemens implementation is based on auto- and cross-correlations of the navigator signals as described in [2]. As will be discussed in chapter 10.1.1 this phase correction method failed when used with data from the 3D multi-shot DW-EPI sequence and resulted in severe ghosting artifacts.

Therefore, a different approach by Feiweier was evaluated which introduces additional weights for the correlations based on the signal's magnitude [24]. This suppresses the impact of noise regions in the navigator signals and significantly decreased the previously observed ghosting level. These findings motivated the manual implementation of Feiweier's approach into the online ICE (Image Calculation Environment) reconstruction software.

DYNAMIC SCALING: During image reconstruction, all images of the same series, including the b_0 reference, are usually scaled to use the same dynamic image range of 4096 *integer* gray values. The highest signal intensity will always be found in the b_0 reference while the diffusion-encoded images will have significantly lower intensities. Therefore, diffusion encoding only uses part of the available gray value range which results in a loss of information in the final magnitude image. In order to preserve the full diffusion information, the ICE program was further modified to scale every image separately before converting the image to *integer* precision. The scaling factor was written to the image header and images were re-scaled at *double* precision during reconstruction of the diffusion orientation distribution functions.

Images were calculated using a modified Siemens ICE program. Based on a 2D EPI reconstruction, the additional Fourier transform for 3D encoding had to be implemented along with support for multi-shot acquisitions and dynamic scaling as described above. The reconstructed images were exported from the host computer in NIFTI format for further processing.

COIL SENSITIVITY CORRECTION: The sensitivity profile of the Panini coil shows a steep intensity gradient close to the surface of the coil (cf. Figs. 9.8 and 9.9a). This is mainly due to the small diameter of the coil elements and close proximity to the sample. While voxel-wise indices such as fractional anisotropy or relaxation times are not influenced by this constant offset, the coil sensitivity profile can cause instabilities for algorithms that isolate target volumes based on intensity thresholds. Therefore, a coil sensitivity correction in the direction perpendicular to the coil surfaces had to be applied for further processing (cf. Fig. 9.8). In the lateral direction no significant intensity variations were found.

Analysis of the sensitivity profile in a homogeneous water phantom showed good agreement with second order polynomials. However, due to variable distances of the two coil layers depending on the sample thickness, a fixed calibration based on a single water phantom will not be applicable to every sample. Therefore, a dynamic method based on the final images had to be developed. The sensitivity profile was estimated by averaging the signal from a range of 30 lines in the final image (cf. Fig 9.9) and modeled with a second order polynomial fit function.

Higher order polynomials may be more accurate in some cases but bear the risk of discarding anatomical features in the image. Although this approach may fail under certain conditions, it achieved satisfying results for all data sets presented in this thesis.

EDDY CURRENT CORRECTION: Eddy current distortions were corrected using the *eddy* function of the software package FSL [4]. Internally, *eddy* uses images with opposing diffusion gradient polarities to estimate the degree and direction of the distortion field. Images are then corrected by applying an inverse distortion and registration to the b_0 reference. For images with low SNR values, this procedure sometimes has to be repeated several times as anatomical features are less pronounced and the correction is less accurate.

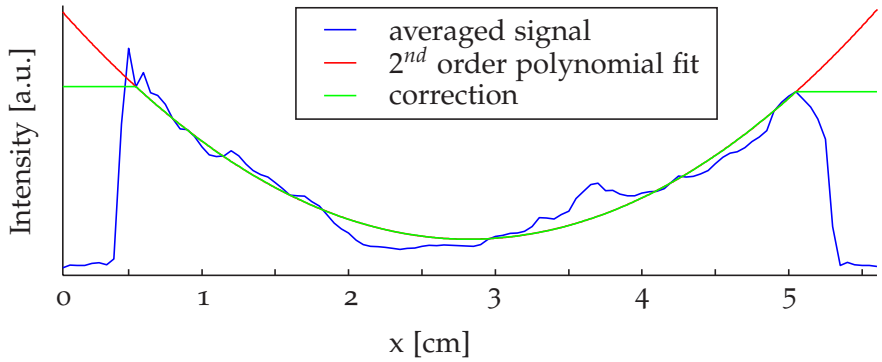

Figure 9.8: Coil sensitivity correction: The signal profile was calculated as the average signal in a region of interest (Fig. 9.9) and modeled with a second order polynomial fit function.

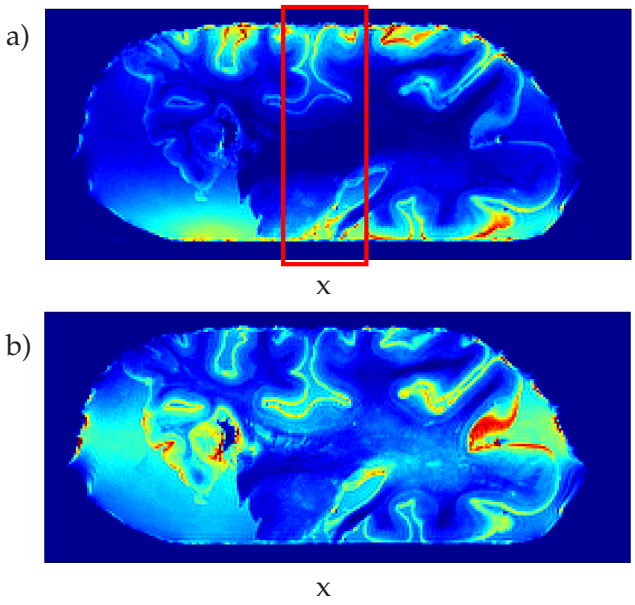

Figure 9.9: Coronal view of the hemisphere at 500 µm isotropic resolution: a) before and b) after correction of the coil sensitivity profile. The red rectangle indicates the region of interest where the signal was averaged to calculate the sensitivity profile.

ODF RECONSTRUCTION AND TRACTOGRAPHY: Fiber-tracking was performed using the free software package DSI Studio. DSI Studio supports a variety of reconstruction methods including DTI and QBI. For q-ball reconstruction the following parameters were chosen:

- Highest spherical harmonics (SH) order: 8
- Laplace-Beltrami regularization: 0.006

The maximum SH order truncates the expansion of the measured signal to reduce computation time and to avoid noisy contributions of high order components. A maximum order of 8 is commonly used in the literature [23] and is justified by the results of spherical harmonic decomposition in chapter 10.4. The Laplace-Beltrami regularization parameter also suppresses higher orders in the SH expansion to avoid noise amplification. The regularization parameter describes the degree to which the weights increase for increasing SH orders and was chosen as recommended in the original publication [19].

9.1.3 *Spherical Harmonic Decomposition*

As described in section 5.2, the measured diffusion-weighted signal of each voxel is expanded into a SH series during QBI reconstruction. The SH coefficients can be used to evaluate the relative energy fraction in every order of the expansion. For the analysis of SH energy spectra in this thesis, only even-order contributions were included because the diffusion model assumes antipodal symmetry.

$$\Psi(\theta,\phi) = \sum_{l=2}^{8} \sum_{m=-l}^{l} 2\pi P_l(0) c_l^m Y_l^m(\theta,\phi) \tag{9.3}$$

Non-vanishing energy fractions in higher-order spherical harmonics represent high-frequency surface patterns of the ODF that indicate multiple fiber populations. Therefore, these higher-order contributions represent increased angular resolution in the ODFs. The energy spectrum of the reconstruction can be calculated as the sum over all coefficients in the respective SH order.

$$E_l = \frac{1}{E_T} \sum_{m=-l}^{l} 4\pi^2 P_l(0)^2 c_l^{m\,2} \tag{9.4}$$

9.2 DWI OF PIG HEARTS

The results of the Panini project indicated that the angular resolution of reconstructed fiber pathways suffered from the low diffusion contrast and strong isotropic diffusion compartment found in fixed tissue (cf. 10.1). Although very high b-values were used, angular resolution in fixed specimens analyzed by spherical harmonic decomposition showed no significant improvements compared to in vivo acquisitions (cf. Fig. 10.11). Furthermore, no new fiber structures or crossings of more than two fiber populations were found.

After returning from Boston the project was continued in Mainz, focusing on the impact of tissue fixation on image quality and performance of the fiber-tracking algorithm. The aim of this project was to investigate the feasibility of high-resolution DWI using unfixed animal and human tissue specimens to increase diffusion contrast and angular resolution.

9.2.1 *Comparison of DWI of Fixed and Fresh Tissue*

In order to investigate the impact of tissue fixation on image quality and diffusion contrast, similar tissue models in the fixed and unfixed state needed to be imaged and compared. Because of easier availability and handling, pig hearts were used as models of fibrous tissue in Mainz. This had the additional advantage of allowing the development of an experimental setup for postmortem cardiac DWI and tractography.

Two pig hearts were provided by the Department of Anesthesia of the Johannes Gutenberg University Mainz Medical Center. Both hearts were explanted from pigs that were used in a study investigating the impact of cardiac arrest and reanimation on cerebral perfusion. The first heart had been fixed in Formalin (Roti®-Histofix, Carl Roth GmbH + Co. KG, Karlsruhe, Germany) 6 months prior to this experiment and served as a reference for fixed tissue. The second heart was explanted from a pig which was sacrificed one hour prior to this experiment. The fresh pig heart was placed in saline solution (NaCl 0,9%, B. Braun Melsungen AG, Melsungen, Germany).

Both hearts were imaged on a 3 T Magnetom Prisma (Siemens Healthcare, Erlangen, Germany) using a custom-built 16 channel receive coil array that was originally designed for cardiac imaging in rabbits (cf. Fig. 9.10). Based on the experience with fixed brain tissue, a relatively high b-value compared to typical in vivo values of 5000 s/mm^2 was used and images were averaged 16 times. Table 9.2 shows the acquisition parameters for the comparison of fresh and fixed pig hearts.

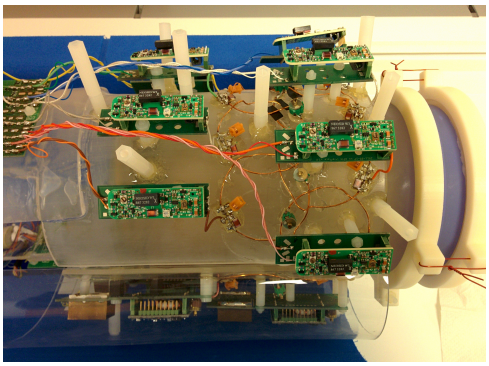

(a) Top part of the coil with 8 receive elements.

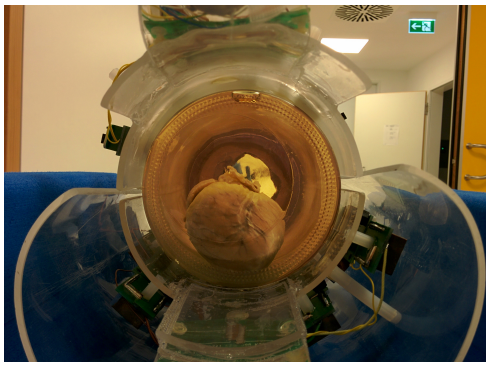

(b) Fixed pig heart inside the sample container.

Figure 9.10: Experimental setup for ex vivo DWI of pig hearts on the Siemens Magnetom Prisma in Mainz.

parameter	value
sequence	2D DW-EPI
TE / TR [ms]	90 / 20 000
resolution [µm]	$800 \times 800 \times 800$
matrix size [p/r/s]	134/196/70
b-value [s/mm^2]	5000
diffusion averages	16
echo spacing [ms]	1.15
bandwidth/pixel [Hz]	1160
acquisition time [h]	1 : 05

Table 9.2: Acquisition parameters for the comparison of fresh and Formalin-fixed pig hearts.

9.2.2 *DWI of the Unfixed Pig Heart*

Based on the results of the aforementioned comparison between fresh and fixed tissue (cf. Fig. 10.13), a more detailed investigation of unfixed tissue was performed. The aim of this study was to evaluate the feasibility of DWI on fresh, unfixed tissue to increase the achievable diffusion contrast. There were three main questions that had to be answered in order to evaluate the feasibility of high-resolution DWI on unfixed human and animal tissue specimens:

- Can continuous imaging at maximum gradient duty cycle over several hours over-heat the gradient system?
- Do T_1 and/or T_2 relaxation times change during data acquisition? If yes, does that introduce a bias for the calculation of the orientation distribution functions?
- Are there structural changes in the tissue after death that may cause misalignment of image volumes acquired at different times during image acquisition? For high-resolution experiments over several hours the first and last volume still need to align to avoid biases in the ODFs.

To address these questions, another fresh pig heart was imaged for an extended period of time where T_1 and T_2 values were monitored. At the time when this experiment was performed, only 12 different diffusion gradient directions, defined by Siemens, could be sampled (cf. A.1). For full QBI acquisitions an additional software license is required which was not yet available on the Magnetom Prisma. As the primary objective of this experiment was to investigate the longterm stability of tissue and hardware, a temporary workaround was used. In order to simulate the duty cycle of a full QBI acquisition with over 200 diffusion directions, the same sequence with 12 directions was repeated continuously. Figure 9.11 shows the timeline of all experiments that were performed on this unfixed pig heart. The b-value was reduced to 2000 s/mm^2 to improve SNR. The temperature of the gradient coil was monitored using the Siemens Local Service application. After the temperatures seemed to approach an equilibrium state after about two hours (cf. Fig. 10.15 on page 93), 7 more sequences with one hour pauses were run to reach the expected acquisition time of the planned QBI experiments. The key question was, whether a structurally stable state can be found that allows continuous imaging of unfixed tissue over several hours (or even days).

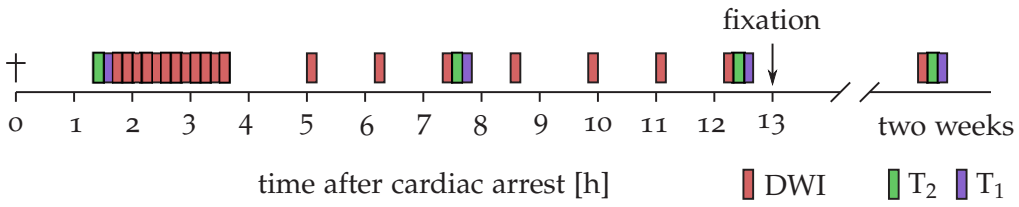

Figure 9.11: Timeline of imaging experiments performed on the unfixed pig heart.

After 13 hours of imaging the heart was placed in a 4 % Formalin solution to allow storage for further investigation. After two weeks in the fixative solution, the heart was imaged again using the exact same DWI and $T_{1,2}$ mapping sequences. Postprocessing steps were performed as described earlier for the fixed human brain specimens with the following exceptions:

Correction of eddy current induced distortions was not possible because the available Siemens diffusion gradient vector tables did not include pairs of anti-parallel vectors. However, only minor distortions were found in the final images and the effect of eddy currents in this experiment was not considered any further. Images were exported in DICOM format because the modified image reconstruction software developed in Boston (dynamic scaling, multi-shot acquisition) was not available on the Magnetom Prisma in Mainz. DTI reconstruction of the orientation distribution functions and deterministic fiber-tracking were performed using DSI Studio. Acquisition parameters for the DWI, T_1 and T_2 mapping sequences are shown in Tab. 9.3.

	DWI	T_1	T_2
sequence	2D DW-EPI	inversion recovery	spin echo
resolution [µm]	$900 \times 900 \times 900$	$800 \times 800 \times 800$	$800 \times 800 \times 800$
matrix [p/r/s]	132/192/90	115/192/1	120/192/1
bandwidth/pixel [Hz]	1446	260	128
b-value [s/mm^2]	2000	-	-
diffusion averages	2	-	-
diffusion directions	12	-	-
TE [ms]	81	16	20.4 to 163.2
TR [ms]	21 600	2500	3000
TI [ms]	-	23 to 2400	-
acquisition time [min]	10 : 06	1 : 04	6 : 05

Table 9.3: Acquisition parameters of the DWI and $T_{1,2}$ mapping sequences used for the unfixed pig heart.

The experiment described above was repeated once the full QBI license was installed on the MRI system. The same gradient vector table of 266 directions as shown in Fig. 9.6 was used. Imaging started four hours post mortem. All other acquisition parameters remained unchanged. In order to evaluate the angular resolution and diffusion contrast at different b-values, an additional experiment was conducted. Diffusion was sampled using 30 equidistant diffusion encoding directions in a 2D plane. The resulting q-space trajectory is a ring and can be used to visualize the 2D water displacement distribution function. For the unfixed pig heart the plane was chosen to show the short axis view of the myocardium.

9.3 DWI OF UNFIXED HUMAN TISSUE SPECIMENS

As will be discussed in chapter 10.3, a structurally stable state was found in the unfixed postmortem pig heart that allowed continuous image acquisition over more than 12 hours with excellent image quality and detailed tract reconstructions. As a next step, this method was transferred to human tissue. The aim of this study was to demonstrate the feasibility of high-resolution DWI of unfixed human brain and heart tissue and to evaluate differences in the imaging properties between human and pig tissue.

A whole human body, which was donated for research purposes, was provided by the Institute of Anatomy of the Johannes Gutenberg University Mainz. The male donor died at age 92 from heart failure with known history of cardiomyopathy and irregular heartbeat. The brain and heart were explanted at the Institute of Pathology 10:30 hours post mortem. Both organs were immediately placed in saline solution (0.9 % NaCl) and transported to the Department of Radiology where all imaging experiments were performed. The use of these tissue specimens for the experiments presented in this thesis was approved by the local ethics board.

The human brain was imaged on the 60 channel Panini coil which was shipped from Boston for this experiment (cf. Fig. 9.2). In order to reduce the FOV and increase spatial resolution, only one hemisphere of the brain was examined. Unfortunately, images from the Panini coil started to show increasingly severe artifacts after 1.5 h of continuous imaging (cf. Fig. 9.12). To protect the coil and MRI hardware from damage, this experiment had to be aborted after having sampled only 120 out of 266 diffusion directions. Of those 120 directions, only the first 60 volumes were free of artifacts and used for further processing.

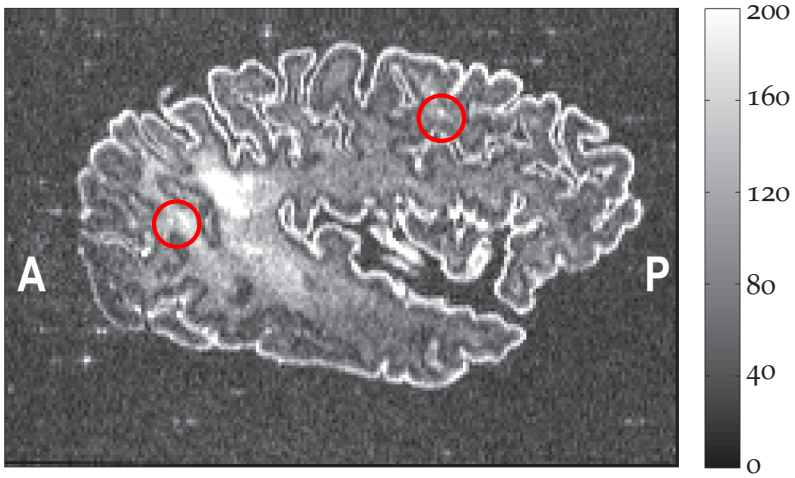

Figure 9.12: Artifacts in images of the unfixed human hemisphere acquired after 1.5 h of continuous imaging using the Panini coil (red circles and bright spots around the sample). Imaging had to be aborted to avoid damage to the coil and MRI hardware.

The human heart was imaged using the 16 channel receive coil that was also used for the pig hearts (cf. Fig. 9.10). A total of 140 directions were acquired, taken randomly from the 266 direction vector table described in section 9.1.1. The full vector table was not used to shorten the required acquisition time and allow further investigation of the brain sample.

After imaging of the heart was finished, the brain hemisphere was imaged again using the spine array of the MRI table together with the Siemens 4 channel "Flex" coil which was placed directly on top of the sample container.

Image acquisition parameters for all three experiments can be found in Tab. 9.4. T_1 and T_2 maps were acquired with the same protocol used for pig hearts, parameters are shown in Tab. 9.3.

	hemisphere	heart	hemisphere
coil	60 ch Panini	16ch Rabbit	Spine + 4ch Flex
sequence	2D DW-EPI	2D DW-EPI	2D DW-EPI
TE/TR [ms]	97/21 600	81/21 600	95/21 600
resolution [mm]	0.9	0.9	1.1
matrix [p/r/s]	144/212/90	134/196/128	174/196/70
echo spacing [ms]	1.08	1.12	0.93
b-value [s/mm^2]	5000	2000	5000
diffusion directions	60	120	140
diffusion averages	4	4	4
acquisition time [h]	1 : 30	3 : 00	3 : 30
PAT	2	2	2

Table 9.4: Acquisition parameters for imaging experiments using unfixed human tissue specimens.

10

RESULTS

10.1 DWI OF FIXED HUMAN BRAIN SPECIMENS

10.1.1 *Image Reconstruction*

First images of the 3D diffusion-weighted multi-shot EPI sequence showed very intense ghosting artifacts (cf. Fig 10.1). Ghosting intensities of up to 60% of the original image were found in several image regions. These artifacts result from phase errors between individual shots and odd/even lines which lead to discontinuities in k-space. While ghosting artifacts are always present in images from multi-shot EPI sequences, their intensity can usually be reduced to less than 10% of the overall image (see section 4.1.5).

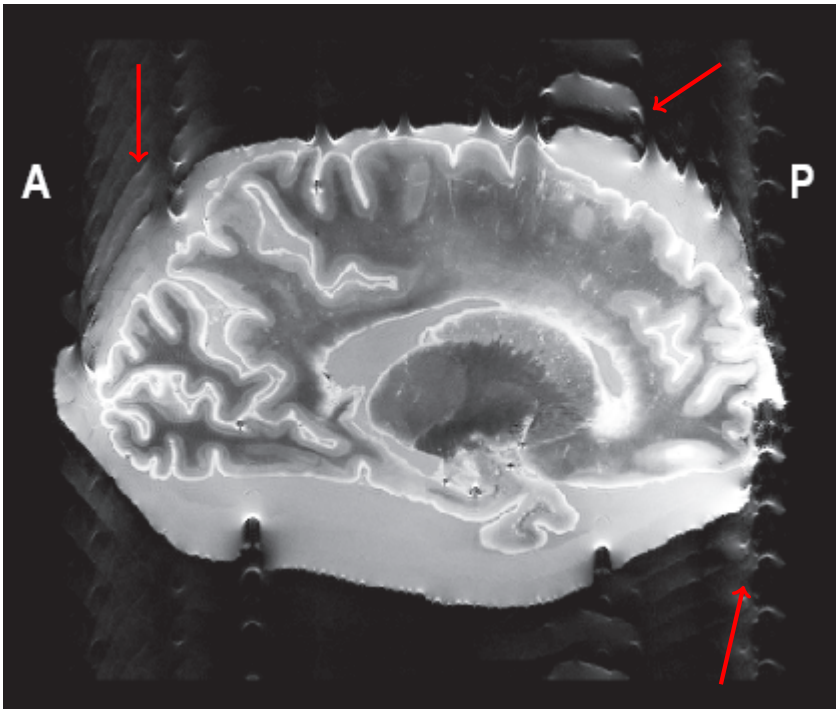

Figure 10.1: Ghosting artifacts in images from the 3D multi-shot DW-EPI sequence using fixed human brain tissue.

Ghosting artifacts in MRI images arise from discontinuities in k-space during Fourier transformation. The most common causes for ghosting are: movement during image acquisition, field inhomogeneities, susceptibility and/or chemical shifts and hardware imperfections [15]. In order to isolate possible factors influencing the observed ghosting, the same sequence was used together with a different coil, a 64 channel head array using a custom-built head phantom [40]. During data analysis, it was noticed that the ghosting level varied heavily between individual receive channels (cf. Fig. 10.2a). Hardware malfunctions were eliminated as a possible source as other imaging sequences did not show any ghosting.

It was therefore assumed, that the phase correction algorithm wasn't performing as intended with the 3D DW-EPI sequence. The online image reconstruction, which is performed by an ICE program, used a phase correction algorithm based on auto- and cross-correlation of the phase navigator signals [2]. However, the phase evolution of the navigator data, which is used to estimate the phase errors, can be inaccurate towards the edges of the spectrum when SNR is low. As a consequence, noise regions in the navigator signal can lead to instabilities of the phase correction algorithm.

Newer versions of the Siemens Syngo software make use of an improved, "local" phase correction algorithm based on [24]. This algorithm introduces an additional weighting of the phase evolution with the signal intensity to suppress possibly erroneous data. This reconstruction method was implemented manually in MATLAB and the results are shown in Fig. 10.2b. A substantial improvement in the ghosting level was observed in most channels.

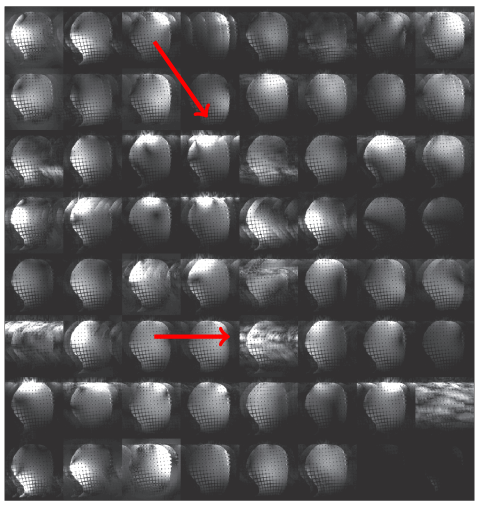

(a) Automatic online phase correction.

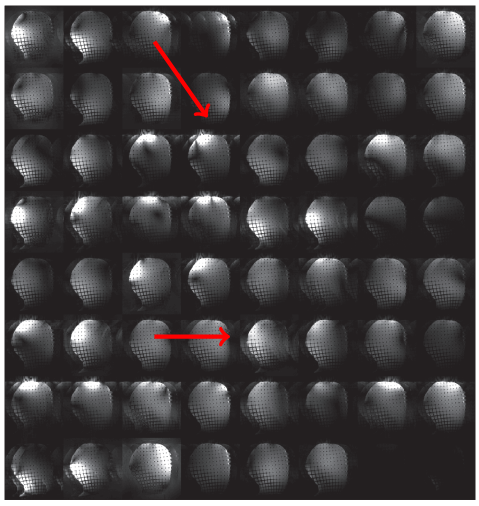

(b) Manual offline phase correction using Feiweier's approach in MATLAB.

Figure 10.2: Analysis of ghosting levels in uncombined images of a 64 channel head array coil using a custom-built head phantom.

Comparison of both methods using data of the Panini coil and adaptive channel combination showed the same improvement in the final images (cf. Fig. 10.3). The initial ghosting intensity of 26%, calculated as the intensity ratio of identical regions in the image and ghost, was reduced to 5%. This motivated the implementation of this phase correction method as an online ICE program which was used for all of the following imaging experiments.

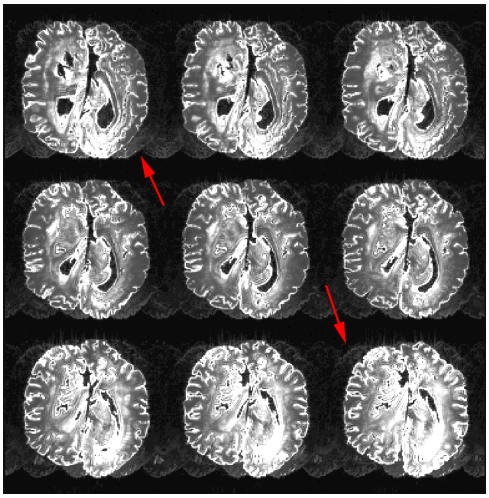

(a) Automatic online phase correction.

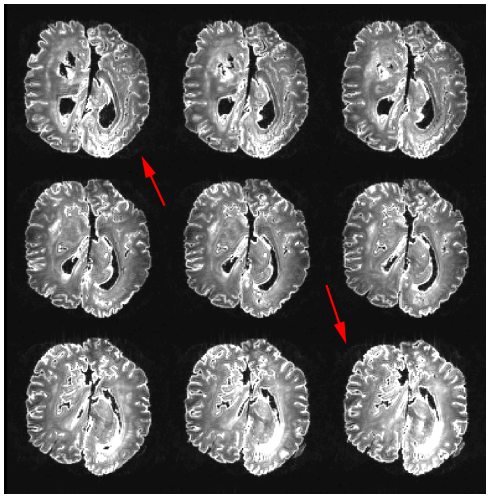

(b) Manual offline phase correction using Feiweier's approach in MATLAB.

Figure 10.3: Analysis of ghosting levels in combined images of the Panini coil using a human brain tissue phantom. a) Images reconstructed with the standard phase correction show a substantial ghosting level (red arrows). b) Implementation of the "local" phase correction method almost completely removed ghosting from the images.

Figure 10.4 shows the measured T_1 and T_2 maps of the fixed human hemisphere. On average, both relaxation times were significantly lower than reported in vivo mean values (cf. Tab. 10.1). Within the sample, a slight transition to shorter relaxation times can be observed from the center towards the outer brain regions. Additionally, minor variations are visible where the border between white and gray matter is to be expected.

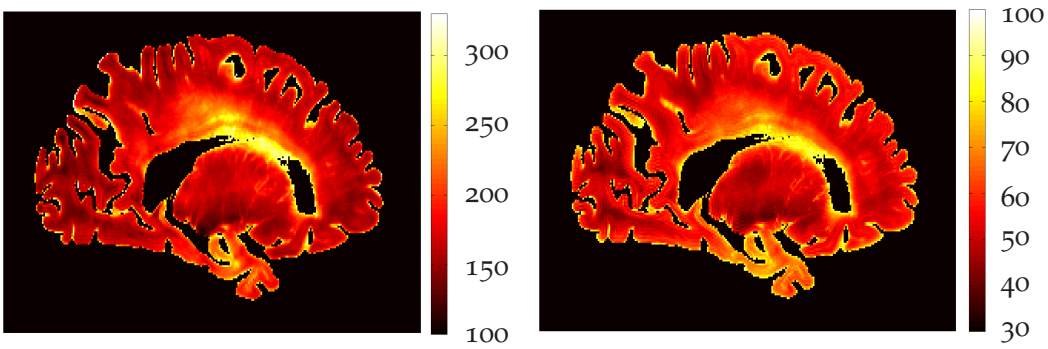

(a) T_1 map [ms] (b) T_2 map [ms]

Figure 10.4: T_1 and T_2 maps of the fixed human hemisphere. The sample had been fixed with Formalin for several years at the time of this study.

	temperature °C	T_1 [ms]	T_2 [ms]
ex vivo	22	200	60
in vivo	37	830	110

Table 10.1: Comparison between average relaxation times found in fixed human brain tissue using the proposed method and reported in vivo values taken from [76]. T_1 and T_2 values dropped to 24% and 56% of their in vivo values, respectively.

10.1.2 *Spatial Resolution and SNR*

Maximum spatial resolution of the presented setup was analyzed using the two human brain tissue samples shown in Fig. 9.3. In the case of the hemisphere, an isotropic spatial resolution of 500 µm with high SNR was achieved. The maximum resolution of this sample was not limited by SNR but by the image matrix size and field of view (FOV) of the imaging pulse sequence. At the minimum FOV required to cover the full sample volume, the maximum matrix size could not be increased above the limits given in table 9.1 which resulted in a maximum resolution of 500 µm. Unfortunately, the source code of the sequence was not available to further investigate the source of these limitations.

In order to further increase spatial resolution and to explore the SNR limits of this setup, smaller FOVs had to be used. By using the smaller coronal slab sample, an isotropic spatial resolution of 350 µm was achieved. SNR at this resolution was very low and barely sufficient to reconstruct the orientation distribution functions for tractography. Thus, this data set represents the maximum workable resolution of the Panini setup.

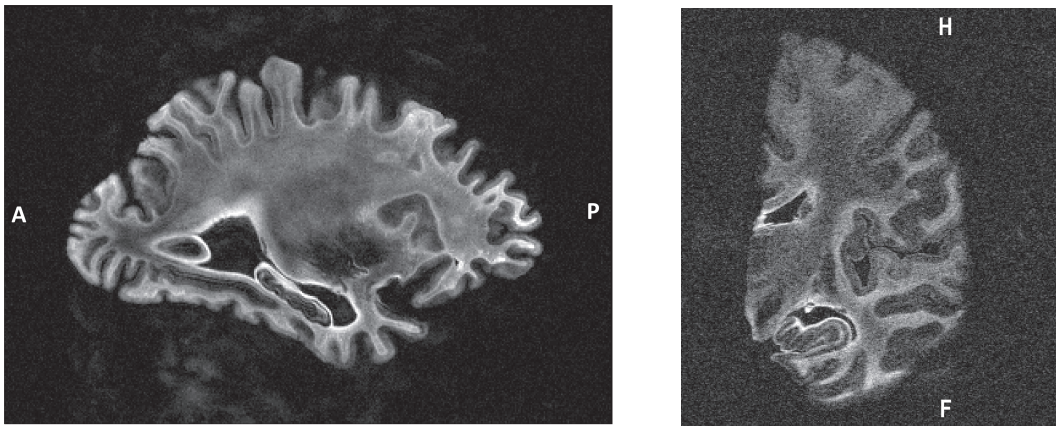

(a) Whole human hemisphere at 500 µm isotropic resolution.

(b) Coronal slab at 350 µm isotropic resolution.

Figure 10.5: DWI images of the two fixed human brain tissue specimens used in this study at maximum spatial resolutions and $b = 30\,000\,\mathrm{s/mm^2}$.

The performance of the Panini coil was quantitatively evaluated by comparison of SNR and $1/G$ maps with those of the 64 channel head array which is used in the HCP in vivo protocol [40]. As seen in Fig. 10.6a, the mean SNR of the Panini coil is about 2-fold higher over the whole sample and up to 4-fold at the Panini coil surfaces. For parallel imaging, acceleration factors of up to 6 or 4×4 can be realized with acceptable SNR penalties (based on a 20% SNR loss limit). Even $R = 5 \times 5$ may be feasible when smaller samples are used as SNR losses are confined to the lower edge of the image.

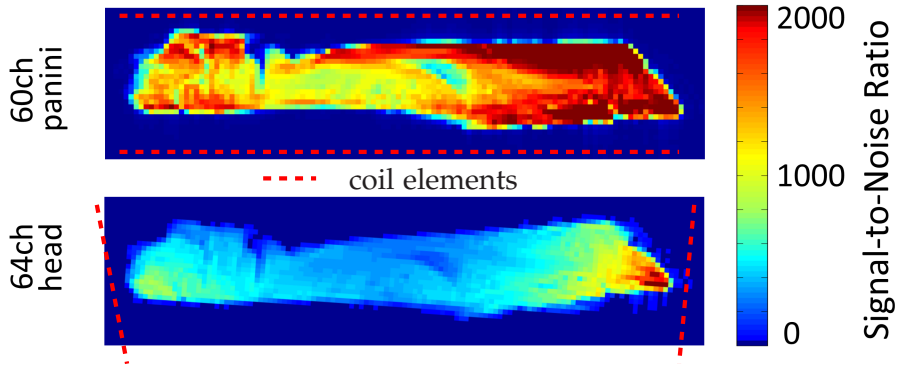

(a) SNR maps in sagittal view.

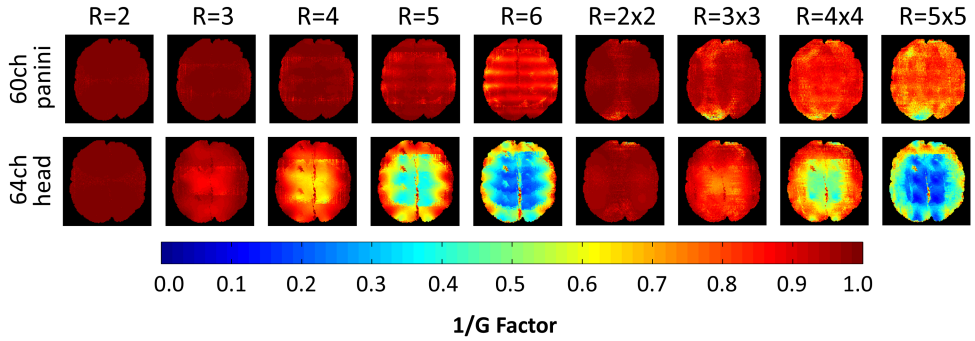

(b) $1/G$ factor maps in transverse view for one- and two-dimensional acceleration factors R.

Figure 10.6: Comparison of SNR and 1/G-factor maps of the 60 channel Panini coil and a 64 channel head array. a) In the head array, the phantom was positioned in a similar way as it would be in a living patient for better comparability. The position of coil elements along the samples in is indicated by dashed red lines.

As mentioned in section 9.1.1, the maximum gradient amplitude available for diffusion encoding plays an important role for the achievable minimum echo time TE_{min}. Using stronger diffusion gradients, the same b-value can be achieved with shorter gradient durations (cf. Eq. 3.17), thus reducing TE_{min}. With very short relaxation times in fixed tissue, the echo time needs to be as short as possible to avoid SNR losses due to T_2 decay.

In order to demonstrate the advantage of the $300\,\text{mT}\,\text{m}^{-1}$ gradients of the Human Connectom MRI system, the maximum gradient amplitude was manually limited in the parameter map of the imaging pulse sequence. The limits were chosen to represent gradient systems available on the Magnetom Connectom ($300\,\text{mT}\,\text{m}^{-1}$), the Magnetom Prisma ($80\,\text{mT}\,\text{m}^{-1}$) and typical clinical MRI systems ($40\,\text{mT}\,\text{m}^{-1}$). The resulting echo times are given in Tab. 10.2. Additionally, the theoretical T_2 weighting factor for the reported average T_2 time of 60 ms is given to evaluate expected SNR losses at longer echo times.

MRI system	gradient amplitude [mT m^{-1}]	TE_{min} [ms]	$\exp\left(\frac{TE_{\text{min}}}{T_2}\right)$
Magnetom Connectom	300	79	0.268
Magnetom Prisma	80	126	0.123
Clinical standard	40	179	0.051

Table 10.2: Minimum echo times of the 3D multi-shot DW-EPI sequence for three different gradient systems. All other acquisition parameters are identical with those given for the coronal slab in Tab. 9.1. The theoretical T_2 weighting factor was calculated at the time TE_{min} with the reported average T_2 relaxation time of 60 ms.

As can be seen from the T_2 weighting factors, the shorter echo times available on the Magnetom Connectom allow for substantially higher SNR values compared to commercially available MRI systems.

10.1.3 *Tractography*

ODF reconstruction and tractography of both tissue specimens were performed using DSI Studio. The high spatial resolutions of 500 µm and 350 µm resulted in a 27-fold and 79-fold increased ODF density, respectively, compared to the HCP reference data at 1.5 mm resolution (cf. Fig. 10.7). These values were calculated as the ratio of voxel volumes relative to the in vivo data.

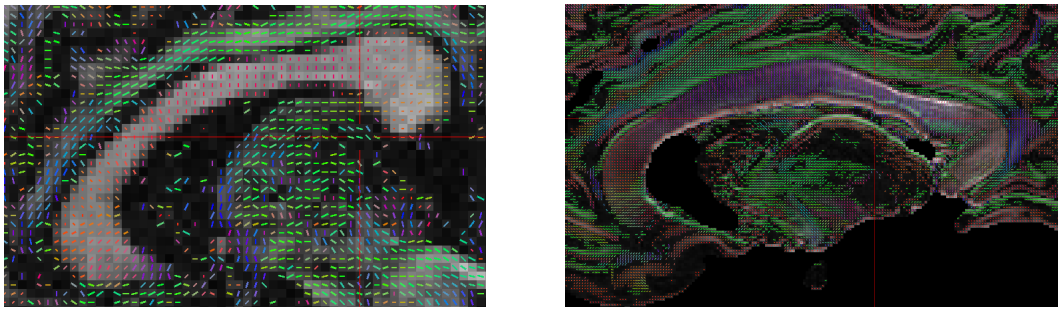

(a) in vivo HCP, 1.5 mm (b) ex vivo Panini, 500 µm

Figure 10.7: Comparison of ODF densities in the corpus callosum.

Figure 10.8 shows the raw tracking results that DSI Studio reconstructed from the diffusion data of the fixed human hemisphere. Large coherent fiber bundles are already visible as they appear as bright structures in the image. At the same time many fine features, especially towards the outer brain regions, can be observed.

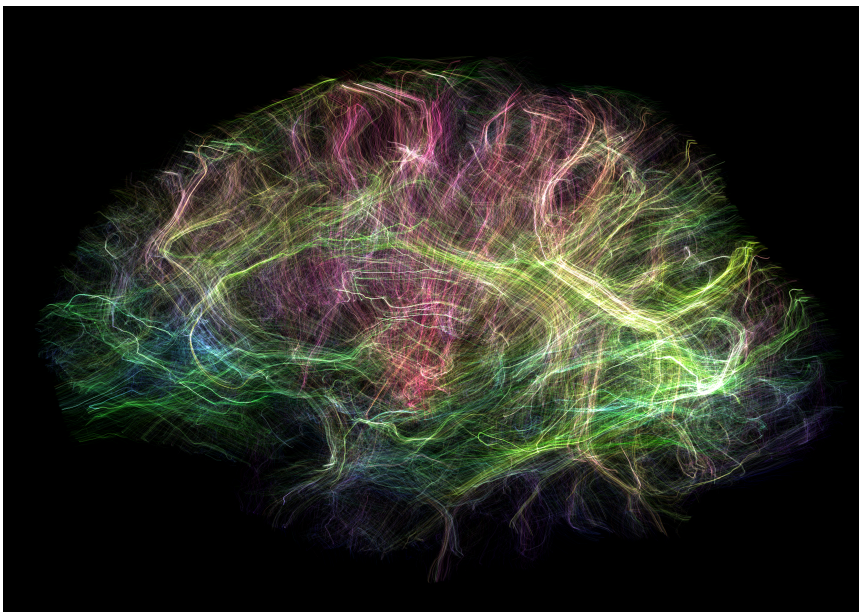

Figure 10.8: Unfiltered tracking results of the whole human hemisphere at 500 µm isotropic resolution. Fibers are color-coded to show their orientation and displayed with 80 % opacity to improve visibility of large fiber bundles.

Figure 10.9 shows a comparison of image quality and tract reconstructions between both ex vivo Panini data sets and the HCP in vivo reference. Although all three brains were anatomically different, coronal slices at similar locations were used for the comparison.

The top row shows images without diffusion-weighting (b_0 images) which are T_2-weighted due to long echo times typical for diffusion imaging. Note that the fixative Formalin was replaced by Fomblin for the experiments at 350 µm resolution. Fomblin has the advantage of being invisible on MRI images but needs to be refrigerated. In this case Fomblin was used to allow for mask generation based on intensity thresholds in b_0 images as the diffusion-weighted images were too noisy in some brain regions.

The second row shows images with high b-values and thus, strong diffusion attenuations. While only a few structures are visible in the in vivo data, both ex vivo samples show uniform signal intensities throughout the brain. This results from a strong isotropic diffusion compartment as a consequence of tissue fixation. Note that at 350 µm isotropic resolution, a substantial noise level is observed. While the border between gray and white matter is barely recognizable in the HCP data, it is well pronounced in both ex vivo data sets.

The third row shows exemplary q-ball fiber reconstructions in all three data sets. Tracts were reconstructed from the corpus callosum and corticospinal tract. Both ex vivo reconstructions show significantly higher levels of detail as a result of the increased ODF density. At 500 µm, the intersection of both tracts is accurately reconstructed. Unfortunately, these fiber crossings are barely visible in the 350 µm data set because the crossing area was not part of the sample region.

Figure 10.10 shows magnified views of selected fiber pathways at 350 µm resolution. In the upper part of the image, fibers of the superior longitudinal fasciculus (SLF, green) are shown as they pass the corpus callosum in close proximity. The SLF is one of the longest neuron tracts in the human brain but is small in diameter. As a consequence, only very few ODFs are typically available for reconstruction in in vivo data sets. Fiber reconstructions in the region indicated by the blue box accurately map the strongly curved short association fibers ("U fibers") between neighboring gyri. These fine features are often not present in in vivo reconstructions.

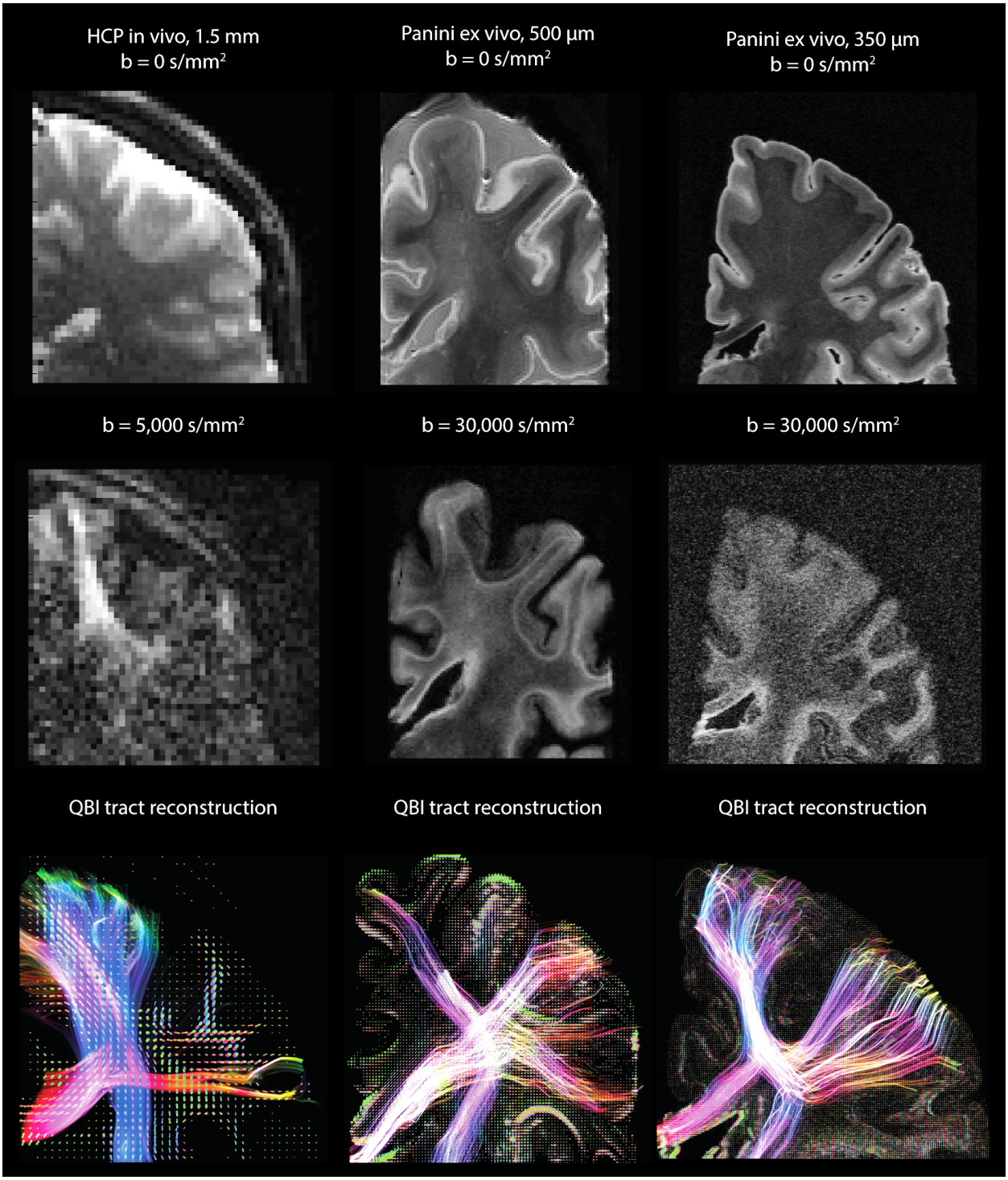

Figure 10.9: Comparison of diffusion-weighted images and the resulting fiber reconstructions between typical in vivo and ex vivo Panini data. In both ex vivo data sets anatomical features and fiber structures are significantly better elaborated.

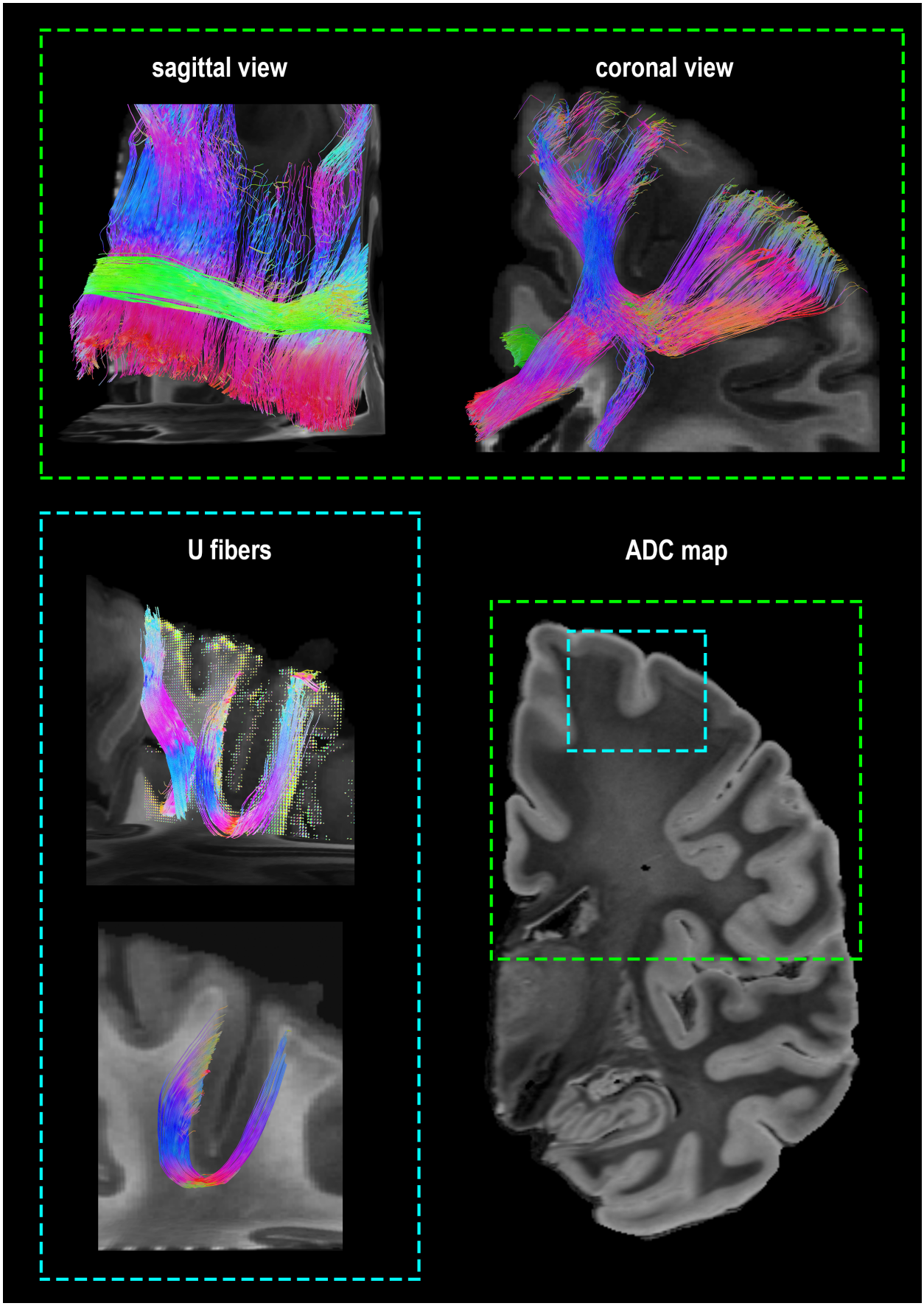

Figure 10.10: Exemplary tract reconstructions obtained from the 350 µm Panini data.

10.1.4 *Angular Resolution*

As described in chapter 9.1.3, angular resolution can be analyzed using spherical harmonic decomposition (SHD). The energy fraction of every order in the expansion is given by the sum of SH coefficients in the respective order and represents the degree to which this order contributes to the final ODF. Higher orders in the SH expansion of the diffusion signal correspond to finer surface features of the ODF. Therefore, higher energy fractions in high SH orders indicate increased angular resolution.

Fig. 10.11 shows the SH energy spectra of the fixed human hemisphere at 500 µm resolution and reported in vivo results from Fan et. al. [23]. This comparison is not entirely fair because different numbers of diffusion directions were sampled which influences the angular resolution. Therefore, a sub-sampled version of the ex vivo data set with 140 out of 266 directions was added to the comparison. The choice of 140 directions is based on the acquisition scheme which sampled multiple sets of 20 directions each. The spectra show very similar energy fractions for all three data sets with slight deviations in SH orders four and six.

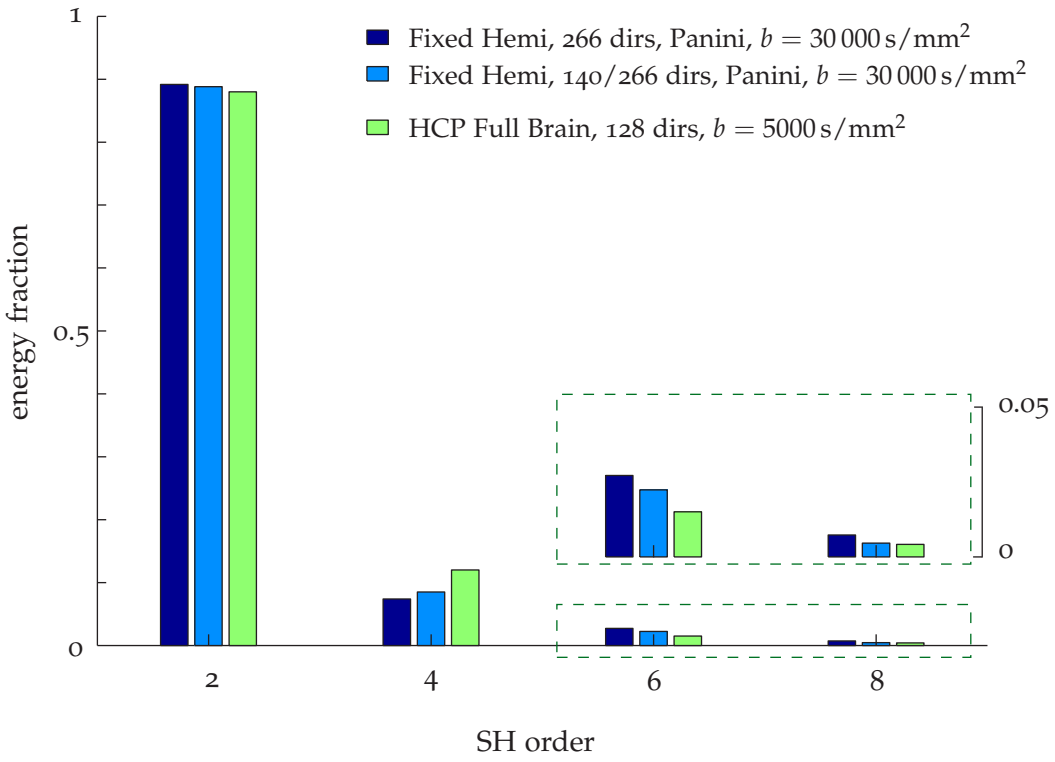

Figure 10.11: Mean SH energy spectra of the fixed postmortem hemisphere and in vivo results published in [23].

This result was unexpected in several ways. First, using only 140 out of 266 diffusion directions should have a significant impact on the angular resolution and thus, the SH spectrum. The fact, that the energy fractions remain almost constant indicates that another limitation for the achievable angular resolution was already reached at 140 directions. Furthermore, the ex vivo experiments were expected to achieve substantially higher angular resolution compared to the HCP in vivo

data. Apparently, sampling more diffusion directions at higher b-values in fixed postmortem tissue does not result in an increased angular resolution.

As the spherical harmonic decomposition is performed for every voxel of the image, it is also possible to calculate maps of the relative energy contributions in every SH order (cf. Fig. 10.12). For orders larger than two similar energy distributions in the fixed hemisphere were found. Bright areas agree well with known crossing fiber regions where up to three fiber populations were identified in the paper from Fan et. al. [23].

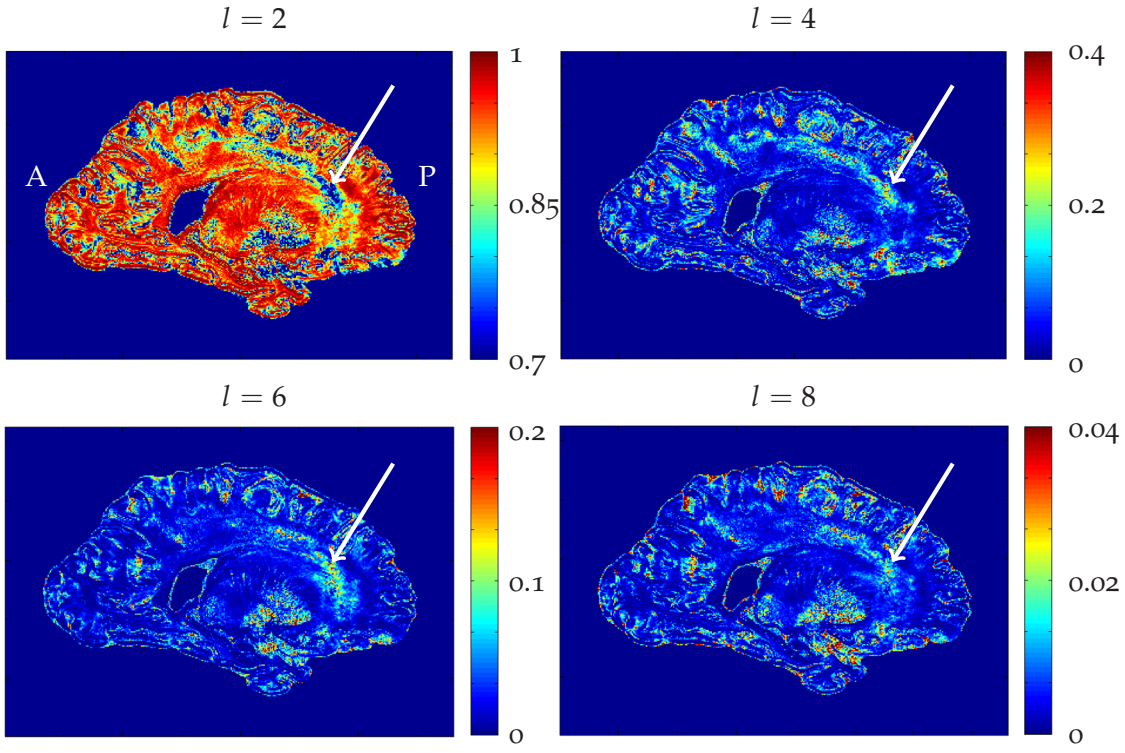

Figure 10.12: Maps of SH coefficients in the fixed human hemisphere (sagittal view). Regions with crossing fibers show higher energy fractions in SH orders larger than two (see white arrows). Color-coding of the images is scaled to emphasize structural features in the tissue.

10.2 COMPARISON OF FRESH AND FIXED PIG HEARTS

In order to evaluate the impact of tissue fixation on signal intensity and diffusion contrast, one fresh and one Formalin-fixed pig heart were imaged using the exact same experimental setup. Figure 10.13 shows the resulting b_0 and diffusion-weighted images. While the b_0 images do not suggest significant variations between fresh and fixed tissue, dramatic differences become evident at a b-value of $5000\,\mathrm{s/mm^2}$. The Formalin-fixed heart is almost invisible in the diffusion-weighted image. The fresh heart shows decent signal intensity and detailed structural features are visible. Although the slice orientation does not align with typical clinical conventions, the left and right ventricles can be easily identified. These observations confirmed the hypothesis that DWI of fresh tissue yields significantly higher SNR values.

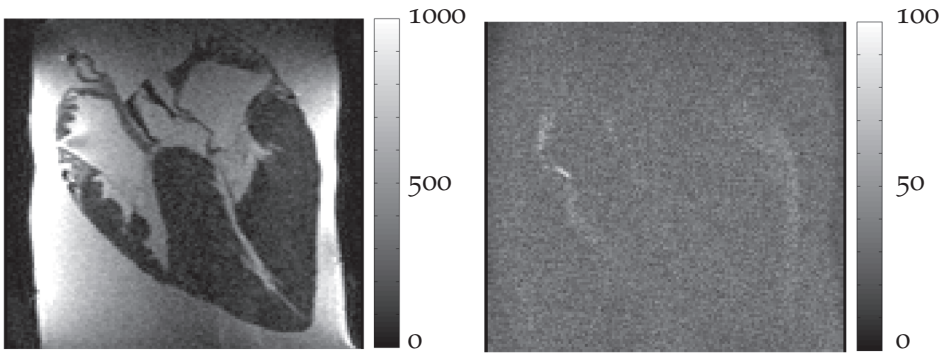

(a) Pig heart fixed in Formalin for 6 months.

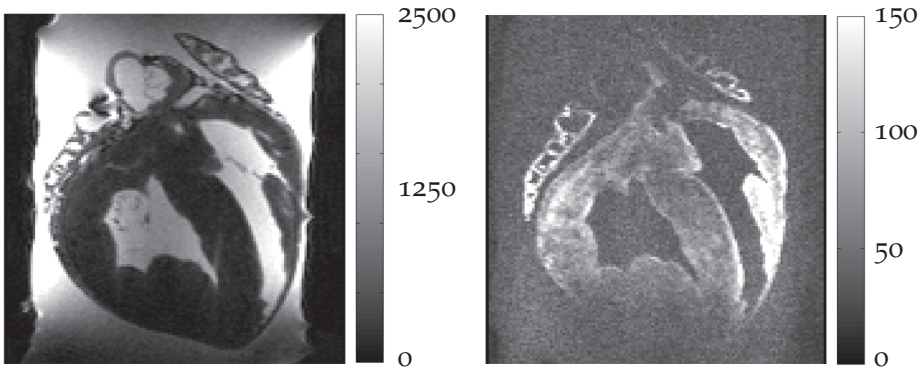

(b) Unfixed pig heart one hour post mortem.

Figure 10.13: Comparison of DWI images of fresh and fixed pig hearts using the same experimental setup at $b = 0\,\mathrm{s/mm^2}$ (left) and $b = 5000\,\mathrm{s/mm^2}$ (right).

Based on these findings, a deeper investigation of the imaging properties of unfixed tissue was initiated. The key question was, whether the experiments presented in section 10.1.3 could be transferred to cardiac tissue, in particular using unfixed specimens to further increase spatial and angular resolution of QBI tractography.

10.3 DWI OF UNFIXED PIG HEARTS

Image Quality

Post-mortem DWI requires thorough planning and preparation as the available time window for imaging experiments is quite short. Tissue degradation processes start immediately after cardiac arrest and the organ will be exposed to air during explantation and to saline solution during imaging. Additionally, the ambient temperature drops from body temperature (~37 °C) to room temperature (~20 °C) during the experiment which is likely to affect the observed diffusion coefficients (cf. Eq. 2.4). In the literature extensive research on the topic of postmortem changes in muscle has been published in the context of meat production [12]. In order to investigate the impact of these factors on the results of diffusion tractography and to study structural changes that might occur during data acquisition, a fresh pig heart was subjected to continuous imaging over the first 13 hours post mortem. Figure 10.14 shows exemplary b_0 and diffusion-weighted images that were acquired two hours post mortem. Left and right ventricles show decent SNR and anatomical detail in both images. The fixative solution appears bright in the T_2-weighted b_0 image (so-called "T_2 shine through") and is fully attenuated at a b-value of 2000 s/mm^2. Note that slices do not align with clinical conventions as the sampling volume was chosen to avoid aliasing artifacts from the sample container and to minimize the field of view (FOV).

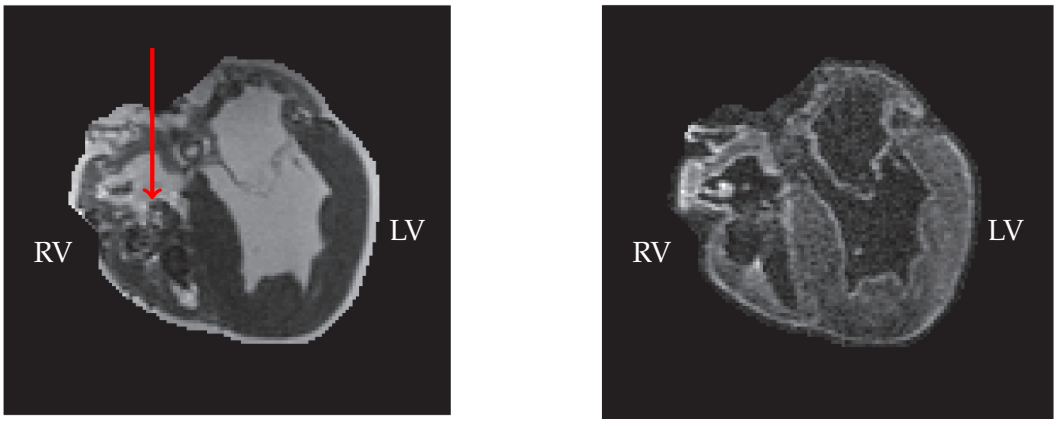

(a) $b = 0\,\mathrm{s/mm^2}$. (b) $b = 2000\,\mathrm{s/mm^2}$.

Figure 10.14: Exemplary masked images of the unfixed pig heart acquired two hours post mortem. The right ventricle (RV) shows minor artifacts due to residual coagulated blood (red arrow).

Gradient System Heating

Heating of the gradient system at maximum duty cycle was monitored using the built-in temperature probes which are accessible through the Siemens Local Service application. This measurement was crucial for the planned ex vivo DWI experiments as the hardware is not designed for continuous operation over several hours or even days. The measured temperature curves of all 12 probes are shown in Fig. 10.15.

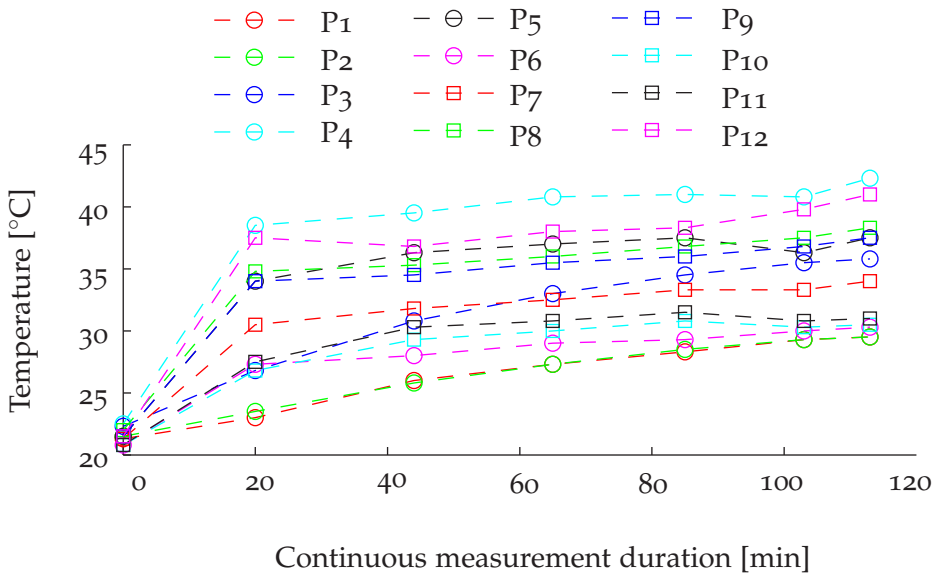

Figure 10.15: Development of temperatures along the gradient coil during continuous diffusion-weighted imaging at maximum gradient amplitude. Curves of all 12 temperature probes (P1-P12) are shown.

Starting from about 22 °C at the beginning of the experiment, temperatures rose quickly within the first 20 minutes. After this initial heating phase, temperatures settled just under 45 °C which is well below the automatic shutdown threshold of the Magnetom Prisma of 80 °C [1]. The temperature probes showed similar tendencies but reached different maximum temperatures which is due to their position along the gradient coil.

Although the exact coil design is confidential, Siemens confirmed that the probes are distributed over primary field-effective gradient coils, shielding coils and power connectors. Probe 4, which reached the highest temperature in Fig. 10.15, monitors the primary x gradient coil where higher temperatures are to be expected. Probes 1 to 3 monitor the power supply connectors for the three field-effective coils and reached low to medium temperatures.

1 This value was provided by the Siemens service specialist responsible for maintaining this MRI system.

Tissue Properties

Exemplary T_1 and T_2 maps of the unfixed pig heart are shown in Fig. 10.16. Both relaxation parameters show homogeneous distributions within the myocardium but significantly higher values in the atria. A region-of-interest approach was used to evaluate the temporal evolution of both relaxation times to reduce statistical errors. Figure 10.17 shows the results of monitoring T_1 and T_2 over the first 13 hours post mortem and an additional measurement after two weeks in Formalin. T_1 and T_2 relaxation times did not show significant drifts over the course of the imaging experiments. However, after two weeks in Formalin both relaxation times showed the expected decrease.

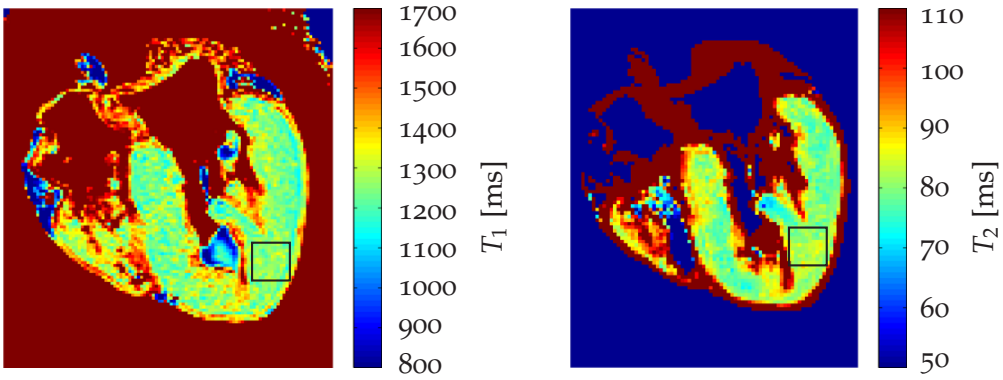

Figure 10.16: T_1 and T_2 maps of the unfixed pig heart 7:30 hours post mortem and regions of interest in the myocardium that were used to evaluate the temporal evolution of T_1 and T_2.

Judging from the presented T_1 and T_2 curves, a structurally stable state of the pig heart is reached after about 5 hours post mortem which may allow acquisition of high-resolution images with a high number of sampled diffusion directions. A limitation for the required acquisition time of several hours might then be the formation of gas bubbles in the tissue which leads to susceptibility artifacts.

Tractography

Figure 10.18 shows results of tractography performed on the averaged data of all 19 DTI acquisitions. The two ventricles are clearly visible along with parts of the aorta and pulmonary trunk. The regions of both atria were excluded from fiber tracking as they showed a high number of noisy fibers. This can be attributed to a different tissue type and agrees with the significantly longer relaxation times found in both atria (cf. Fig. 10.16).

In the short axis view, fibers in both ventricles show the expected circular orientation which is essential for the heart's contraction. Additionally, a transmural transition in the color-coding of the myocardium can be observed which results from a helical fiber distribution. This agrees with a sheet-like helical structure of

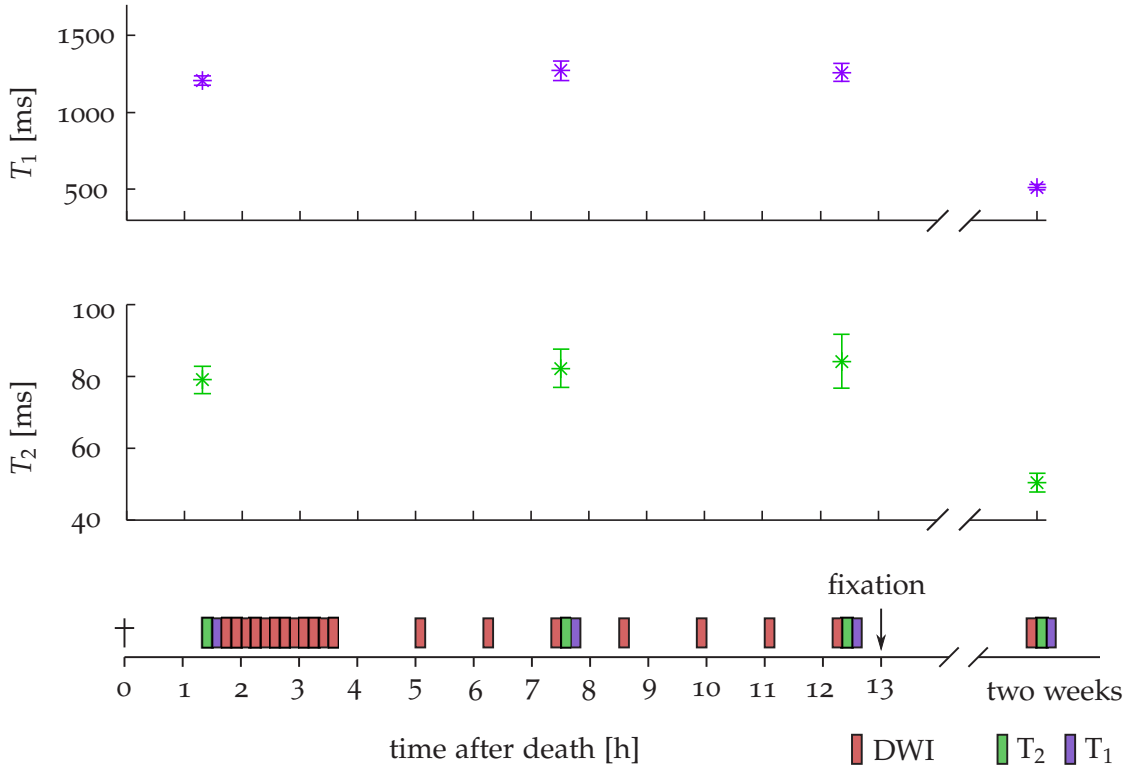

Figure 10.17: Timeline of imaging experiments performed on the unfixed pig heart together with monitored parameters T_1 and T_2.

the myocardium previously reported in rats [66]. Similar fiber configurations in the human heart were found in histological studies [43].

Furthermore, the aorta and pulmonary trunk were reconstructed with great detail. The fact, that both vessels are visible in the tract reconstruction demonstrates the fibrous nature of the vessel wall tissue. This fiber structure provides the high elasticity needed to regulate and smooth the strong variations in blood pressure during the cardiac cycle (cf. Windkessel effect). Figure 10.19 shows enlarged views of the origin of the right coronary artery. The view from inside the heart reveals a large area of circular fibers in the aortic wall that connects aortic fibers with those from the coronary artery. Similar to the aorta itself, the walls of the coronary artery show anisotropic diffusion but fiber reconstructions were less accurate.

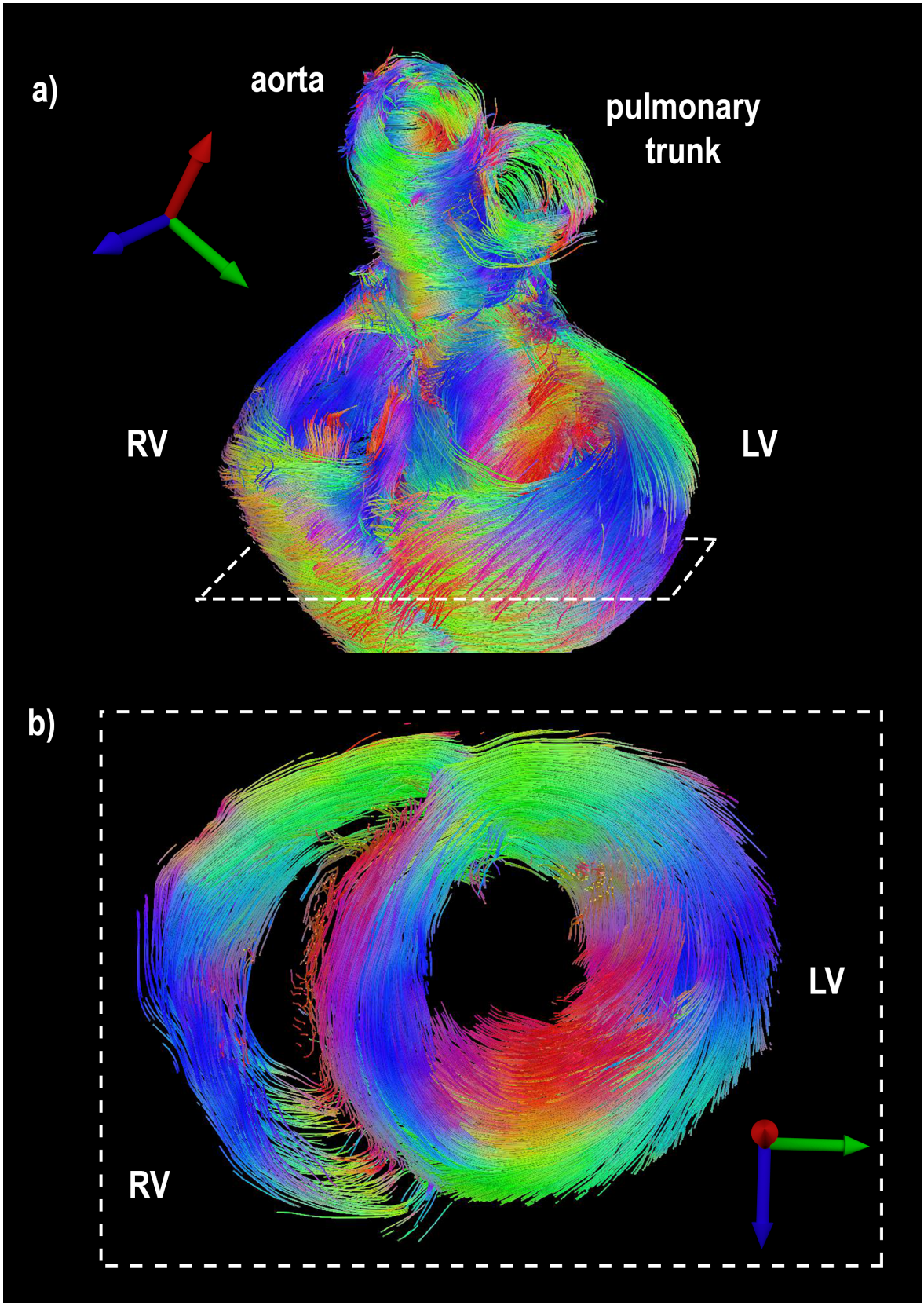

Figure 10.18: Results of DTI-based tractography performed on the DWI data of an unfixed pig heart in saline solution: a) Full fiber reconstruction using all reconstructed ODFs. Left ventricle (LV), right ventricle (RV), the aorta and pulmonary trunk are clearly visible. Fibers of both atria are omitted for the sake of clarity. b) Short axis view of circular myocardial fibers showing a helical sheet-like fiber architecture.

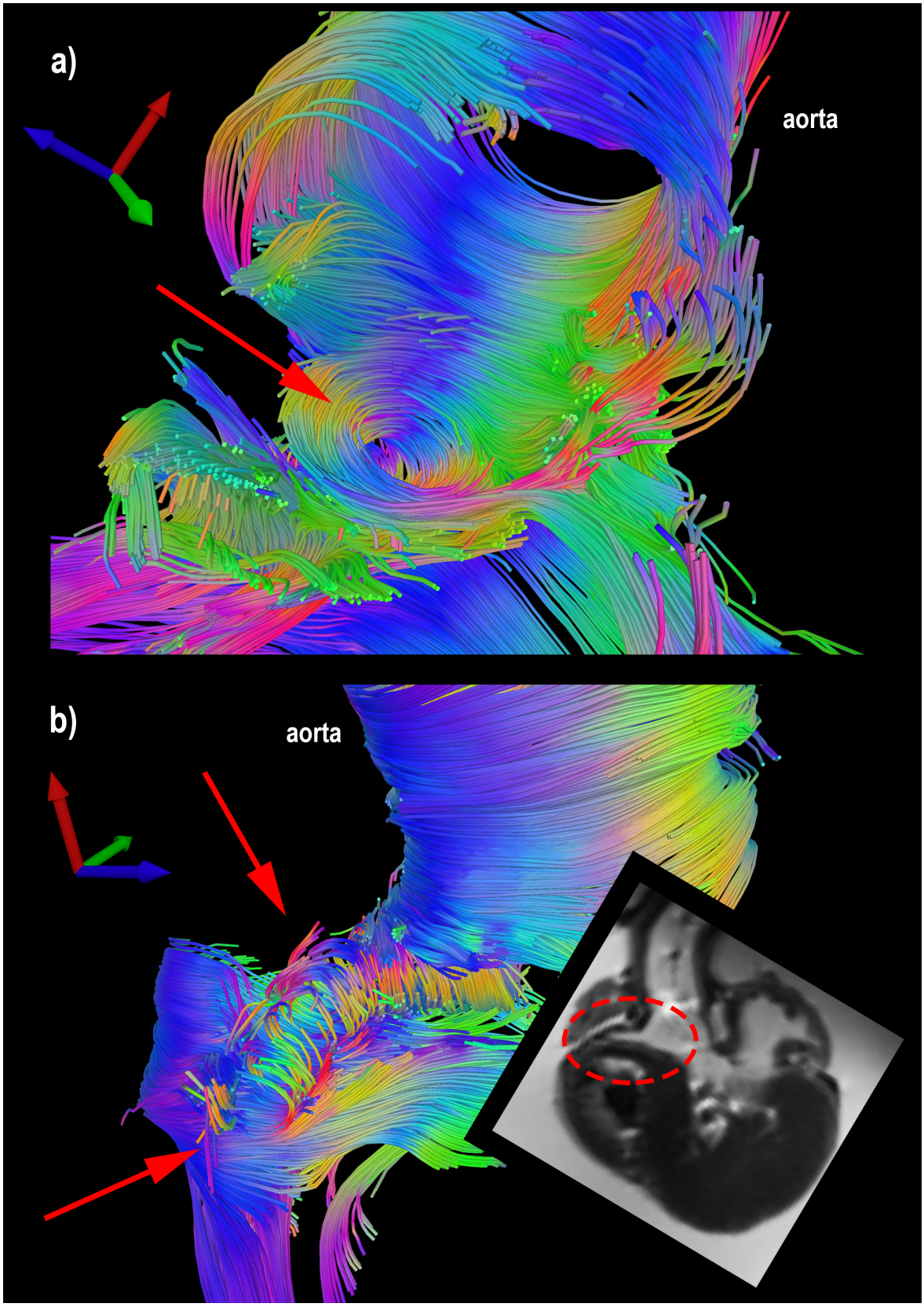

Figure 10.19: Fiber reconstruction around the origin of the right coronary artery (red arrows): a) View from within the heart into the aorta and right coronary artery. b) View from the outside showing partial fiber reconstructions of the first 2 cm of the right coronary artery. The same region is also highlighted in a b_0 image to provide an anatomical reference.

After two weeks in Formalin, the same heart was imaged again using the same experimental setup and DTI imaging sequence. Images showed significantly reduced SNR, especially towards the center of the coil volume. As a consequence ODF reconstruction failed in many areas of the heart. Fig. 10.20 shows the results of tractography performed on the remaining ODFs. The left and right ventricle can still be identified but show very noisy, incoherent fiber reconstructions towards the upper part of the image.

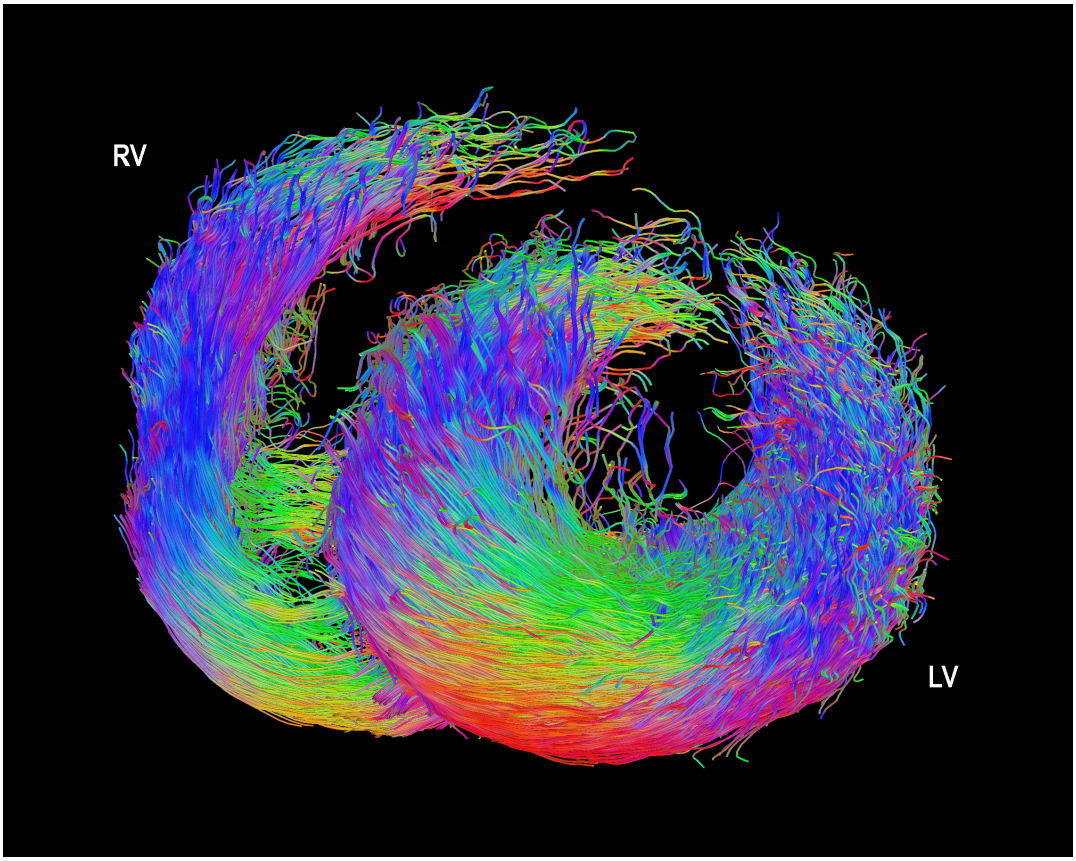

Figure 10.20: Tractography results in short axis view of the same pig heart as in Fig 10.18 b) after two weeks in Formalin solution.

Fig. 10.21 shows the results of sampling a ring of 30 in-plane diffusion directions in the short axis view of the unfixed pig heart. For three regions of interest (ROI) the measured mean signal intensities in the direction of the diffusion encoding gradients are shown. The resulting distributions are equivalent to 2D ODFs and agree with known fiber orientations in the respective regions. With increasing b-value, the eccentricity of the distributions increases which demonstrates increased angular resolution. In Fig. 10.21 c), only the highest b-value of 5000 s/mm^2 revealed multiple fiber directions within this ROI. However, in this region only one fiber orientation was expected. A possible explanation for this discrepancy may be the large area of the ROI which includes several layers of the aforementioned helical

tissue structure in the myocardium. For all ROIs, the ODF volumes decrease with higher b-values due to stronger signal attenuation and lower SNR. This trade-off between angular resolution and SNR creates the need to optimize the b-value for every DWI experiment.

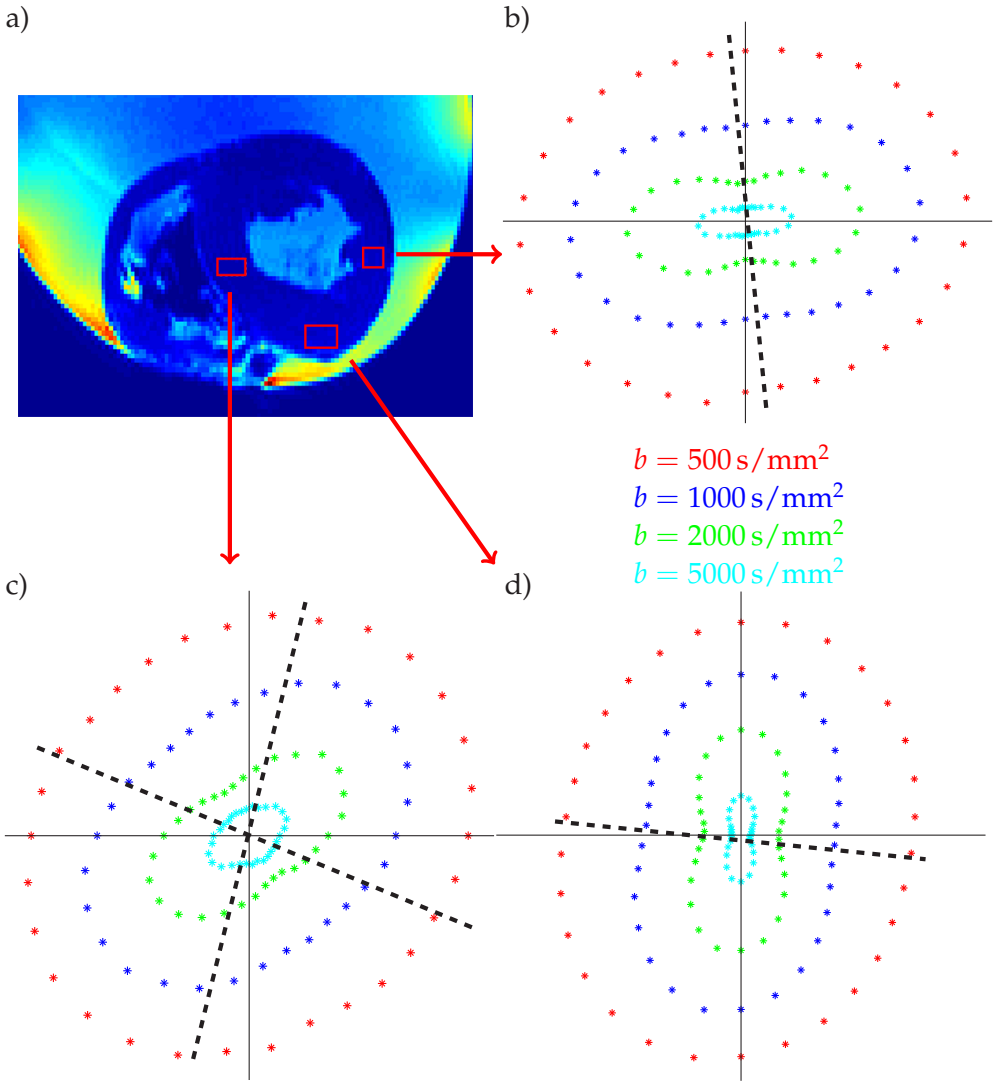

Figure 10.21: 2D sampling of diffusion attenuation profiles in the left ventricle of the unfixed pig heart. The 2D profiles were sampled using 30 equidistant in-plane diffusion encoding directions in the short axis view (a). Signal distributions from three regions of interest for different b-values are shown in (c-d). The detected fiber directions align with the minima of the respective profiles as indicated by the dashed black lines.

Once the full QBI license was installed on the Magnetom Prisma in Mainz, the above experiment was repeated using a new, fresh pig heart. Figure 10.23 shows the results of tractography performed on the QBI data set. Fibers in the myocardium show the same helical structure with a transition of the helix angle from epicardium to endocardium (transmural transition). Fiber reconstructions agree very well with reported structures in the human heart obtained from histology in [43].

The reconstructed fiber pathways look very similar to those from the DTI data set. This is a consequence of the heart's tissue structure which is dominated by coherent fiber bands with very few fiber crossings. This can also be seen in the spherical harmonic energy spectrum where over 97 % of the energy is found in second order terms (cf. Fig. 10.22). These second order contributions are equivalent to the tensor representation. Under these conditions, DTI performs very well which is why the QBI reconstruction doesn't show additional features in the myocardium.

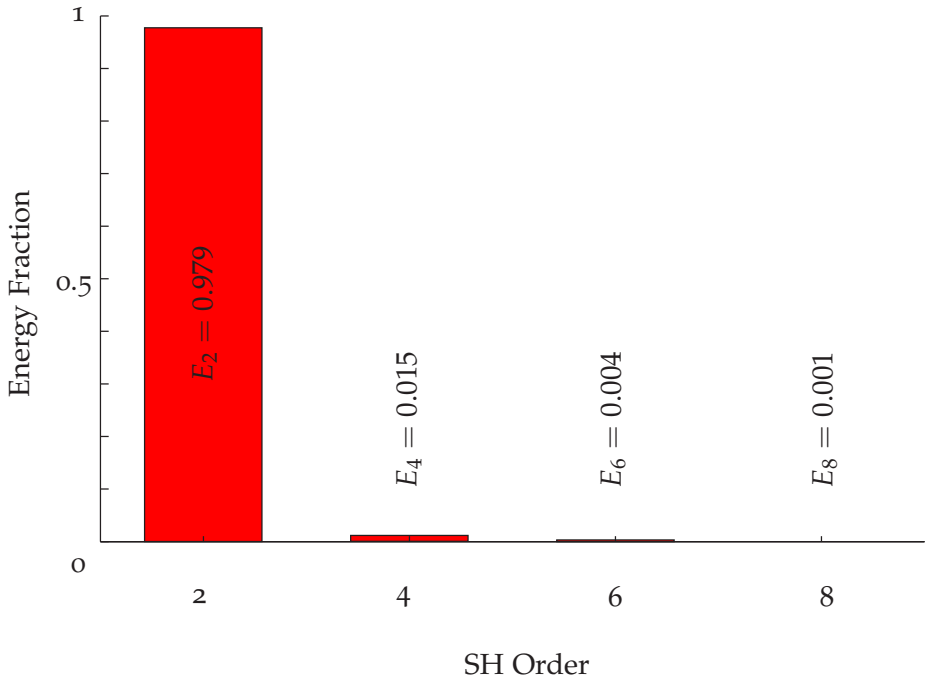

Figure 10.22: Spherical harmonic energy spectrum of the unfixed pig heart. Over 97 % of the total energy is found in second order terms.

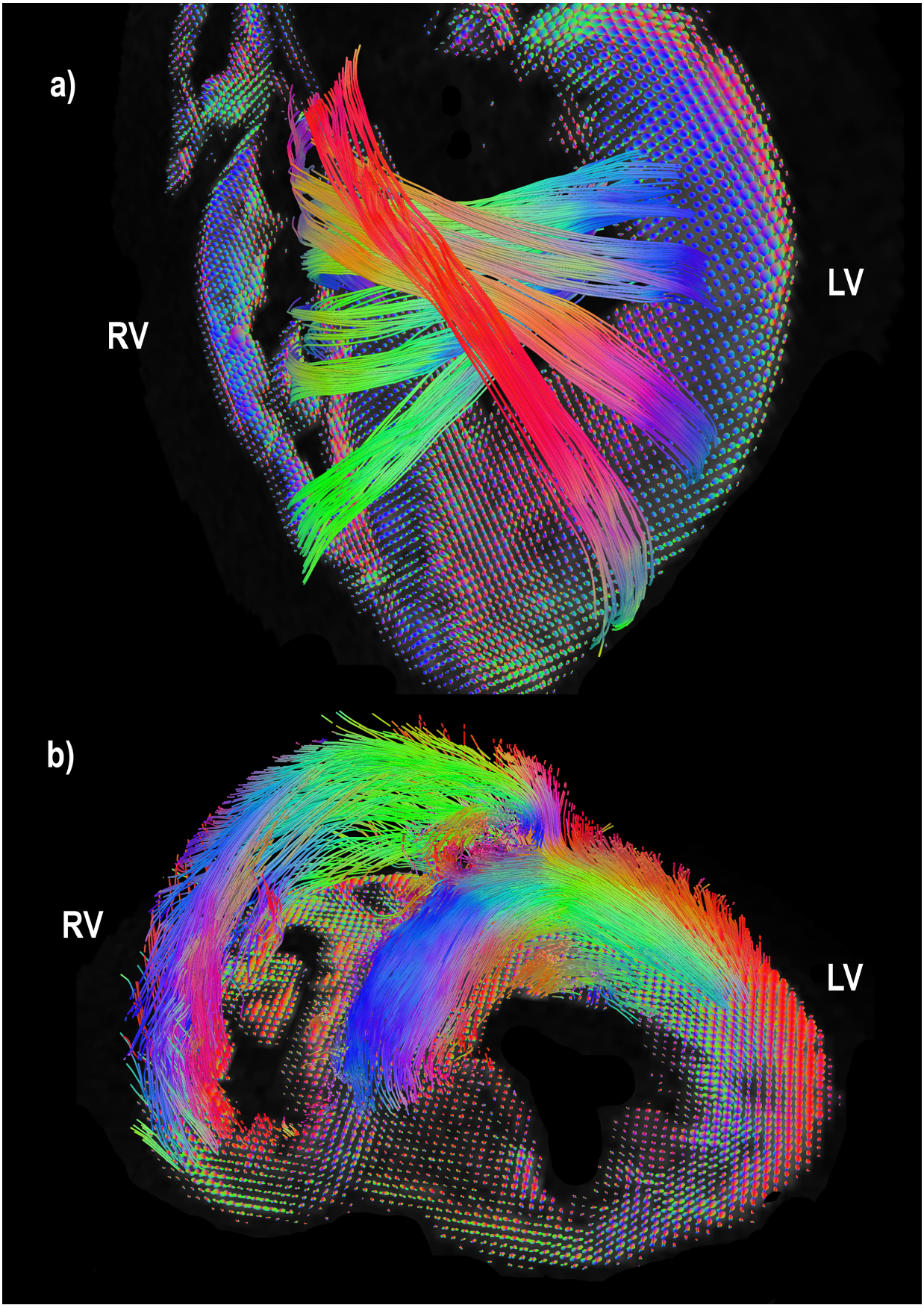

Figure 10.23: Results of QBI-based tractography in an unfixed pig heart. a) Transmural transition of fiber orientations in the myocardium. b) Short axis view of myocardial fibers. Fibers are superimposed onto the local ODFs.

10.4 DWI OF UNFIXED HUMAN TISSUE SPECIMENS

With the experience from imaging of unfixed pig hearts, the next step was to transfer this method to human tissue. For this purpose, the brain and heart of a donated body were explanted and imaged as described in chapter 9.3 and 10.3.

10.4.1 *Human Brain*

The raw images of the human brain showed strong diffusion contrast at a b-value of $5000\,\mathrm{s/mm^2}$. Using the Panini coil, very detailed images at a spatial resolution of 0.9 mm with high SNR values were acquired (cf. Fig. 10.24). In both images, a large hyperintense area can be observed. Hyperintensity in T_2 and diffusion-weighted images can be an indicator for stroke. However, according to the available patient data, no recent or acute stroke was diagnosed. Another possible explanation may be postmortem damage to the brain during explantation although this is more likely to occur on the brain surface.

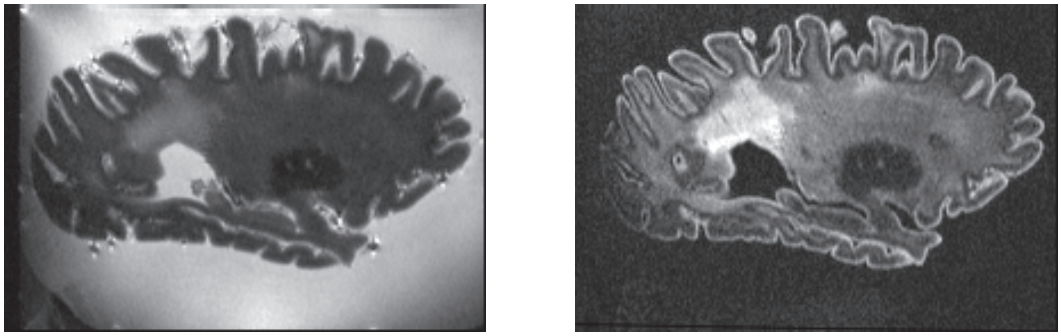

(a) Reference image at $b = 0\,\mathrm{s/mm^2}$.

(b) DWI image at $b = 5000\,\mathrm{s/mm^2}$.

Figure 10.24: Raw images in sagittal view of the unfixed human brain acquired 12 hours post mortem.

Results of mapping T_1 and T_2 in the unfixed human brain are shown in Fig. 10.25. The measured mean relaxation times of $T_1 \approx 800\,\mathrm{ms}$ and $T_2 \approx 100\,\mathrm{ms}$ are significantly higher than those found in the fixed tissue (cf. Fig. 10.4) and agree well with reported in vivo values at 3 T [76]. This supports the hypothesis that unfixed postmortem tissue specimens can serve as an imaging model with high similarity to in vivo conditions.

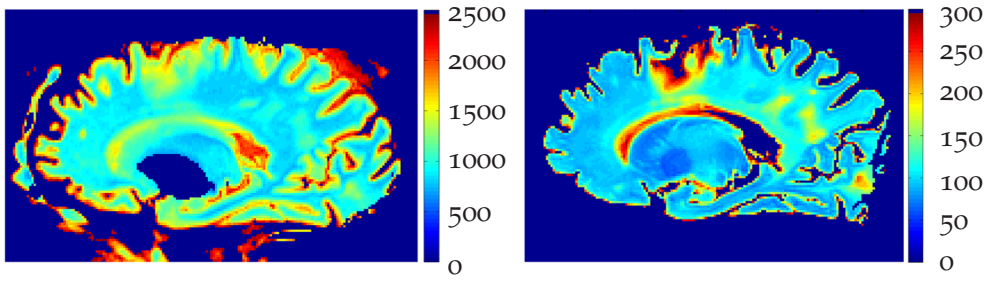

Figure 10.25: T_1 and T_2 maps of the unfixed human brain acquired 12 h post mortem.

As only 40 diffusion directions were sampled with the Panini coil, only a tensor-based reconstruction of fiber pathways was possible. The unfiltered result of DTI-based fiber-tracking in the unfixed human brain hemisphere is shown in Fig. 10.26. Large coherent fiber bundles can be identified in the center of the specimen, especially in the anterior-posterior (A-P) direction. Additionally, fine structures and short association u-fibers can be observed in the outer brain regions.

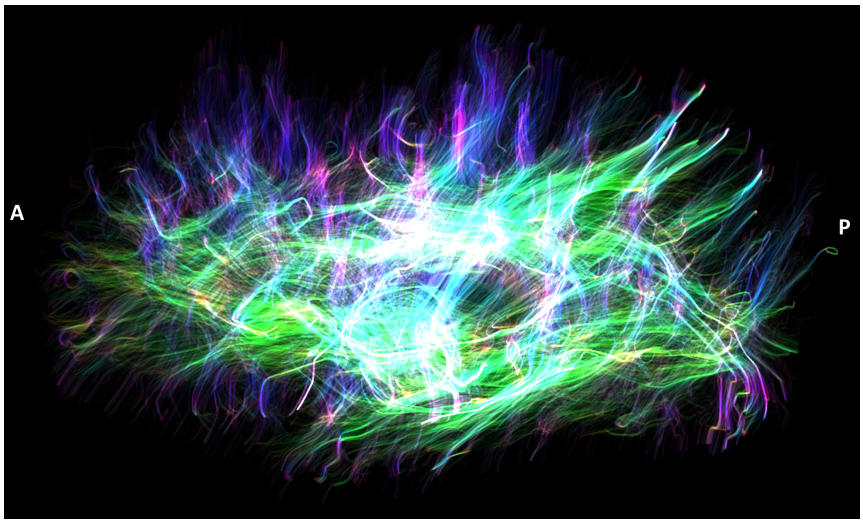

Figure 10.26: Sagittal view of the results of DTI tractography of an unfixed human brain hemisphere. A total of 40 diffusion encoding directions at a b-value of 5000 s/mm^2 were used to estimate the diffusion tensor. Fibers are rendered with 80 % opacity to improve the visibility of large coherent fiber bundles.

In order to compare the tractography results with the HCP and fixed tissue data, the same major white matter fiber pathways were isolated and reconstructed (cf. Fig. 10.27). Although fiber-crossings can not be resolved using DTI, all major tracts were reconstructed accurately. During manual tract filtering, a lower amount of noisy ODFs and spurious fibers was noticed in comparison to the fixed tissue data.

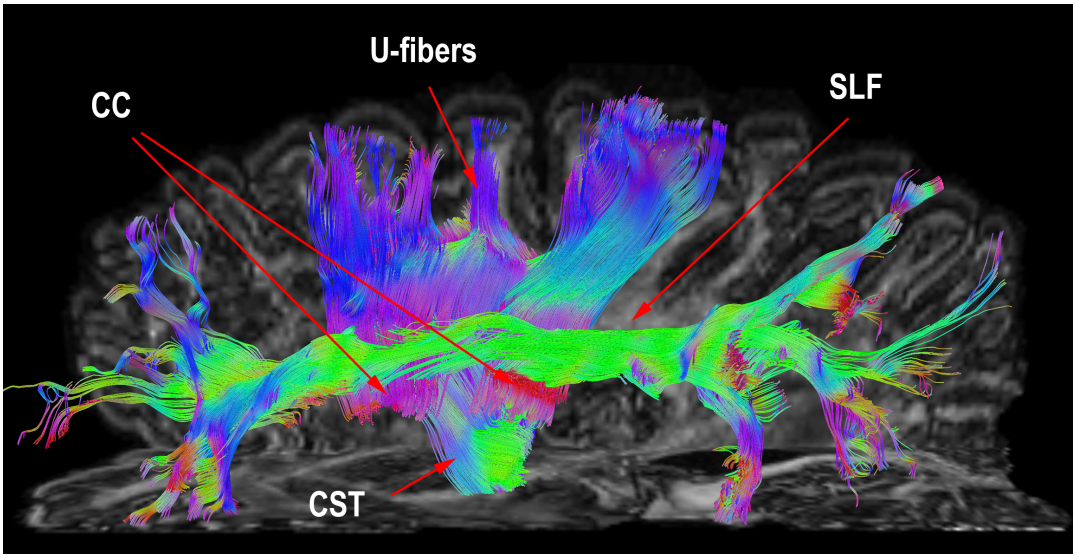

Figure 10.27: Sagittal view of reconstructed fiber pathways of the corpus callosum (CC), superior longitudinal fasciculus (SLF) and corticospinal tract (CST) in the unfixed human brain.

In order to quantify and evaluate the suitability of unfixed post mortem tissue specimens for DWI and tractography, specific diffusion metrics have to be compared between the available data sets. Fractional anisotropy as the most important DTI index was compared between different regions in all three data sets (cf. Tab. 10.3).

Comparison of FA values was based on tracking results from a seeding region in the target tract. The mean FA of all three samples was calculated from 20 000 tracts which were generated from random seed points throughout the samples. Data for fixed tissue was taken from the whole hemisphere at 500 µm resolution because its sample volume is similar to the other data sets.

Analysis of fractional anisotropy confirms the previously mentioned similarity between unfixed postmortem and in vivo tissue. Mean FA values in all three fiber tracts as well as the whole sample agree well within their respective confidence intervals. Fractional anisotropy in the fixed tissue was more than three times lower compared to unfixed tissue which demonstrates the impact of fixation on the diffusion properties of the tissue.

FA	total	SLF	CST	CC
in vivo	0.352 ± 0.109	0.359 ± 0.089	0.347 ± 0.097	0.412 ± 0.112
ex vivo (unfixed)	0.329 ± 0.112	0.386 ± 0.105	0.379 ± 0.110	0.363 ± 0.143
ex vivo (fixed)	0.090 ± 0.039	0.100 ± 0.038	0.092 ± 0.037	0.111 ± 0.054

Table 10.3: Comparison of mean FA values in the human brain between in vivo (1.5 mm), fixed ex vivo (500 µm) and unfixed ex vivo (900 µm) acquisitions. Values are given for the superior longitudinal fasciculus (SLF), corticospinal tract (CST), corpus callosum (CC) and the whole sample volume.

Additional data of the brain, acquired with a four channel Flex coil and the spine array of the patient table, provided 140 diffusion directions. Although these images showed lower SNR values than those from the Panini coil, they allowed for the calculation of a SH energy spectrum (cf. Fig. 10.28). Images from the Panini coil that were compromised by artifacts were also included in the comparison to investigate the impact of these artifacts on the ODF reconstruction.

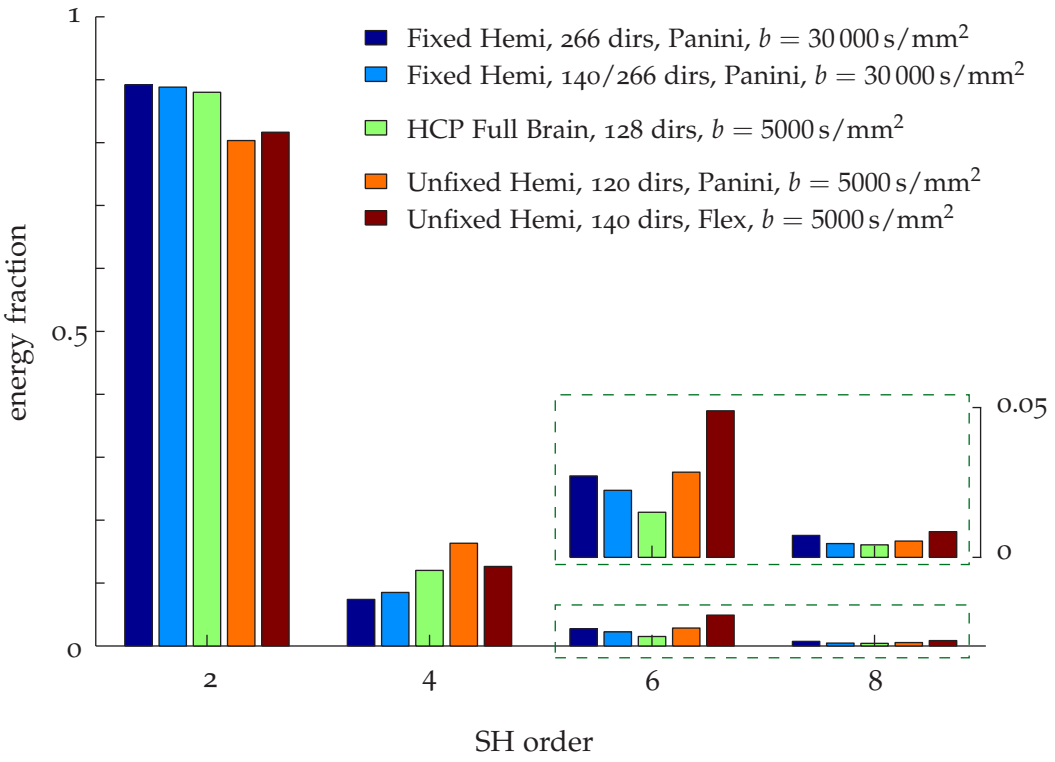

Figure 10.28: Energy spectrum of averaged spherical harmonic (SH) coefficients in diffusion data from fixed and unfixed human hemispheres.

When compared with fixed tissue data, both data sets of unfixed tissue show lower energy fractions in the second SH order but higher energies in the fourth and sixth order. This result is consistent with the observed higher diffusion contrast which results in the detection of finer surface features in the ODF. Thus, unfixed tissue yields higher angular resolution.

All four data sets show similar low energies in SH orders six and eight. However, when evaluating these numbers, one should consider the relatively low number of sampled diffusion directions. In order to determine these high-order SH coefficients with sufficient confidence, more diffusion directions are usually desirable. The exact dependency between the number of diffusion samples, SNR and optimal SH order is still a topic of current research ([19]).

10.4.2 *Human Heart*

In contrast to the brain, the unfixed heart unexpectedly showed very low SNR values, especially towards the center of the coil volume (cf. Fig. 10.29). Furthermore, the heart exceeded the active coil volume in lateral direction which lead to SNR losses in the large blood vessels. Diffusion-weighted images showed decent diffusion contrast in the septal and apical myocardium but barely any signal towards the atria and larger blood vessels.

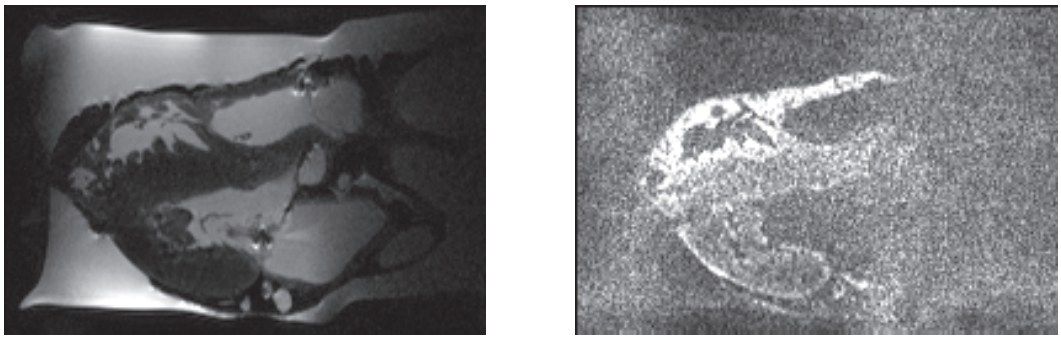

(a) Reference image at $b = 0\,\mathrm{s/mm^2}$.

(b) DWI image at $b = 2000\,\mathrm{s/mm^2}$.

Figure 10.29: Raw images of the unfixed human heart acquired 19 hours post mortem.

T_1 and T_2 maps of the human heart were acquired 19 h post mortem (cf. Fig. 10.30). The average relaxation times in a region of interest are given in table 10.4 along with those of the unfixed pig heart. A comparison with reported in vivo values is difficult as relaxation times are very sensitive to temperature.

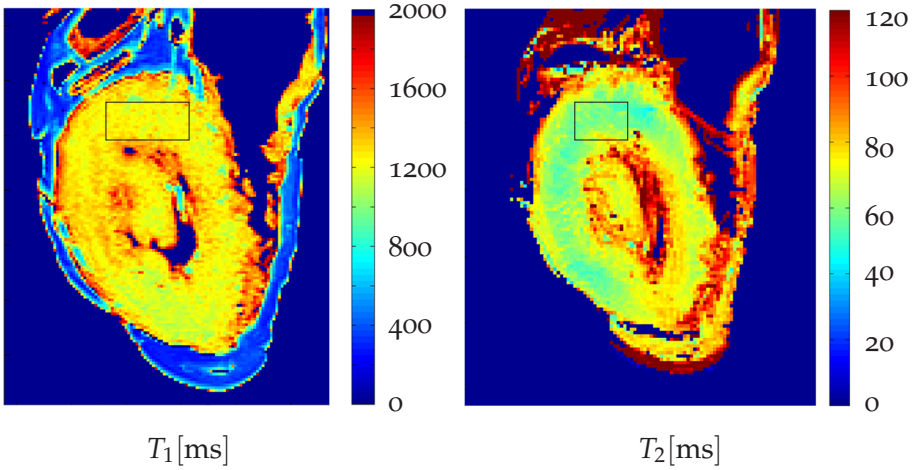

Figure 10.30: T_1 and T_2 maps of the unfixed human heart acquired 19 h post mortem.

Reconstruction of the ODFs revealed better results than anticipated from the raw images. Figure 10.31 shows the results of deterministic tractography performed on the data of 140 sampled diffusion directions. Because of the low SNR and FA values,

	temperature [°C]	T_1 [ms]	T_2 [ms]
pig heart (ex vivo)	22	1240.6 ± 52.1	82.1 ± 5.7
human heart (ex vivo)	22	1177.6 ± 50.8	57.9 ± 3.5
human heart (in vivo)	37	982.0 ± 46.0	52.2 ± 3.4

Table 10.4: T_1 and T_2 postmortem relaxation times in the unfixed human and pig heart. Literature values for human in vivo T_1 and T_2 values are taken from [51] and [26], respectively.

a high number of noisy fibers are present. However, it was still possible to isolate some detailed structures like the two coronary arteries shown in Fig. 10.31 a.

Fibers in the short axis view show the expected helical fiber architecture. A transmural transition of fiber orientations in the myocardium can be seen which is very similar to that observed in pig hearts (cf. Fig. 10.23). The aorta and other blood vessels are only partially reconstructed and required intensive manual seeding and filtering.

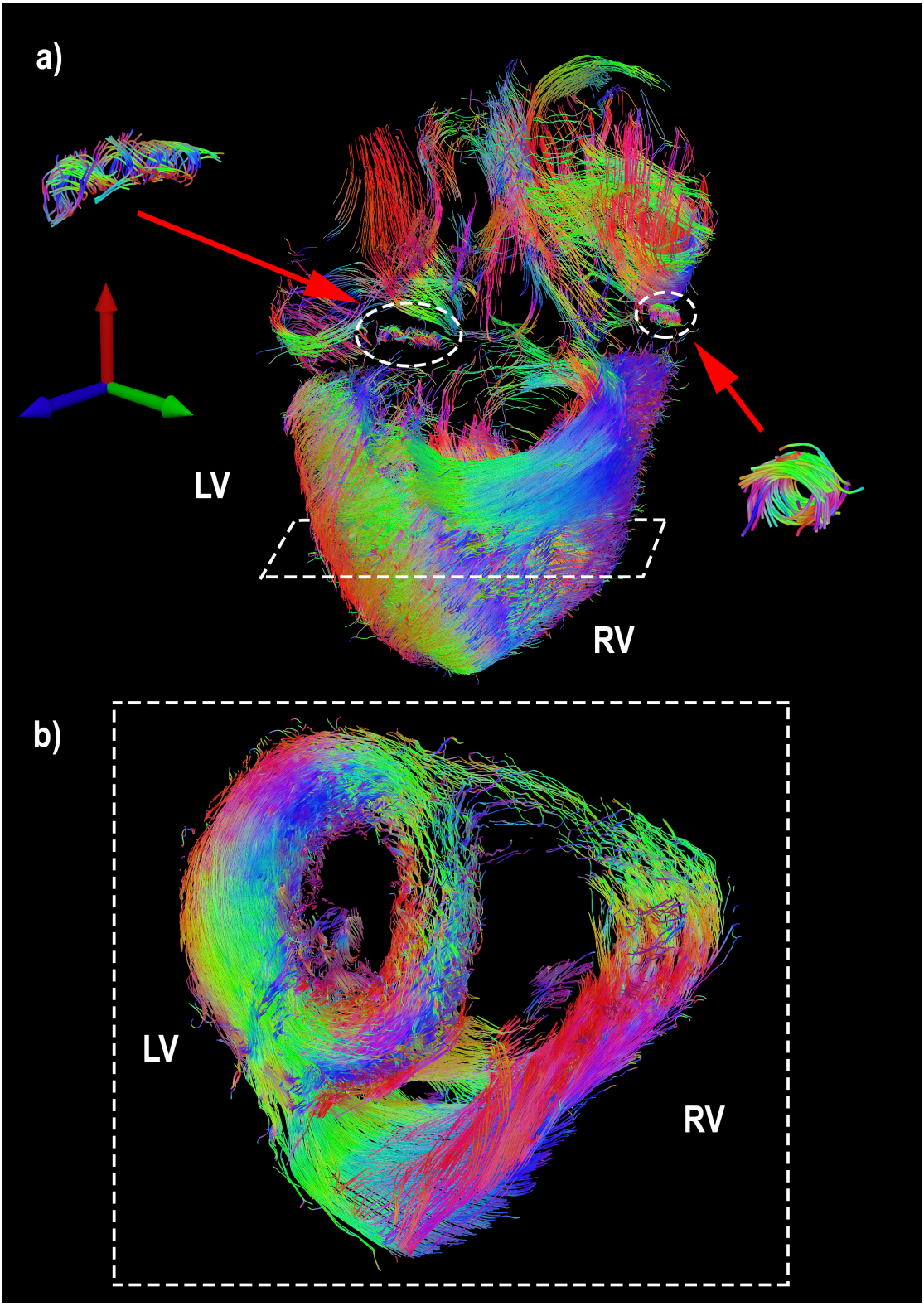

Figure 10.31: Results of DTI-based tractography in the unfixed human heart: a) unfiltered fiber reconstruction of the whole heart volume. Partial reconstructions of the left and right coronary arteries were identified (see enlarged sections). b) Short axis view of myocardial fibers. Very low SNR in the center of the setup leads to incomplete reconstruction of the right ventricle (RV).

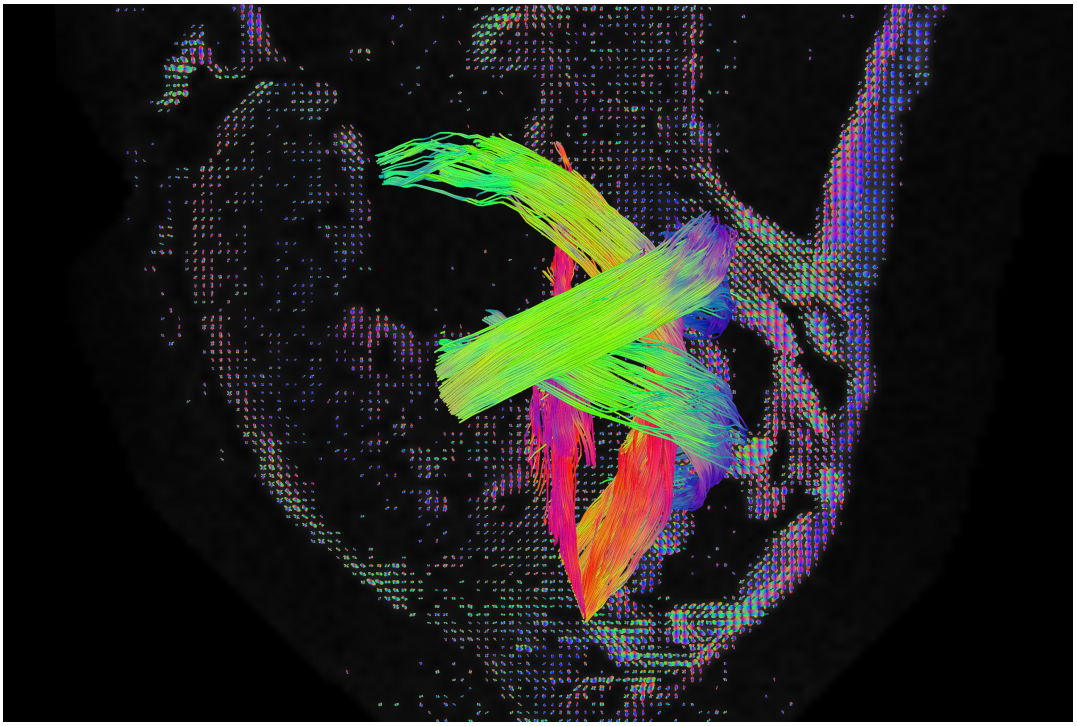

Figure 10.32: Results of QBI-based tractography in the unfixed human heart. Selected fiber tracts are shown to visualize the transmural transition of fiber directions in the myocardum. Fibers are superimposed onto the local ODFs.

11

DISCUSSION

11.1 DWI OF FIXED HUMAN TISSUE SPECIMENS

The results of the Panini project showed impressive isotropic spatial resolutions of up to 350 µm. This resolution was achieved by using a highly optimized 60 channel receive coil array together with the 300 $\mathrm{mT\,m^{-1}}$ gradient system of the MGH-UCLA Magnetom Connectom MRI system. Associated challenges such as inhomogeneous SNR profiles, eddy current distortions and severe ghosting artifacts were successfully compensated or minimized. The goal of this project was to resolve smaller and more complex fiber architectures compared to those identified in in vivo acquisitions. Major white matter fiber tracts were reconstructed accurately. Also, reconstruction of finer features such as short association fibers and fiber crossings in the centrum semiovale was possible, benefiting from the high density of ODFs.

However, both fixed specimens showed very significant isotropic diffusion compartments as a result of the tissue fixation using Formalin or Fomblin. This can be seen in the uniform residual signal despite very strong diffusion attenuation using a b-value of 30 000 $\mathrm{s/mm^2}$. These unusually high b-values were necessary to induce sufficient diffusion weighting to detect multiple maxima in the water displacement distributions. In this regime, diffusion is not purely Gaussian but has to be modeled as a multi-compartment system with different diffusion coefficients. Low SNR values at 350 µm resolution added substantial noise to the field of reconstructed ODFs which reduced the achievable angular resolution. It is worth mentioning that the performance of the eddy current correction algorithm also suffers from low SNR values. Residual image distortions can then lead to false fiber reconstructions.

Most software solutions for tractography use FA (or GFA) thresholds to distinguish between anisotropic fiber ODFs and isotropic noise ODFs. The latter are ignored in the tracking algorithm to avoid reconstruction of unlikely pathways through noise regions. However, ex vivo diffusion anisotropy values were more than three times smaller than in vivo values. This makes an isolation of the target volumes and tracts based on threshold less efficient. As a consequence, only pathways with high diffusion anisotropy were identified which are also present in in vivo data sets. This severely compromised the ability of ex vivo DWI of fixed tissue to discover and identify new complex fiber pathways.

Analysis of the spherical harmonic energy spectrum in the fixed human hemisphere showed decreasing energy contributions with increasing order of the expansion. The calculated mean energies of the whole fixed hemisphere agree well with a recently published in vivo study by Fan et al. where the impact of the

b-value and the number of sampled diffusion directions on the energy spectrum was analyzed [23]. Energy fractions in higher SH orders appear to be very similar in fixed and living tissue. However, with a b-value of 30 000 s/mm^2 and 260 diffusion directions, significant improvements compared to in vivo acquisitions were expected in the fixed tissue. This result shows that the anticipated advantages of ex vivo DWI are at least partially offset by the tissue fixation as it drastically reduces diffusion anisotropy. This conclusion is further supported by the fact that random sub-sampling from 266 to 140 diffusion directions only had a negligible effect on the SH energy spectrum of the fixed hemisphere. It appears reasonable to conclude that another limitation for the achievable angular resolution was already reached at or below 140 directions.

11.2 DWI OF UNFIXED ANIMAL TISSUE SPECIMENS

These findings motivated the use of fresh, unfixed tissue for diffusion-weighted imaging. The idea was to elegantly combine the high signal intensity and diffusion contrast of in vivo acquisitions with the advantages of ex vivo imaging, i.e. long acquisition times and the absence of motion artifacts.

Experiments on fresh pig hearts confirmed the expected improvement in signal intensity and diffusion contrast. Also, a time window of several hours was determined in which the unfixed heart remained in a structurally stable state. Relaxation parameters and the heart's shape stayed almost constant after an initial settling period of about 4 hours. These findings agree with observations in rats published in [36] where T_1 and T_2 were monitored over 24 hours. The fact, that a structurally stable state exists for several hours, allows acquisition of many image volumes without causing misalignment. Although all pig hearts used in this thesis were explanted from reanimated pigs, no structural alterations or injuries of the tissue were noticed.

The averaged data of 19 DTI acquisitions over almost 12 h showed an impressive level of detail in the unfixed pig heart. The high data quality even allowed for the reconstruction of vessels walls in the aorta, pulmonary trunk and right coronary artery (cf. Fig. 10.18). Additionally, the transmural transition of fiber orientations in the myocardium was accurately reconstructed and agrees well with reported structures in the rat and human heart [65, 43]. The "layered" helical structure of myocardial fibers is essential for the heart's function as it allows contraction and torsion of the ventricles.

Furthermore, a 266 direction QBI data set at 0.9 mm resolution was acquired within 4 h. QBI reconstruction yielded similar fiber pathways as DTI. This is a consequence of the heart's tissue structure where mainly single-fiber voxel populations without crossings are present. This was verified in the SH energy spectrum which showed over 97 % of the total energy in second order SH terms. Under

these conditions, DTI performs very well and is capable of accurately mapping the fiber orientations. Consequently, q-ball imaging does not provide substantially better tractography results. It shall be noted that the helical fiber transition in the myocardium can lead to "false" detections of crossing fibers when spatial resolution is low (cf. Fig. 10.21).

11.3 DWI OF UNFIXED HUMAN TISSUE SPECIMENS

Based on the successful experiments using unfixed pig hearts, the feasibility of applying the proposed method to unfixed human tissue specimens was evaluated. For this purpose, the heart and brain of a body donation were explanted and imaged using the previously established experimental setup.

Images of the unfixed human brain were acquired 12 hours post mortem. At this time, the brain still showed very strong diffusion contrast and high SNR at a b-value of $5.000\,\mathrm{s/mm^2}$. At this b-value, the minimum echo time was 97 ms on a commercially available MRI system, namely the Siemens Magnetom Prisma. Considering temperature effects, the measured relaxation times agree with reported in vivo values which illustrates the strong similarity between the ex vivo model and living tissue. Image quality could have been further improved by using the 3D DW-EPI pulse sequence that was developed for the Panini project but was not available in Mainz due to license restrictions.

Comparison of FA values in all three imaging environments of the human brain (in vivo, fixed ex vivo and unfixed ex vivo) confirmed the anticipated improvement in diffusion contrast using unfixed tissue. Note that the reported mean FA values may be slightly biased by the size and shape of the brain specimens. Evaluation of mean spherical harmonic energy spectra in all three brain data sets showed a significant tendency towards higher orders in the unfixed brain. This is a very important result as it demonstrates the detection of finer features in the ODF surfaces of the entire data set which is equivalent to a higher angular resolution. Energy fractions in the eighth order of the SH expansion are equally low in all data sets which raises the question whether a maximum order of six may be sufficient for most QBI acquisitions. At the same time, the number of sampled diffusion directions may be too low to reliably determine these energy fractions. Especially for the unfixed human brain, a second experiment with 266 diffusion directions is highly desirable to compare the achievable angular resolution with the fixed tissue results.

In contrast to the unfixed human brain, the heart showed surprisingly low signal intensities. A possible explanation is the T_2 relaxation time which was found to be significantly shorter compared to the pig heart (60 ms vs. 80 ms). However, this value agrees with reported in vivo values [26]. Reconstruction of myocardial fibers was possible but showed increasingly noisy ODFs towards the center of the active

coil volume. Fiber tracts also showed parts of two coronary arteries and some larger vessel walls. Unfortunately, only fractions of the aorta and pulmonary artery could be reconstructed. This may be due to the fact that the volume of the heart was larger than anticipated and exceeded the active coil volume. Other factors influencing the tissue properties may be age and the known history of cardiomyopathy in this patient. In order to better evaluate the quality of fiber reconstructions, a comparison of the presented results with a healthy human heart from a younger donor would be desirable.

11.4 LIMITATIONS

One major disadvantage of avoiding tissue fixation is the degradation of the specimen. Although it was shown in chapter 10.3 that degradation during image acquisition can be neglected for fresh samples, all specimens had to be disposed of after the experiments. Depending on the actual acquisition time, all specimens developed a distinctive smell and pressurized the sample container. It may be interesting for future studies to investigate whether these samples could still be fixed and stored for further experiments. Formation of gas bubbles was only observed in one pig heart after over 60 hours of storage at room temperature. Because of the long echo times and inherent T_2-weighting in DWI acquisitions, the susceptibility artifacts rendered this pig heart useless for further investigation.

For human body donations, official procedures impose a lower limit of about 6 hours post mortem on the beginning of any research experiments. At the University Medical Center in Mainz about 50 body donations are received per year from over 200 hospitals. On average, only 2 donations come from the medical center in Mainz where the 6 hours mentioned above can be realized. The vast majority of bodies reaches Mainz after more than 20 hours post mortem which is too long to perform DWI experiments without fixation for another 12 to 24 hours. As a consequence only one donor in 5 months fulfilled the inclusion criteria for this thesis.

Section 4.2.3 of the theory chapter covered the impact of Rician noise on magnitude MR images and the bias introduced thereby. The experiments presented in this thesis aimed for high spatial resolution and strong diffusion contrast to resolve complex tissue microstructures. While b_0 images usually show high signal intensities and SNR, the diffusion-weighted images approached SNR levels that are barely sufficient for ODF reconstruction (cf. Fig. 10.5 b). Consequently, those images are well in the SNR regions where the Rician noise distribution has to be considered. Figures 11.1 and 11.2 show the impact of Rician noise on the reconstruction of diffusion ODFs from noisy image data.

In the case of isotropic diffusion, the signal intensity shows no dependency on the direction of the applied gradient. As a consequence, all measurements are

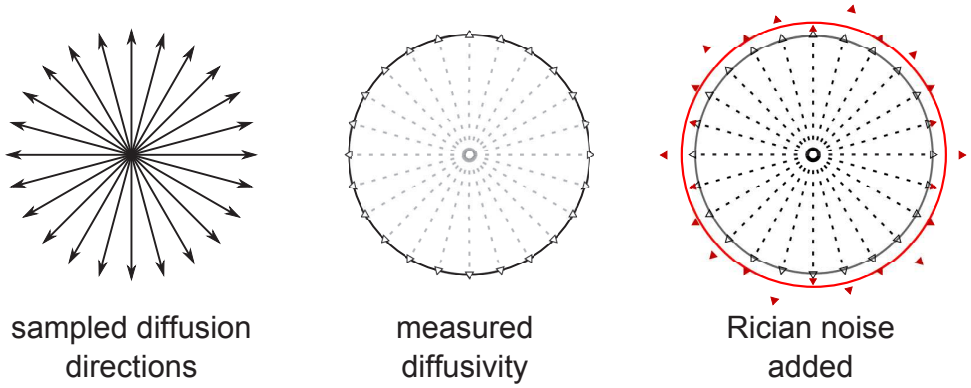

Figure 11.1: Impact of Rician noise on the estimation of orientation distribution functions in the case of isotropic diffusion. The black solid circle represents the true ODF without noise, the red circle shows the observed distribution.

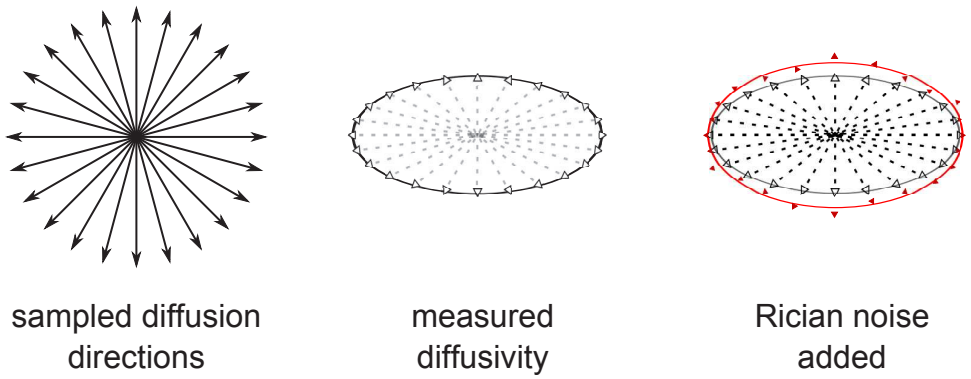

Figure 11.2: Impact of Rician noise on the estimation of orientation distribution functions in the case of restricted diffusion. The black solid ellipse represents the true ODF without noise, the red circle shows the observed distribution where FA is under-estimated.

influenced by random non-zero mean noise which leads to an over-estimation of the ODF volume. The shape of the ODF is not influenced.

For anisotropically restricted diffusion, however, the signal intensity is modulated by the underlying microstructure and depends on the direction of the applied diffusion gradient. Therefore, directions with high diffusion attenuation will be influenced by the Rician noise distribution and their SNR will be over-estimated. During ODF reconstruction, this effect leads to an under-estimation of the fractional anisotropy as shown in Fig. 11.2. As a consequence, the ability to resolve crossing fibers may be limited in data sets with high b-values and thus, low SNR.

This problem has been addressed in the literature and several approaches to compensate Rician noise in low-SNR diffusion data have been proposed [8]. Future studies in this field may benefit from implementing an additional correction for Rician noise into their post-processing pipeline.

Part IV

CONCLUSION AND OUTLOOK

12

CONCLUSION

The experiments presented in this thesis were designed to study diffusion processes in the human body in two different environments. While the diffusion of contrast agent molecules in the blood stream can be modeled as mainly isotropic, water molecules in muscle fibers and neurons show highly anisotropic diffusion patterns. In the course of this thesis the impact of both, the size of the diffusing particle itself and its microscopic environment, on the observed diffusion characteristics were investigated.

The influence of structural reconfiguration on the diffusional behavior of paramagnetic MRI contrast agent chelates was studied. Substitution of the paramagnetic Gd^{3+} ion in Gd-DOTA with Ga^{3+} allowed for direct observation of the complex by means of ^1H NMR spectroscopy and enabled direct diffusion measurements. The diffusion coefficient of Ga-DOTA in D_2O at 310 K was measured to be

$$D_{\mathrm{Ga-DOTA}}(310\,\mathrm{K}, \mathrm{D_2O}) = (4.38 \pm 0.04) \times 10^{-10}\,\mathrm{m^2/s} \tag{12.1}$$

The validity of assuming similar diffusional behavior of Gd-DOTA and Ga-DOTA depends on the similarity of their respective hydrodynamic radii. These were investigated using dielectric relaxation spectroscopy and agree well within their respective confidence intervals. This provides evidence that both complexes are indeed very similar in their hydrodynamic properties. Therefore, the above diffusion coefficient of Ga-DOTA is also valid for the MRI contrast agent Gd-DOTA.

An estimate for the diffusivity of both complexes in human blood plasma was calculated by correcting the above results for the higher viscosity of blood:

$$D_{\mathrm{Ga/Gd-DOTA}}(310\,\mathrm{K}, \mathrm{plasma}) = (2.92 \pm 0.25) \times 10^{-10}\,\mathrm{m^2/s} \tag{12.2}$$

This estimate agrees with a previously reported value for the diffusion of Gd-DOTA in necrotic tumor regions. However, the agreement is mainly due to the high uncertainty of the literature value and should be evaluated with caution. The evident tendency towards faster diffusion in blood plasma, compared to necrotic tumor tissue appear reasonable.

In the second part of this thesis anisotropic diffusion in the presence of boundaries for water displacement was studied. Neuron pathways in the brain and muscle fibers in the heart served as models for fibrous tissue.

Starting with the Panini project, the advantages and limitations of diffusion-weighted imaging of fixed postmortem tissue specimens were investigated. The goal of this research project was to increase spatial and angular resolution in neuron fiber reconstructions to further our understanding of the complex neuron network in the human brain.

Using a highly optimized experimental setup, an unprecedented spatial resolution of 350 µm was achieved on a 3 T full-bore human MRI system. Fiber reconstructions at this resolution showed impressively detailed structures as a result of the 79-fold higher ODF density compared to typical in vivo acquisitions. However, analysis of diffusion contrast based on spherical harmonic decomposition revealed little to no benefit in terms of angular resolution. As a consequence, the ability to resolve and possibly discover new microstructures in the postmortem human brain was severely limited.

Application of the proposed method to fixed and unfixed pig hearts identified tissue fixation as the major limitation for SNR and diffusion contrast in ex vivo DWI. Images of the unfixed heart showed significantly higher SNR values and stronger diffusion contrast compared to fixed tissue. Also, a structurally stable state in the unfixed postmortem heart was found which allowed continuous imaging over 13 h. The helical structure of myocardial fiber bands was accurately reconstructed as were the vessel walls of the aorta, pulmonary trunk and right coronary artery. Judging from the presented results, the diffusion tensor model is capable of mapping the correct fiber orientations in the myocardium as no fiber crossings are present. Therefore, the number of sampled diffusion directions and acquisition times can be reduced significantly.

In a following pilot study, the feasibility of DWI and tractography using unfixed human tissue was investigated. In the human brain, major white matter pathways were successfully reconstructed at 0.9 mm isotropic resolution. Although only 60 diffusion directions were sampled, similar results compared to the Panini data were achieved in 1.5 h. Fiber reconstructions in the unfixed human heart suffered from low SNR values due to shorter T_2 times. Using a larger coil and lower b-value, the quality of tract reconstructions is likely to improve significantly in future studies.

The presented results demonstrate the feasibility of DWI and tractography using unfixed human and animal tissue specimens. Analysis of fractional anisotropy and spherical harmonic energy spectra verified the significantly improved angular resolution compared to fixed tissue. At the same time, the higher water content and longer relaxation times in unfixed tissue yield higher SNR values and bear the potential of further increasing image resolution.

In conclusion, the use of unfixed, fresh tissue provided better data quality at significantly lower b-values and echo times. This enables the proposed method to be implemented on standard clinical MRI systems, making it accessible for the whole MRI community.

13

OUTLOOK

At the current state both projects were pursued to a point that answered the respective questions which they were motivated by. During the course of this thesis many new questions emerged from unexpected challenges and sometimes even changed the focus of the following investigations.

In the case of diffusion tractography, ex vivo imaging is often used to obtain high-resolution images with little to now artifacts, especially in regions that are not easily accessible in vivo. But at the same time, tissue fixation imposes strong limitations on the achievable data quality. The results of this thesis suggest that the use of unfixed, fresh tissue specimens can help to significantly improve the quality of ex vivo diffusion data. Acquisition windows of several hours allow sampling of very high numbers of diffusion directions at high spatial resolution. In the pursuit of pushing the limits of spatial and angular resolution in diffusion tractography, the results of this thesis may provide a valuable strategy to further advance our ability to investigate complex neuron microstructures in the human brain.

Clinical applications may also benefit from the proposed method by using high-resolution ex vivo data as training references for adaptive dictionaries in compressed sensing reconstructions of in vivo data [11]. Another fascinating research field which may benefit from this methodology is neuroplasticity [71]. It is well known that the neuronal routing between brain regions changes with behavior or disease. In stroke patients, other brain regions are sometimes able to adapt the functionality of tissue that was lost. It is also known from psychology that certain disorders, e.g. depression and schizophrenia, correlate with abnormal fiber structures [78, 46]. DWI and tractography of unfixed postmortem tissue provides the ability to identify and study these structural changes at significantly higher spatial and possibly angular resolutions. On a larger timescale one can envision the development of "forensic MR imaging" as a new discipline to non-invasively assess the integrity of tissue structure in postmortem bodies.

Applications of the chelating agent DOTA are not limited to the field of MRI. As a carrier for radio-isotopes like ^{69}Ga and other drugs, DOTA and its derivatives serve as very versatile tools for the treatment and diagnosis of various diseases. This widespread field of in vivo applications underlines the importance to better understand the exact mechanisms of how these agents are distributed in the human body. The reported diffusion coefficients of Ga- and Gd-DOTA may have a direct impact on current research efforts in the field of computational fluid dynamics. They may also serve as valuable references for other DOTA derivatives.

Direct measurement of the diffusivity in human blood plasma could provide an important validation of the presented estimate. Because of the strong ^{1}H NMR signal background of blood this experiment could not be performed within the time frame of this thesis. However, a direct measurement may become feasible by using NMR-detectable metal ions or isotopic labeling of the compound.

A

APPENDIX

LIST OF FIGURES

Figure 2.1 Brownian motion 5
Figure 2.2 Gaussian diffusion derived by Pascal's triangle 6

Figure 3.1 NMR FID and resulting Fourier peak. 13
Figure 3.2 ^{1}H NMR spectrum and structure of ethanol. 14
Figure 3.3 NMR signal attenuation by Gaussian diffusion 15
Figure 3.4 Calculation of b from sequence parameters. 17

Figure 4.1 MRI slice encoding. 19
Figure 4.2 Fourier relation between pulse shape and slice profile. 20
Figure 4.3 MRI phase encoding 21
Figure 4.4 MRI frequency encoding. 21
Figure 4.5 Concept of k-space. 22
Figure 4.6 Schematic representation of a 2D EPI sequence. 23
Figure 4.7 Accelerated k-space sampling. 23
Figure 4.8 Schematic representation of a 2D multi-shot DW-EPI sequence. 25
Figure 4.9 Restricted diffusion. 26
Figure 4.10 Rician noise distribution 27
Figure 4.11 Gd-DOTA structure. 28

Figure 5.1 Diffusion tensor visualization. 30
Figure 5.2 DTI limitations. 30
Figure 5.3 PDF and ODF reconstruction. 31
Figure 5.4 Angular resolution in QBI as a function of harmonic order L. . 33
Figure 5.5 Illustration of fiber-tracking algorithms. 35

Figure 7.1 Structure and ^{1}H NMR spectrum of pure DOTA in D_2O. 45
Figure 7.2 ^{1}H NMR spectra of all metal-DOTA solutions. 46
Figure 7.3 ^{1}H NMR spectra of Ga-DOTA and pure DOTA in D_2O. 47
Figure 7.4 Temperature series of ^{1}H NMR spectra of Ga-DOTA in D_2O. . 48
Figure 7.5 MALDI-TOF mass spectrum of Ga-DOTA. 49
Figure 7.6 2D DOSY NMR spectra of pure DOTA and Ga-DOTA at 310 K. 50
Figure 7.7 DRS spectra of Ga-DOTA and Gd-DOTA. 51

Figure 8.1 Comparison of Ga-DOTA and Gd-DOTA crystal structures. . . 54

Figure 8.2 ^{1}H NMR spectrum of human blood plasma. 56

Figure 9.1 3D render of the two Panini coil layers. 60
Figure 9.2 Photographs of the final Panini coil design. 61
Figure 9.3 Photographs of fixed brain tissue specimens. 62
Figure 9.4 Anatomical localization of the fixed human brain specimens. . 62
Figure 9.5 Schematic representation of the 3D multi-shot DW-EPI sequence. 63
Figure 9.6 Q-Space coverage using 260 evenly spaced vectors. 65
Figure 9.7 Postprocessing pipeline. 66
Figure 9.8 Panini coil sensitivity correction. 68
Figure 9.9 Correction of the Panini coil sensitivity profile: before and after. 68
Figure 9.10 Experimental setup for heart DWI. 71
Figure 9.11 Timeline of experiments performed on the unfixed pig heart. . 72
Figure 9.12 Artifacts in unfixed human brain images. 74

Figure 10.1 Ghosting artifacts in the 3D DW-EPI sequence. 77
Figure 10.2 Manual vs. automatic phase correction. 78
Figure 10.3 Improved ghosting levels in 3D DW-EPI sequence images. . . . 79
Figure 10.4 T_1 and T_2 maps of the fixed human hemisphere. 80
Figure 10.5 DWI images of the two fixed human brain specimens. 81
Figure 10.6 SNR and 1/G factor maps of the Panini coil and a 64 channel head array. 82
Figure 10.7 Comparison of ODF densities in the corpus callosum. 84
Figure 10.8 Unfiltered fiber tracts in the fixed hemisphere. 84
Figure 10.9 Comparison of HCP and Panini image quality. 86
Figure 10.10 Exemplary tract reconstructions in the 350 µm Panini data. . . 87
Figure 10.11 Spherial harmonic energy spectrum fixed hemisphere. 88
Figure 10.12 SH coefficient maps of the fixed human brain. 89
Figure 10.13 Comparison of fixed and fresh pig hearts. 91
Figure 10.14 DWI images of a fresh pig heart. 92
Figure 10.15 Heating of the gradient coil at maximum duty cycle. 93
Figure 10.16 T_1 and T_2 maps of the unfixed pig heart. 94
Figure 10.17 Timeline and results of experiments on the fresh pig heart. . . 95
Figure 10.18 DTI tractography on a fresh pig heart. 96
Figure 10.19 DTI tractography of the right coronary artery. 97
Figure 10.20 Pig heart tractography after 2 weeks in Formalin. 98
Figure 10.21 2D diffusion profiles in the pig's myocardium. 99
Figure 10.22 Spherical harmonic energy spectrum of the unfixed pig heart. . 100
Figure 10.23 QBI tractography of an unfixed pig heart. 101
Figure 10.24 Raw images of the unfixed human brain. 102
Figure 10.25 T_1 and T_2 maps of the unfixed human brain. 103
Figure 10.26 DTI tractography of the whole unfixed human brain. 103
Figure 10.27 DTI tractography in the unfixed human brain. 104
Figure 10.28 Spherial harmonic energy spectrum of the (un)fixed hemisphere. 105

Figure 10.29 Raw images of the unfixed human heart. 106
Figure 10.30 T_1 and T_2 maps of the unfixed human heart. 106
Figure 10.31 DTI tractography of the unfixed human heart. 108
Figure 10.32 QBI tractography of the unfixed human heart. 109

Figure 11.1 Impact of Rician noise on isotropic ODFs. 115
Figure 11.2 Impact of Rician noise on anisotropic ODFs. 115

LIST OF TABLES

Table 6.1 Periodic table of suitable replacement ions for Gd^{3+} in Gd-DOTA. 40
Table 6.2 List of tested replacement ions for Gd^{3+} in Gd-DOTA. 41

Table 9.1 Acquisition parameters: Fixed human brain specimens. 64
Table 9.2 Acquisition parameters: Fresh vs. fixed pig hearts. 71
Table 9.3 Acquisition parameters: DWI, T_1 and T_2 of unfixed pig heart. . 73
Table 9.4 Acquisition parameters: Unfixed Human Tissue. 75

Table 10.1 Average relaxation times in the fixed human brain. 80
Table 10.2 Minimum echo time vs. gradient amplitude. 83
Table 10.3 FA comparison in living and (un)fixed post mortem tissue. . . 104
Table 10.4 T_1 and T_2 in the unfixed human heart. 107

Table A.1 Siemens MDDW gradient vector table. 127

ACRONYMS

ADC	Apparent Diffusion Coefficient **AND** Analog-to-Digital Converter
CST	Corticospinal Tract
DOTA	1,4,7,10-tetraazacyclododecane-1,4,7,10-tetraacetic acid
DRS	Dielectric Relaxation Spectroscopy
DSI	Diffusion Spectrum Imaging
DTI	Diffusion Tensor Imaging
DOSY	Diffusion-Ordered Spectroscopy
EPI	Echo Planar Imaging
FA	Fractional Anisotropy
FID	Free Induction Decay
FFT	Fast Fourier Transform
FOV	Field of View
GFA	Generalized Fractional Anisotropy
HARDI	High Angular Resolution Diffusion-Weighted Imaging
HCP	Human Connectome Project
ICE	Image Calculation Environment
QA	Quantitative Anisotropy
QBI	Q-Ball Imaging
MDDW	Multi-Direction Diffusion Weighting
MGH	Massachusetts General Hospital
MRI	Magnetic Resonance Imaging
NIH	National Institutes of Health
NMR	Nuclear Magnetic Resonance
ODF	Orientation Distribution Functions
PET	Positron Emission Tomography

PD	Proton Density
PDF	Probability Distribution Function
RF	Radio-Frequency (pulse)
ROI	Region of Interest
SH	Spherical Harmonics
SHD	Spherical Harmonic Decomposition
SNR	Signal-to-Noise Ratio
SSFP	Steady-State Free Precession
TE	Echo Time
TR	Repetition Time

SIEMENS GRADIENT TABLE

vector	components		
	phase	read	slice
1	0.8628	0.3574	−0.3574
2	0.8628	−0.3574	−0.3574
3	0.8628	−0.3574	0.3574
4	0.8628	0.3574	0.3574
5	0.3574	0.3574	0.8628
6	0.3574	0.8628	0.3574
7	0.3574	0.8628	−0.3574
8	0.3574	0.3574	−0.8628
9	0.3574	−0.3574	−0.8628
10	0.3574	−0.8628	−0.3574
11	0.3574	−0.8628	0.3574
12	0.3574	−0.3574	0.8628

Table A.1: Siemens multi-direction diffusion weighting (MDDW) gradient vector table with 12 directions. Values were taken from [1] and normalized to unity.

BIBLIOGRAPHY

[1] Siemens AG. Diffusion imaging, perfusion imaging - application brochure. Munich, Germany, 2009.

[2] C. B. Ahn and Z. H. Cho. A new phase correction method in nmr imaging based on autocorrelation and histogram analysis. *Ieee Transactions on Medical Imaging*, 6(1):32–36, 1987.

[3] S. Aime, M. Botta, and G. Ermondi. Nmr-study of solution structures and dynamics of lanthanide(iii) complexes of dota. *Inorganic Chemistry*, 31(21):4291–4299, 1992.

[4] J. Andersson, J. Xu, E. Yacoub, E. Auerbach, S. Moeller, and K. Ugurbil. A comprehensive gaussian process framework for correcting distortions and movements in diffusion images. *Proc. Int. Soc. Mag. Reson. Med.*, 20:2426, 2012.

[5] Paul D. Bailey, Domenico Zacà, Mahmud Mossa Basha, Shruti Agarwal, Sachin K. Gujar, Haris I. Sair, John Eng, and Jay J. Pillai. Presurgical fmri and dti for the prediction of perioperative motor and language deficits in primary or metastatic brain lesions. *Journal of Neuroimaging*, page tbd (early online view), 2015.

[6] R. H. Barton, D. Waterman, F. W. Bonner, E. Holmes, R. Clarke, J. K. Nicholson, and J. C. Lindon. The influence of edta and citrateanticoagulant addition to human plasma on information recovery from nmr-based metabolic profiling studies. *Molecular BioSystems*, 6(1):215–224, 2010.

[7] P. J. Basser, S. Pajevic, C. Pierpaoli, J. Duda, and A. Aldroubi. In vivo fiber tractography using dt-mri data. *Magnetic Resonance in Medicine*, 44(4):625–632, 2000.

[8] Saurav Basu, Thomas Fletcher, and Ross Whitaker. *Rician Noise Removal in Diffusion Tensor MRI*, volume 4190 of *Lecture Notes in Computer Science*, chapter 15, pages 117–125. Springer Berlin Heidelberg, 2006.

[9] S. Benazeth, J. Purans, M. C. Chalbot, M. K. Nguyen-van Duong, L. Nicolas, F. Keller, and A. Gaudemer. Temperature and ph dependence xafs study of gd(dota)(-) and gd(dtpa)(2-) complexes: Solid state and solution structures. *Inorganic Chemistry*, 37(15):3667–3674, 1998.

[10] M. A. Bernstein, K. F. King, and J. Z. Xiaohong. *Handbook of MRI Pulse Sequences*. Elsevier Academic Press, 2004.

[11] Berkin Bilgic, Kawin Setsompop, Julien Cohen-Adad, Anastasia Yendiki, Lawrence L. Wald, and Elfar Adalsteinsson. Accelerated diffusion spectrum imaging with compressed sensing using adaptive dictionaries. *Magnetic Resonance in Medicine*, 68(6):1747–1754, 2012.

[12] C. E. Bodwell, A. M. Pearson, and Mildred E. Spooner. Post-mortem changes in muscle. i. chemical changes in beef. *Journal of Food Science*, 30(5):766–772, 1965.

[13] R. Brown. A brief account of microscopical observations made in the months of june, july and august, 1827, on the particles contained in the pollen of plants; and on the general existence of active molecules in organic and inorganic bodies. *Edinburgh new Philosophical Journal*, 1(July-September):358–371, 1827.

[14] R. Buchner and G. Hefter. Interactions and dynamics in electrolyte solutions by dielectric spectroscopy. *Physical Chemistry Chemical Physics*, 11(40):8984–8999, 2009.

[15] M. H. Buonocore and L. S. Gao. Ghost artifact reduction for echo planar imaging using image phase correction. *Magnetic Resonance in Medicine*, 38(1):89–100, 1997.

[16] H. Y. Carr. Steady-state free precession in nuclear magnetic resonance. *Physical Review*, 112(5):1693–1701, 1958.

[17] C. H. Cho, J. Urquidi, S. Singh, and G. W. Robinson. Thermal offset viscosities of liquid h20, d20, and t20. *Journal of Physical Chemistry B*, 103(11):1991–1994, 1999.

[18] J. Cohen-Adad, M. Descoteaux, S. Rossignol, R. D. Hoge, R. Deriche, and H. Benali. Detection of multiple pathways in the spinal cord using q-ball imaging. *Neuroimage*, 42(2):739–749, 2008.

[19] M. Descoteaux, E. Angelino, S. Fitzgibbons, and R. Deriche. Regularized, fast, and robust analytical q-ball imaging. *Magnetic Resonance in Medicine*, 58(3):497–510, 2007.

[20] J. F. Desreux. Nuclear magnetic resonance spectroscopy of lanthanide complexes with a tetraacetic tetraaza macrocycle. unusual conformation properties. *Inorganic Chemistry*, 19(5):1319–1324, 1980.

[21] C. Eichner, L. L. Wald, and K. Setsompop. A low power radiofrequency pulse for simultaneous multislice excitation and refocusing. *Magnetic Resonance in Medicine*, 72(4):949–958, 2014.

[22] A. Einstein. Über die von der molekularkinetischen theorie der wärme geforderte bewegung von in ruhenden flüssigkeiten suspendierten teilchen. *Annalen der Physik*, 17:549 ff., 1905.

[23] Qiuyun Fan, Aapo Nummenmaa, Thomas Witzel, Roberta Zanzonico, Boris Keil, Stephen Cauley, Jonathan R. Polimeni, Dylan Tisdall, Koene R. A. Van Dijk, Randy L. Buckner, Van J. Wedeen, Bruce R. Rosen, and Lawrence L. Wald. Investigating the capability to resolve complex white matter structures with high b-value diffusion magnetic resonance imaging on the mgh-usc connectom scanner. *Brain connectivity*, 4(9):718–26, 2014.

[24] T. Feiweier. Magnetic resonance method and apparatus to determine phase correction parameters, 2011.

[25] C. Gaudiano, V. Clementi, F. Busato, B. Corcioni, M. G. Orrei, E. Ferramosca, E. Fabbri, P. Berardi, A. Santoro, and R. Golfieri. Diffusion tensor imaging and tractography of the kidneys: assessment of chronic parenchymal diseases. *European Radiology*, 23(6):1678–1685, 2013.

[26] S. Giri, Y. C. Chung, A. Merchant, G. Mihai, S. Rajagopalan, S. V. Raman, and O. P. Simonetti. T2 quantification for improved detection of myocardial edema. *Journal of Cardiovascular Magnetic Resonance*, 11, 2009.

[27] Maurice Goldman, Haukur Jóhannesson, Oskar Axelsson, and Magnus Karlsson. Hyperpolarization of 13c through order transfer from parahydrogen: A new contrast agent for mri. *Magnetic Resonance Imaging*, 23(2):153–157, 2005.

[28] D. Graafen, K. Munnemann, S. Weber, K. F. Kreitner, and L. M. Schreiber. Quantitative contrast-enhanced myocardial perfusion magnetic resonance imaging: Simulation of bolus dispersion in constricted vessels. *Medical Physics*, 36(7):3099–3106, 2009.

[29] B. Gruber, B. Keil, T. Witzel, A. Nummenmaa, and L. L. Wald. A 60-channel ex-vivo brain-slice coil array for 3t imaging. *Proceedings of the 22nd Annual Meeting of the ISMRM, Milan, Italy*, page #4885, 2014.

[30] H. Gudbjartsson and S. Patz. The rician distribution of noisy mri data. *Magnetic Resonance in Medicine*, 34(6):910–914, 1995.

[31] Daniela Guenther, Balthasar Eberle, Jochem Hast, Jana Lill, Klaus Markstaller, Michael Puderbach, Wolfgang G. Schreiber, Gorden Hanisch, Claus P. Heussel, Reinhard Surkau, Tino Grossmann, Norbert Weiler, Manfred Thelen, and Hans-Ulrich Kauczor. 3he mri in healthy volunteers: preliminary correlation with smoking history and lung volumes. *NMR in Biomedicine*, 13(4):182–189, 2000.

[32] Christopher P. Hess, Pratik Mukherjee, Eric T. Han, Duan Xu, and Daniel B. Vigneron. Q-ball reconstruction of multimodal fiber orientations using the spherical harmonic basis. *Magnetic Resonance in Medicine*, 56(1):104–117, 2006.

[33] Simone Hoeft and Klaus Roth. Struktur und dynamik von lanthanoid-tetraazacyclododecantetraacetat-(dota-)komplexen in lösung. *Chemische Berichte*, 126(4):869–873, 1993.

[34] Susie Y. Huang, Aapo Nummenmaa, Thomas Witzel, Tanguy Duval, Julien Cohen-Adad, Lawrence L. Wald, and Jennifer A. McNab. The impact of gradient strength on in vivo diffusion mri estimates of axon diameter. *Neuroimage*, 106(0):464–472, 2015.

[35] A. Jerschow and N. Muller. Suppression of convection artifacts in stimulated-echo diffusion experiments. double-stimulated-echo experiments. *Journal of Magnetic Resonance*, 125(2):372–375, 1997.

[36] R. L. Kamman, K. G. Go, G. P. Stomp, C. E. Hulstaert, and H. J. Berendsen. Changes of relaxation times t1 and t2 in rat tissues after biopsy and fixation. *Magnetic Resonance Imaging*, 3(3):245–50, 1985.

[37] Michael Karas, Doris Bachmann, and Franz Hillenkamp. Influence of the wavelength in high-irradiance ultraviolet laser desorption mass spectrometry of organic molecules. *Analytical Chemistry*, 57(14):2935–2939, 1985.

[38] H. U. Kauczor, M. Ebert, K. F. Kreitner, H. Nilgens, R. Surkau, W. Heil, D. Hofmann, E. W. Otten, and M. Thelen. Imaging of the lungs using 3he mri: Preliminary clinical experience in 18 patients with and without lung disease. *Jmri-Journal of Magnetic Resonance Imaging*, 7(3):538–543, 1997.

[39] B. Kaya and Z. Koc. Diffusion-weighted mri and optimal b-value for characterization of liver lesions. *Acta Radiologica*, 55(5):532–542, 2014.

[40] Boris Keil, James N. Blau, Stephan Biber, Philipp Hoecht, Veneta Tountcheva, Kawin Setsompop, Christina Triantafyllou, and Lawrence L. Wald. A 64-channel 3t array coil for accelerated brain mri. *Magnetic Resonance in Medicine*, 70(1):248–258, 2013.

[41] G. Kesmarky, P. Kenyeres, M. Rabai, and K. Toth. Plasma viscosity: A forgotten variable. *Clinical Hemorheology and Microcirculation*, 39(1-4):243–246, 2008.

[42] Z. Koc and G. Erbay. Optimal b value in diffusion-weighted imaging for differentiation of abdominal lesions. *Journal of Magnetic Resonance Imaging*, 40(3):559–566, 2014.

[43] Mladen J. Kocica, Antonio F. Corno, Francesc Carreras-Costa, Manel Ballester-Rodes, Mark C. Moghbel, Clotario N.C. Cueva, Vesna Lackovic, Vladimir I. Kanjuh, and Francisco Torrent-Guasp. The helical ventricular myocardial band: global, three-dimensional, functional architecture of the ventricular myocardium. *European Journal of Cardio-Thoracic Surgery*, 29(Supplement 1):S21–S40, 2006.

[44] T. S. Koh, S. Hartono, C. H. Thng, T. K. H. Lim, L. Martarello, and Q. S. Ng. In vivo measurement of gadolinium diffusivity by dynamic contrast-enhanced mri: A preclinical study of human xenografts. *Magnetic Resonance in Medicine*, 69(1):269–276, 2013.

[45] V. Kubicek, J. Havlickova, J. Kotek, T. Gyula, P. Hermann, E. Toth, and I. Lukes. Gallium(iii) complexes of dota and dota-monoamide: Kinetic and thermodynamic studies. *Inorganic Chemistry*, 49(23):10960–10969, 2010.

[46] M. Kubicki, H. Park, C.F. Westin, P.G. Nestor, R.V. Mulkern, S.E. Maier, M. Niznikiewicz, E.E. Connor, J.J. Levitt, M. Frumin, R. Kikinis, F.A. Jolesz, R.W. McCarley, and M.E. Shenton. {DTI} and {MTR} abnormalities in schizophrenia: Analysis of white matter integrity. *NeuroImage*, 26(4):1109 – 1118, 2005.

[47] M. H. Levitt. *Spin Dynamics: Basics of Nuclear Magnetic Resonance*. Wiley, 2008.

[48] P. Mansfield. Multi-planar image-formation using nmr spin echoes. *Journal of Physics C-Solid State Physics*, 10(3):L55–L58, 1977.

[49] Jennifer A. McNab, Brian L. Edlow, Thomas Witzel, Susie Y. Huang, Himanshu Bhat, Keith Heberlein, Thorsten Feiweier, Kecheng Liu, Boris Keil, Julien Cohen-Adad, M. Dylan Tisdall, Rebecca D. Folkerth, Hannah C. Kinney, and Lawrence L. Wald. The human connectome project and beyond: Initial applications of 300 mt/m gradients. *Neuroimage*, 80(0):234–245, 2013.

[50] Jennifer A. McNab, Saâd Jbabdi, Sean C. L. Deoni, Gwenaëlle Douaud, Timothy E. J. Behrens, and Karla L. Miller. High resolution diffusion-weighted imaging in fixed human brain using diffusion-weighted steady state free precession. *Neuroimage*, 46(3):775–785, 2009.

[51] Daniel R. Messroghli, Kevin Walters, Sven Plein, Patrick Sparrow, Matthias G. Friedrich, John P. Ridgway, and Mohan U. Sivananthan. Myocardial t1 mapping: Application to patients with acute and chronic myocardial infarction. *Magnetic Resonance in Medicine*, 58(1):34–40, 2007.

[52] R. Mills. Self-diffusion in normal and heavy water in the range 1-45.deg. *The Journal of Physical Chemistry*, 77(5):685–688, 1973.

[53] M. J. Nuevo, J. J. Morales, and D. M. Heyes. Mass dependence of isotope self-diffusion by molecular dynamics. *Physical Review E*, 51(3):2026–2032, 1995.

[54] S. L. F. Owen, J. Heath, M. L. Kringelbach, J. F. Stein, and T. Z. Aziz. Preoperative dti and probabilistic tractography in an amputee with deep brain stimulation for lower limb stump pain. *British Journal of Neurosurgery*, 21(5):485–490, 2007.

[55] J. Perrin. *Les Atomes*, volume 1. Librairie Félix Alcan, Paris, 1913.

[56] C. Pierpaoli and P. J. Basser. Toward a quantitative assessment of diffusion anisotropy. *Magnetic Resonance in Medicine*, 36(6):893–906, 1996.

[57] K. P. Pruessmann, M. Weiger, M. B. Scheidegger, and P. Boesiger. Sense: Sensitivity encoding for fast mri. *Magnetic Resonance in Medicine*, 42(5):952–962, 1999.

[58] R. Schmidt, D. Graafen, S. Weber, and L. M. Schreiber. Computational fluid dynamics simulations of contrast agent bolus dispersion in a coronary bifurcation: impact on mri-based quantification of myocardial perfusion. *Computational and mathematical methods in medicine*, 2013:513187, 2013.

[59] Stefan O. Schoenberg, Olaf Dietrich, and Maximilian F. Reiser. *Parallel imaging in clinical MR applications*. Springer, 2007.

[60] K. Setsompop, R. Kimmlingen, E. Eberlein, T. Witzel, J. Cohen-Adad, J. A. McNab, B. Keil, M. D. Tisdall, P. Hoecht, P. Dietz, S. F. Cauley, V. Tountcheva, V. Matschl, V. H. Lenz, K. Heberlein, A. Potthast, H. Thein, J. Van Horn, A. Toga, F. Schmitt, D. Lehne, B. R. Rosen, V. Wedeen, and L. L. Wald. Pushing the limits of in vivo diffusion mri for the human connectome project. *Neuroimage*, 80:220–233, 2013.

[61] R. D. Shannon. Revised effective ionic-radii and systematic studies of interatomic distances in halides and chalcogenides. *Acta Crystallographica Section A*, 32(SEP1):751–767, 1976.

[62] K. Sommer, R. Schmidt, D. Graafen, H.-C. Breit, and L. M. Schreiber. Contrast agent bolus dispersion in a realistic coronary artery geometry: Influence of outlet boundary conditions. *Annals of Biomedical Engineering*, 42(4):787–796, 2013.

[63] A. W. Song, E. C. Wong, and J. S. Hyde. Echo-volume imaging. *Magnetic Resonance in Medicine*, 32(5):668–671, 1994.

[64] Ting Song, Wen-Jun Chen, Bo Yang, Hong-Pu Zhao, Jian-Wei Huang, Ming-Jin Cai, Tian-Fa Dong, and Tang-Sheng Li. Diffusion tensor imaging in the cervical spinal cord. *European Spine Journal*, 20(3):422–428, 2011.

[65] D. Sosnovik, R. Wang, G. Dai, T. Reese, and V. Wedeen. Diffusion mr tractography of the heart. *Journal of Cardiovascular Magnetic Resonance*, 11(1):47, 2009.

[66] D. E. Sosnovik, R. P. Wang, G. P. Dai, T. Wang, E. Aikawa, M. Novikov, A. Rosenzweig, R. J. Gilbert, and V. J. Wedeen. Diffusion spectrum mri tractography reveals the presence of a complex network of residual myofibers in infarcted myocardium. *Circulation-Cardiovascular Imaging*, 2(3):206–212, 2009.

[67] E. O. Stejskal and J. E. Tanner. spin diffusion measurements: spin echoes in the presence of a time-dependent field gradient. *Journal of Chemical Physics*, 42(1):288–299, 1965.

[68] S. W. Sun, J. J. Neil, and S. K. Song. Relative indices of water diffusion anisotropy are equivalent in live and formalin-fixed mouse brains. *Magnetic Resonance in Medicine*, 50(4):743–748, 2003.

[69] Koichi Tanaka, Hiroaki Waki, Yutaka Ido, Satoshi Akita, Yoshikazu Yoshida, Tamio Yoshida, and T. Matsuo. Protein and polymer analyses up to m/z 100 000 by laser ionization time-of-flight mass spectrometry. *Rapid Communications in Mass Spectrometry*, 2(8):151–153, 1988.

[70] Arthur W. Toga, Kristi A. Clark, Paul M. Thompson, David W. Shattuck, and John Darrell Van Horn. Mapping the human connectome. *Neurosurgery*, 71(1):1–5, 2012.

[71] Fernanda Tovar-Moll, Jorge Moll, Ricardo de Oliveira-Souza, Ivanei Bramati, Pedro A. Andreiuolo, and Roberto Lent. Neuroplasticity in human callosal dysgenesis: A diffusion tensor imaging study. *Cerebral Cortex*, 17(3):531–541, 2007.

[72] M. Tovi and A. Ericsson. Measurements of t1 and t2 over time in formalin-fixed human whole-brain specimens. *Acta Radiologica*, 33(5):400–404, 1992.

[73] D. S. Tuch. Q-ball imaging. *Magnetic Resonance in Medicine*, 52(6):1358–1372, 2004.

[74] N. A. Viola, R. S. Rarig, W. Ouellette, and R. P. Doyle. Synthesis, structure and thermal analysis of the gallium complex of 1,4,7,10-tetraazacyclo-dodecane-n,n ′,n ″,n ″′-tetraacetic acid (dota). *Polyhedron*, 25(18):3457–3462, 2006.

[75] T. J. Wadas, E. H. Wong, G. R. Weisman, and C. J. Anderson. Coordinating radiometals of copper, gallium, indium, yttrium, and zirconium for pet and spect imaging of disease. *Chemical Reviews*, 110(5):2858–2902, 2010.

[76] J. P. Wansapura, S. K. Holland, R. S. Dunn, and W. S. Ball. Nmr relaxation times in the human brain at 3.0 tesla. *Jmri-Journal of Magnetic Resonance Imaging*, 9(4):531–538, 1999.

[77] R.C. Weast. *CRC Handbook of Chemistry and Physics*. Chemical Rubber Publishing Company, Boca Raton, 1990.

[78] T. White. Diffusion tensor imaging in psychiatric disorders. *TMRI*, 19(2):97–109, 2008.

[79] C. Wieseotte. *Bestimmung des Diffusionskoeffizienten von Gd-DOTA mittels Magnetresonanzspektroskopie und ultraschnelle 13C-MR-Bildgebung*. Diploma Thesis. Johannes Gutenberg University, Mainz, 2012.

[80] F.-C. Yeh, T. D. Verstynen, Y. Wang, J. C. Fernández-Miranda, and W.-Y. I. Tseng. Deterministic diffusion fiber tracking improved by quantitative anisotropy. *PLoS ONE*, 8(11):e80713, 2013.

[81] F. C. Yeh, V. J. Wedeen, and W. Y. I. Tseng. Generalized q-sampling imaging. *Ieee Transactions on Medical Imaging*, 29(9):1626–1635, 2010.

DECLARATION

I hereby declare that I wrote the dissertation submitted without any unauthorized external assistance and used only sources acknowledged in the work. All textual passages which are appropriated verbatim or paraphrased from published and unpublished texts as well as all information obtained from oral sources are duly indicated and listed in accordance with bibliographical rules. In carrying out this research, I complied with the rules of standard scientific practice as formulated in the statutes of Johannes Gutenberg-University Mainz to ensure standard scientific practice.

Mainz, 28. September 2015

Christian Wieseotte